NORTHWESTERN UNIVERSITY

Initial Growth of Ultrathin Metal Films on Semiconductors

A DISSERTATION

SUBMITTED TO THE GRADUATE SCHOOL

IN PARTIAL FULFILLEMENT OF THE REQUIREMENTS

for the degree

DOCTOR OF PHILOSOPHY

Field of Materials Science and Engineering

By

Daniel Grozea

EVANSTON, ILLINOIS

June 2000

ABSTRACT

Initial Growth of Ultrathin Metal Films on Semiconductors

Daniel Grozea

The importance of surface and thin-film science has been steadily increasing and now constitutes one of the most significant aspects of the semiconductor industry. In many cases atoms from the surface layers of a crystal do not occupy the positions that would be expected from a simple continuation of the bulk structure, leading to the formation of a reconstructed surface. Moreover, the presence of adsorbate atoms on the surface induces many different surface reconstructions that can be considered as the early stages of nucleation and thin film growth on that particular substrate.

The combination of structural information from high-resolution transmission electron microscopy and surface chemical analysis allows for a full characterization of the room temperature deposition of Au on the Si(001)-(2x1) reconstruction. In addition, the effects of electron beam heating during the preparation of clean Si surfaces suitable for epitaxial studies in UHV conditions is investigated.

A new Direct Methods approach involving a Minimum Relative Entropy method is successfully applied to both transmission electron and X-ray diffraction data to solve

unknown surface structures. The atomic structures of the Si(111)-(6x6)Au and Si(111)-(3x1)Ag phases are determined using this technique on surface X-ray diffraction data and transmission electron diffraction data, respectively.

During the investigation of the Ag submonolayer on the Ge(111) system, a new stable reconstruction Ge(111)-(3x1)Ag is obtained over large areas, although previous studies have reported its existence only as small insets. The TED data are analyzed using Direct Methods and heavy-atom holography, with the result of an atomic model of the structure similar to that of the Si(111)-(3x1)Ag reconstruction.

Finally, surface phase diagrams are proposed for the submonolayer region of the Ag/Ge(111) system and for the supermonolayer region of the Au/Si(111) system, based on the atomic arrangements of all the phases and the interphase relationships and on a survey of all relevant experimental reports.

Approved by

Professor Laurence D. Marks (Thesis advisor)

Department of Materials Science and Engineering

Robert R. McCormick School of Engineering and Applied Science

Northwestern University, Evanston, IL 60208

ACKNOWLEDGEMENTS

Somebody mentioned the 'Three musketeers', in fact there were four of them. And we should not forget the king, who was definitely not Louis XIII, but more like the big one, Louis XIV. As much king as you can get, with his great moments or mistakes.

Without my friends', Chris Collazo-Davila, Erman Bengu, and Eric Landree, support and encouragement during these long graduate years, I am not certain about getting to ever write this dissertation. I do not have enough words to describe how much I owe them.

I would like to acknowledge my thesis advisor, Prof. L. D. Marks, for teaching and introducing me to 'Big Science'.

I also appreciate the contribution of various members of our group to my achievements. We shared knowledge, company, and assisted each other in many and different ways. Thanks to the girls, especially Monica Salud and Natasha Erdman, for changing things around the lab.

TABLE OF CONTENTS

Abstract ii

Acknowledgements iv

Table of contents v

List of Tables viii

List of Figures ix

Chapter 1: Introduction 1

1.1 Surface structures 2

1.2 Surface sensitive techniques 6

1.3 SPEAR 10

1.4 Sample preparation 21

Chapter 2: Determination of the atomic geometry of surface structures 27

2.1 Initial model 27

2.1.1. Genetic Algorithm 31

2.2 Structure completion 32

2.3 Refinement 39

2.4 Discussion 40

Chapter 3: Effect of small particles on the Au/Si(001) interface formation at room-temperature 43

3.1 Surface roughening by electron beam heating 44

3.1.1 Experimental 46

3.1.2 Results 46

3.2 Role of small particles in the Au/Si interface formation 53

3.2.1 Experimental 55

3.2.2 Results 57

3.2.3 Discussion of Results 64

Chapter 4: Structure determination of Si(111)-(6x6)Au surface 67

4.1 Background 68

4.2 Experimental 71

4.3 Initial Model 72

4.4 Structure Refinement 73

4.5 Discussion of Results 79

Chapter 5: Structural investigation of the 3x1 reconstruction 91

5.1 Background 91

5.2 Si(111)-(3x1)Ag 96

5.2.1 Experimental 96

5.2.2 Initial model 98

5.2.3 Structure Refinement 100

5.2.4 Discussion of Results 103

5.3 Theoretical confirmation of the model 103

5.4 Ge(111)-(3x1)Ag 105

5.4.1 Experimental 106

5.4.2 Initial model 107

5.4.3 Structure Refinement 111

5.4.4 Discussion of Results 112

Chapter 6: Surface phase diagrams 116

6.1 Background 117

6.2 The Ag/Ge(111) system 122

6.3 The Au/Si(111) system 131

Chapter 7: Future work 137

References 140

Appendix A: The Spear Dance 156

TABLES

4.1 Refined atomic positions for the Si(111)-(6x6)Au structure 80

4.2 Comparison of the stronger experimental and calculated reflections from the Si(111)-(6x6)Au surface 82

5.1 Refined atomic positions for the Si(111)-(3x1)Ag structure 101

FIGURES

1.1. Photograph of the SPEAR system and the attached Hitachi UHV H-9000 microscope 11

1.2 a) SEM image of an area from a Si sample, and b) TEM bright field image of the same area 15

1.3. SEM image of ZrO_2 + 7 wt% Cu powder on an Au grid 16

1.4. XPS spectra from ZrO_2 + 7 wt% Cu powder dispersed on a Au grid using Al Kα radiation 17

1.5. Ion-induced secondary electron images while O ion milling of a Si sample 19

1.6. Ion-induced secondary electron images while sputtering an area within the oxidized region with Ar ions 20

1.7. Schematic diagram of the Mo ring used as a sample holder in SPEAR 23

1.8. XPS spectra from a Si sample. a) As-etched surface, and b) Clean surface after cycles of ion milling and thermal annealing 24

1.9. XPS spectra from a Ge sample. a) As-etched surface, and b) Clean surface after cycles of ion milling and thermal annealing 25

1.10. Diffraction pattern corresponding to the Si(111)-(7x7) surface reconstruction 26

2.1. Contour map of the scattering potential generated using phases estimated through Direct Methods for the Si(111)-($\sqrt{3}$x$\sqrt{3}$)R30°Ag structure 34

2.2. Contour map of the scattering potential found for Si(111)-(3x1)Ag 35

2.3. Contour map of the charge density map generated by Direct Methods, showing the best solution for Ge(111)-(4x4)Ag 35

2.4. Contour map of the charge density calculated by Direct Methods, showing an initial fragment of the Si(111)-(6x6)Au structure 36

2.5. Flow chart of the iteration process of atomic position refinement/heavy-atom

holography 37

3.1. Dark field image of the Si(001) surface using the Si(220) reflection: a)Showing well-ordered steps prior to ion beam disordering of surface B, and b)After ion beam roughening, when the surface steps are no longer present 48

3.2. Diagram of the sample's beam exposure: a) Direction of electron beam, and Direction of Ar ion beam for b) Side B, and c) Side A 49

3.3. Dark field image of the Si(001) surface showing the presence of well-ordered steps: a)Prior to, and b)After the ion beam disordering of the sample surface A 51

3.4. Schematic of the Si(001)-(2x1) surface during heating with a direct current showing the motion of monoatomic steps 52

3.5. Off-zone HREM image of Si(001)-(2x1) surface taken at 200 kV 56

3.6. Shifts in the Si 2p and Au $4f_{7/2}$ peaks as a function of Au coverage 58

3.7. Line shape of the Si LVV and Au NVV Auger transitions as a function of Au coverage 60

3.8. HREM image of the Si(001) surface following 13 Å of Au deposition 61

3.9. TED pattern of the Si(001) surface following 13 Å of Au deposition 63

4.1. a) Charge density map of the initial fragment used for the Si(111)-(6x6)Au structure, b), c) Intermediate steps in constructing the model; d) Final model with 42 gold atoms 74

4.2. a)-d) Corresponding diffraction patterns for Figure 4.1a-d 76

4.3. New possible atom sites generated by heavy-atom holography after processing the partial model from Figure 4.1c 77

4.4. Diagram of the Si(111)-(6x6)Au structure 83

4.5. Triangular domain walls of Si(111)-(6x6)Au 86

4.6. Experimental diffraction pattern of the ($\sqrt{3}$x$\sqrt{3}$) + ring-like structure 87

4.7. a) Glass-like tiling using A and B gold units and, b) Corresponding diffraction pattern 88

5.1. Models proposed for the (3x1) reconstruction: (a) Seiwatz chain, and (b) Extended Pandey chain 95

5.2. Experimental diffraction pattern showing the presence of a) Both (3x1) and ($\sqrt{3}$x$\sqrt{3}$) phases, and b) Only the (3x1) phase 97

5.3. Contour maps of the calculated surface scattering potential using phases estimated through Direct Methods for Si(111)-(3x1)Ag 99

5.4. Model proposed for the (3x1) reconstruction 102

5.5. Honeycomb chain-channel model with the Si double bond 104

5.6. (a) Dark field image of the (4x4) triangular domains with narrow strips of (3x1) structure visible on the edge as one or two linear features, and (b) Corresponding (4x4) diffraction pattern 108

5.7. (a) Dark field image showing linear features due to one domain of the (3x1) structure, and (b) Corresponding diffraction pattern displaying both (3x1) and ($\sqrt{3}$x$\sqrt{3}$) phases 109

5.8. Contour map of the calculated surface scattering potential using phases estimated through Direct Methods for Ge(111)-(3x1)Ag 110

5.9. Domain boundary model for the boundary between (4x4) and (3x1) structures 113

6.1. Surface phase diagram for the Au/Si(111) system proposed by Plass (1996) (Region 1 – submonolayer coverage) with in situ experimental results. Region 2 (1 ML – 2 ML coverage) displays experimental data points 118

6.2. T-T-T curve: effects of cooling rate and temperature on the transformation rate 121

6.3. Schematic phase diagram of the Ag/Ge(111) system proposed by Le Lay 122

6.4. TED patterns taken close to a Ge(111) zone-axis. a) From a region covered by the (4x4) structure, and b) From a region with both (4x4) and ($\sqrt{3}$x$\sqrt{3}$) domains 125

6.5. a) Proposed surface phase diagram for the Ag/Ge(111) system in the submonolayer regime, and b) The phase diagram with experimental data points 127

6.6 Proposed T-T-T curve representation of the transformation from a (4x4) disordered structure to the (4x4) ordered phase 130

6.7 a) Proposed phase diagram extension to the supermonolayer regime for the Au/Si(111) system, and b) The phase diagram with experimental data points, limited from 0.5 to 1.5 ML, from Figure 6.1 134

6.8 Proposed T-T-T curve representation of the transformation from $\beta(\sqrt{3}x\sqrt{3})$ phase to the (6x6) phase 136

CHAPTER 1:

INTRODUCTION

The importance of surface and thin-film science has been steadily increasing and now constitutes one of the most significant aspects of the semiconductor industry. Despite this practical importance, fundamental understanding of surface and interface phenomena has been difficult to attain due to their complexity. More often than not, uncontrolled impurities at surfaces as well as interdiffusion or reactions determine the macroscopic scale properties of semiconductor devices.

Critical questions, such as whether Moore's law will hold forever, or can the semiconductor industry keep on accelerating, have continuously been asked. They hinge upon how much the scaling-down of the electronic devices can go on. Gordon Moore observed that the number of transistors on a chip quadruples every three years, resulting in a new chip generation with a feature size that is 30% smaller than that of the previous generation. This trend has held true for the last 30 years despite potential technology barriers.

An important role is played by Semiconductor Industry Association (SIA), with

its unique charter of coordinating academic research to meet industry's needs. The SIA publishes a biannual Roadmap which gives projections of device technology. The 1997 National Technology Roadmap for Semiconductors estimates a formidable barrier to be reached in the year 2006 due to the physical limits of optical lithography currently used in chip production. The forecast requires 'a vigorous creative research activity' to surmount that barrier (Hu 1999).

Therefore, the industry needs to move from sub-micron technology to nanotechnology. In making further miniaturized structures which approach the atomic scale, the atomic geometry of these structures and atomic manipulation and control techniques become important. On the other hand, instead of developing nanosize devices by pursuing the miniaturization limit of the dominant chip technology (the metal-oxide semiconductor), another direction would be to explore breakthrough devices that utilize quantum effects such as single-electron devices (Sone et al. 1999).

1.1 Surface structures

Developments in surface-sensitive techniques, film deposition technology, and ab initio theoretical methods have enabled the investigation of the atomic geometry and electronic properties of semiconductor surfaces with more accuracy and reliability.

In many cases, atoms from the surface layer of a crystal do not occupy the positions that would be expected from a simple continuation of the bulk structure. The bonding configuration of the surface atoms being different from that of the bulk atoms, small shifts in atom positions either normal to or parallel to the crystal surface can lead to

a substantial increase in bonding energy and a lowering of the total energy of the system. This new atomic configuration, called a reconstruction, can extend several atomic layers into the bulk.

In addition to native reconstructions, the presence of adsorbate atoms on the surface, usually less than one monolayer, induces many different surface reconstructions. These can be considered as the early stages of nucleation and thin film growth on that particular substrate. Classic epitaxial theories (Frankl and Venables 1970, Zinsmeister 1971), which assume that bulk terminated structures for the substrate surface serve as simple bonding sites for the adsorbates, should be reconsidered as processes become observable at the atomic level under ultrahigh vacuum (UHV) conditions. In fact, it is the tendency for most adsorbate-semiconductor surfaces to be reconstructed.

A standard notation for reconstructions is M(hkl)-(nxm)RΦ-C where M(hkl) is the bulk material and its crystallographic orientation (Wood 1964). Considering that **a** and **b** are the two-dimensional surface unit vectors describing the original surface periodicity, (nxm) indicates the new surface structure with a periodicity n times along the original **a** unit cell direction and m times along the **b** direction. If the reconstruction lattice is rotated with respect to the original surface unit cell, an RΦ notation is used to define the rotation angle Φ. Finally, an adsorbate induced reconstruction is indicated by its chemical symbol -C.

Despite the development of numerous experimental techniques and advances in theoretical calculations, in most cases the atomic surface structure is not yet unambiguously known. Nevertheless, basic concepts such as the reduction of the number

of surface dangling bonds and the relief of surface stress, both consistent with the minimization of the surface free energy, are recognized as the driving forces for surface rearrangement processes.

More than once, a structure has been believed to be solved and is then reconsidered in later studies (see, for example, the case of the Si(111)-(3x1)Ag surface, Weitering et al. 1994; Erwin 1995; Collazo-Davila, Grozea, and Marks 1998). At the moment, there are no techniques which can straightforwardly image the atomic arrangement at the surface. Scanning tunneling microscopy (STM) images show the density of surface states, not atom locations (e.g. Binning and Rohrer 1987). A protruding atom or a high density of states have the same effect, leading to an intricate interpretation of results. Moreover, STM is sensitive to only the outermost layer of atoms and ignores subsurface relaxation. This limitation does not apply to transmission electron microscopy and x-ray diffraction. High resolution transmission electron microscopy (HREM) can provide detailed atomic-scale information about surface structures by direct imaging. This approach has been successful in resolving not only heavy atoms such as Ir on Ir(100)-(5x1) (Marks, Xu, and Dunn 1993) and Au atoms on Si(111)-(5x2) (Marks and Plass 1995), but also lighter atoms as such as all the Si atoms from the Si(111)-(7x7) structure (Bengu et al. 1996). However, HREM information is tedious to acquire and the signal-to-noise ratio is extremely low.

On the other hand, the use of diffraction techniques, electron and x-ray alike, to investigate the surface atomic arrangement necessitates a starting model which is close to the correct structure. This approach has the advantage of easy and accurate refinement.

Patterson maps generated from surface diffraction data constitute a technique to solve the surface atomic geometry (for instance, Woolfson and Fan 1995). These maps show positive peaks corresponding to interatomic vectors. Therefore, the map analysis could lead to information on only some part of the structure due to the difficulty of picking out many individual vectors and the presence of artifacts, as well as false peaks induced by special relationships between interatomic vectors.

More powerful than the Patterson approach, Direct Methods have become a routine analysis technique for solving bulk crystal structure from x-ray (for example, Giacovazzo 1980; Woolfson 1987; Woolfson and Fan 1995) and from electron diffraction data (not so routine, Dorset 1995). Direct Methods have recently been applied to surface diffraction data by our group to determine the initial structure estimate. This approach has worked for electron as well as x-ray surface diffraction data, since kinematical diffraction, a necessary condition, is an adequate approximation in both cases (Tanishiro and Takayanagi, 1989). The application of Direct Methods to known reconstructions successfully found the "correct" solution in each case: Si(111)-(7x7) (Gilmore et al. 1997), Si(111)-($\sqrt{3}$x$\sqrt{3}$)R30°Au, and Si(111)-(5x2)Au (Marks, Plass, and Dorset 1997) (using electron data in every case). Subsequently, a large array of unknown structures were tackled for either electron or x-ray data on semiconductor surfaces: Si(111)-(4x1)In (Collazo-Davila, Marks et al. 1997), Si(111)-(6x6)Au (Marks, Grozea et al. 1998; Grozea et al. 1998), Si(111)-(3x1)Ag (Collazo-Davila, Grozea, and Marks 1998), Ge(111)-(4x4)Ag (Collazo-Davila et al. 1998), and metal oxides: TiO_{2-x}(100)-(1x3) (Landree et al. 1998), MgO(111)-(n$\sqrt{3}$) (Plass et al. 1998).

1.2 Surface sensitive techniques

Over the last several decades, many different methods have been developed for probing the structural, chemical, or electronic properties of surface structures. In this section, only the techniques essential to and broadly employed in the investigations described in the following chapters will be briefly overviewed.

While STM, atomic force microscopy (AFM), and low-energy electron diffraction (LEED), techniques traditionally associated with surface studies, have provided a wealth of knowledge about surfaces at the atomic level, they suffer from an important limitation. These techniques are sensitive to only the outermost layer of atoms, and it has been suggested that surface reconstructions can involve relaxations of the top several layers of atoms near the surface extending into the bulk (LaFemina 1992).

A strong point of the HREM technique is its ability to look at both the surface and the bulk at the same time. However, the atomic or almost-atomic resolution may be limited in practice because the surface-specific information appears as a weak signal either buried in noise or on top of a large background.

Considering the orientation of the specimen surface with respect to the incident electron beam, two HREM imaging modes of surfaces can be discussed: profile view (Marks and Smith 1983) or plan view imaging. In the case of the profile imaging mode, the electron beam is parallel to the surface. Although applied with success in several cases, e.g. the study of the Au(110)-(2x1) reconstruction (Marks 1983) or CdTe(001)-(2x1) and (3x1) surfaces (Lu and Smith 1991), this technique does not image individual

atoms but only arrangements of the atomic rows parallel to the beam. Other limitations arise due to the very thin edge involved. This mode's application to large surface structures is therefore restricted. Another limitation is related to obtaining an equilibrium surface configuration given the intrinsic thermodynamical instability of a thin profile edge.

In the other mode, plan view imaging, the incident beam is perpendicular to the surface of interest. Thermodynamical instability is no longer a problem in this case. Information from both surfaces, top and bottom, and the bulk material in between is present in images. Plan view imaging can be performed in either on-zone axis mode (Krakow 1982; Nihoul, Abdelmoula, and Métois 1984; Xu et al. 1993), where the electron beam is parallel to a major zone axis of the material, or off-zone axis mode (Marks, Xu, and Dunn 1993; Marks and Plass 1995) by tilting the crystal away from the principal axial orientation. The surface structure can be approximated as almost two-dimensional and it therefore gives rise to a set of continuous lines in reciprocal space (rel rods) in contrast to the sets of sharp maxima at the reciprocal lattice points due to the bulk. The latter are only slightly elongated in the direction parallel to the incident beam. Thus, with tilting off the zone axis, the amplitudes of the reflections from the bulk lattice may be significantly reduced relative to the reflections from the surface layers (Xu and Marks 1992). A higher surface sensitivity may be achieved by this modification of the imaging conditions, reducing the bulk signal and leading to better HREM images.

The application of the off-zone imaging mode has been successful in identifying heavy atom positions, e.g. the case of Au sites in the Si(111)-(5x2)Au reconstruction

(Marks and Plass 1995). The images provided the starting elements necessary to solve the atomic arrangement of this surface. In fact, a combination of diffraction and imaging techniques is typically necessary to fully characterize a surface structure by transmission electron microscopy (TEM).

The major difficulty in solving unknown surface structures based only on diffraction data is the lack of a starting point from which to refine atomic positions. However, if an initial model is known, information about the atomic structure of a reconstruction can be obtained from quantitative analysis of beam intensities in transmission electron diffraction (TED) patterns. Electron diffraction patterns are recorded mostly in the off-zone axis mode since it yields better surface data as has already been discussed. Typically, a series of diffraction patterns are recorded at different exposure times to cover the large dynamic variation of surface and bulk beams. The experimental data sets are reduced through a cross-correlation technique developed by our group (Xu, Jayaram, and Marks 1994). To obtain the final atomic arrangement, either a kinematical or a dynamical approach including the effects of crystal thickness and tilt is used to numerically calculate the beam intensity generated from an initial structure model. The absolute intensities of the surface diffraction spots are calculated and then compared against the experimentally measured ones, and the difference is minimized in an iterative process to yield the final model.

As an example, for the native Ge surface reconstruction, Ge(001)-(2x1), the lateral atomic displacements for the first top six layers extending into the bulk have been determined (Collazo-Davila, Grozea et al. 1997). The simulations included dynamical

refinements taking into account crystal thickness and tilt. The atomic positions coincide with the results from x-ray studies to within a few hundredths of an Angstrom. Such a precise experimental agreement suggests the use of the Ge(001)-(2x1) surface as a valuable model system for theoretical studies of native surface reconstructions.

Other important features of the surfaces, the electronic structure and the chemical state, are probed by XPS and AES techniques (for example Crescenzi and Piancastelli 1996). The surface sensitivity and quantitative chemical analysis capabilities of XPS have made it one of today's most broadly used surface analysis techniques. Its objective is the detection and energy analysis of photoelectrons whose energy exceeds their binding energy and are emitted following the exposure to x-ray beams. With an ability to nondestructively detect all elements except for H and He at levels down to about 0.05 at%, it is used extensively to examine the composition of the surface layers of solid materials down to a depth of about 5 nm. XPS can not only identify the presence of an element but it can also distinguish different chemical states of a particular element in different environments by measuring the chemical shift of the core lines.

For Auger spectroscopy, either x-rays or electrons are used to generate Auger electrons. Thus, while using XPS, additional information is collected in the form of Auger lines and which be employed to calculate the so-called Auger Parameter. This parameter is a way to highlight the chemical shifts. On the other hand, the use of electron stimulation has several advantages, such as probing only the very top sample layers, due to the electrons' short mean free path of a few Angstroms. Furthermore, an electron source is easy to focus into narrow beams and it needs less sophisticated, and hence

cheaper, detection systems than XPS. An Auger electron can be produced when a core electron is removed either by an incident photon or electron. The resulting metastable hole can be filled with an electron from a higher atomic level, with the outcome of an electron being ejected (the Auger electron), or of an x-ray photon being emitted. These are two competing processes. The AES can detect down to 10^{-3} of a monolayer with a spatial resolution of 20 nm.

1.3 SPEAR

Further progress in surface science is intimately correlated with the development of experimental tools and techniques that are suited for studies with clean and intentionally modified surfaces. First of all, UHV conditions are needed for such investigations to keep the specimen surface fairly clean over a reasonable period of time.

For the experiments performed for this study, I was fortunate to have access to an integrated surface science system, the SPEAR system (Sample Preparation, Evaluation, Analysis, and Reaction) (Collazo-Davila et al. 1995), attached to a UHV high resolution transmission electron microscope, Figure 1.1. The whole system combines the ability to prepare clean surfaces with surface analytical tools such as x-ray photoelectron spectroscopy (XPS) and Auger electron spectroscopy (AES), and atomic structure information available from the microscope. During operation, the entire system is capable of maintaining UHV conditions.

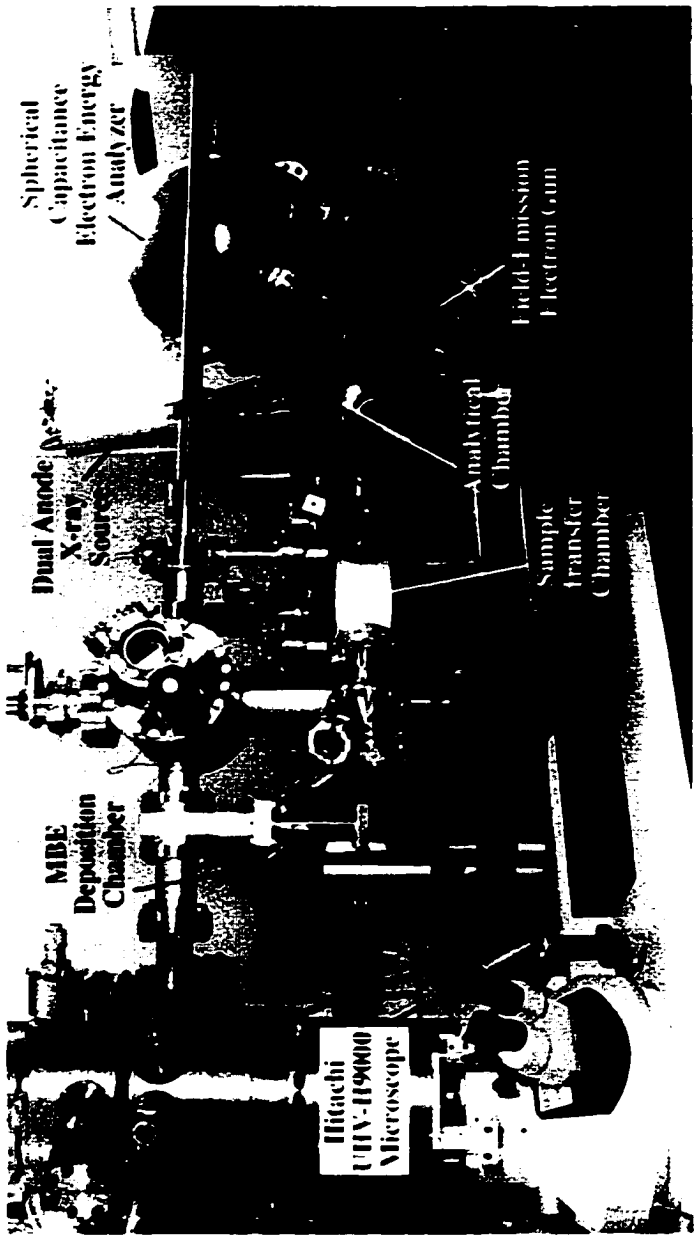

Figure 1.1. Photograph of the SPEAR (Sample Preparation, Evaluation, Analysis, and Reaction) system and the attached Hitachi UHV H-9000 microscope.

The microscope is a Hitachi UHV H-9000 TEM with its differentially pumping system modified to achieve operating pressures better than $1x10^{-10}$ Torr. It is equipped with a Parallel Electron Energy Loss Spectroscopy (PEELS) unit to enable bulk chemical analysis and estimation of the sample thickness, and a metal deposition stage for three different metals. At the same time, the presence of the PEELS unit has effectively precluded the replacement of the present TV-rate CCD camera with a slow-scan CCD camera.

The advantage of TEM over many other techniques lies in its ability to provide information about the crystal structure at the surface and extending into the bulk. However, it is limited by its lack of surface chemical information. One approach to overcoming this obstacle is to modify the electron optics region of the microscope or even to replace it with a fully equipped surface science chamber (Heinemann and Poppa 1986; Kondo et al. 1991; Twesten, Gibson, and Ross 1994). Unfortunately, more often than not, this leads to compromising the resolution capabilities of the TEM, in some cases from 0.21 nm to 2.5 nm (Twesten, Gibson, and Ross 1994).

As an alternative approach, several groups have left the electron optics untouched (Métois, Nitsche, and Heyraud 1989; McCartney and Smith 1991). Although this preserves the resolution capabilities of the TEM, typically less peripheral equipment can be incorporated. For our instrument at Northwestern University, Profs. L. D. Marks and P. C. Stair have left the TEM optics intact and placed all the surface science equipment in an adjoining chamber.

The SPEAR system represents a second-generation design for the side chamber approach, and it incorporates many improvements over the previous UHV surface science chamber (Bonevich and Marks 1992). It is a multichamber system and has several ports for further expansion. The four original chambers are separated by gate valves, allowing for their independent operation. Hence, they can be brought up to air and pumped back down individually.

The load-lock chamber constitutes a separate introduction chamber for the insertion and retrieval of up to five samples without breaking the UHV conditions for the whole system. Usually an overnight bake is used to bring the load-lock close to UHV, after which it can be opened for a quick exchange to the transfer chamber.

The transfer chamber has two levels. The upper module holds up to four microscope cartridges (one of them a heating stage), and is connected to the lower level via an elevator rod and to the microscope through a long transfer rod. The lower level has a storage module for up to eight samples and a metal deposition stage for five different metals. It connects all the chambers and is employed to transfer samples using a central linear-rotary transfer arm. The large number of samples that can be present inside the system allows for multiple experiments to be carried out simultaneously and greatly improves the efficiency of the microscope and the SPEAR system.

The analytical chamber was designed to perform both sample surface cleaning and chemical characterization. Samples can be cleaned through cycles of ion milling and thermal annealing. A differentially pumped Duoplasmatron Ion Gun, with a minimum probe size of 5 μm, is used for removal of surface contaminants with oxygen, argon, and

xenon (currently replaced with nitrogen) ion beams. The beam energy can be varied between 0.5 – 10 keV. Low-energy ions are used to avoid the generation of a high level of defects and high-energy ions for implantation studies. Sample heating can be induced resistively or via an electron gun capable of delivering 1 – 10 keV electrons. The sample temperature is monitored with an infrared pyrometer, assuring a good reproducibility of the annealing conditions.

XPS and AES techniques are available for chemical analysis utilizing a spherical capacitance electron energy analyzer with an analysis area from 10mm x 3mm to 70μm x 70μm, a dual-anode x-ray source capable of producing either Al Kα or Mg Kα x-rays, and an electron gun with a thermal field emitter and scanning ability. Scanning electron microscopy (SEM) images are acquired with the electron gun and a Channeltron secondary electron detector giving information about the sample topography.

To illustrate the capabilities of the SPEAR system, Figure 1.2 shows how the same area can be identified in the microscope and in the analytical chamber using SEM, leading to precise correlation between structural and chemical analysis. To roughly determine the detection limits of the XPS, a test sample was prepared by dusting zirconia powder containing 7 wt% Cu on a 1000-mesh Au grid. The approximate surface area coverage was estimated at between 10% and 15% using SEM, Figure 1.3. Figure 1.4a is the XPS spectrum of the sample, illustrating the various chemicals detected, and the stronger Cu peaks are highlighted in Figure 1.4b using detailed scanning.

An interesting idea was to use the Channeltron detector from the SEM and the video imaging system to capture the secondary electrons ejected from samples during ion

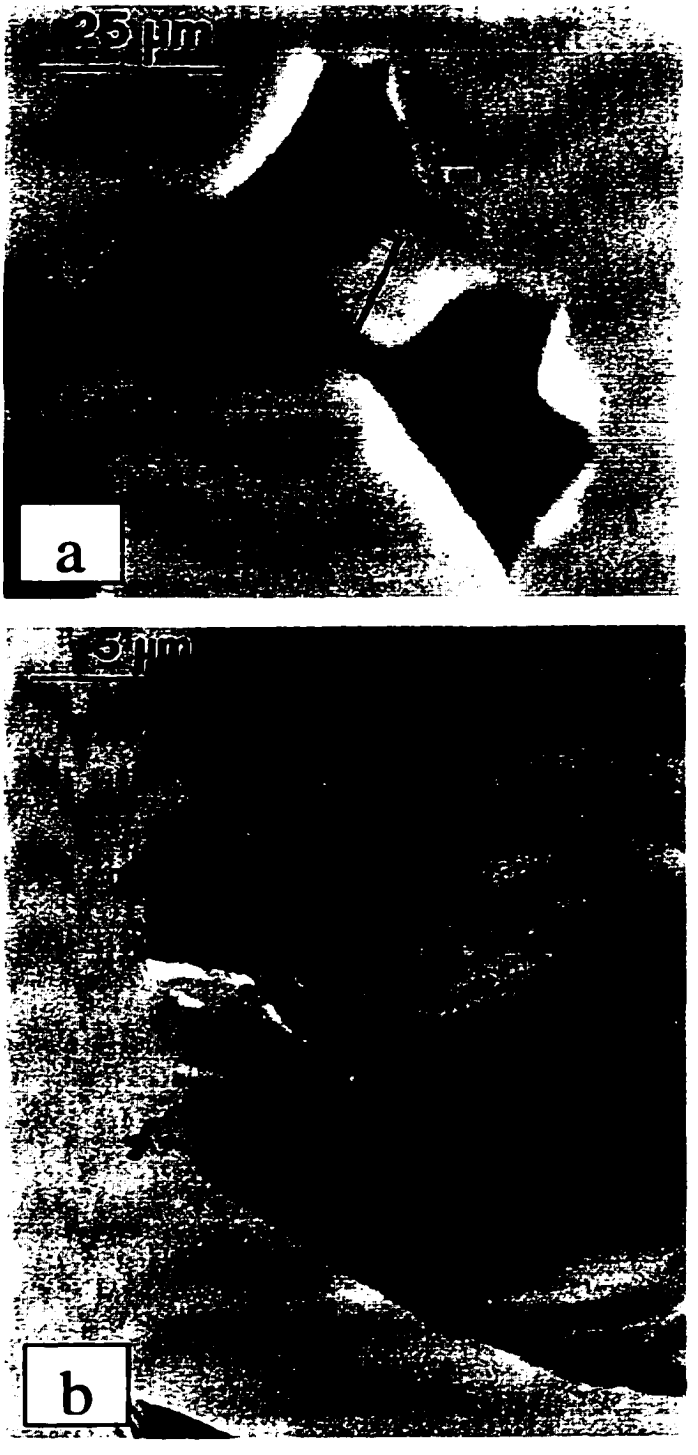

Figure 1.2. a) SEM image of an area from a Si sample, and b) TEM bright field image of the same area.

Figure 1.3. SEM image of ZrO_2 + 7 wt% Cu powder on an Au grid.

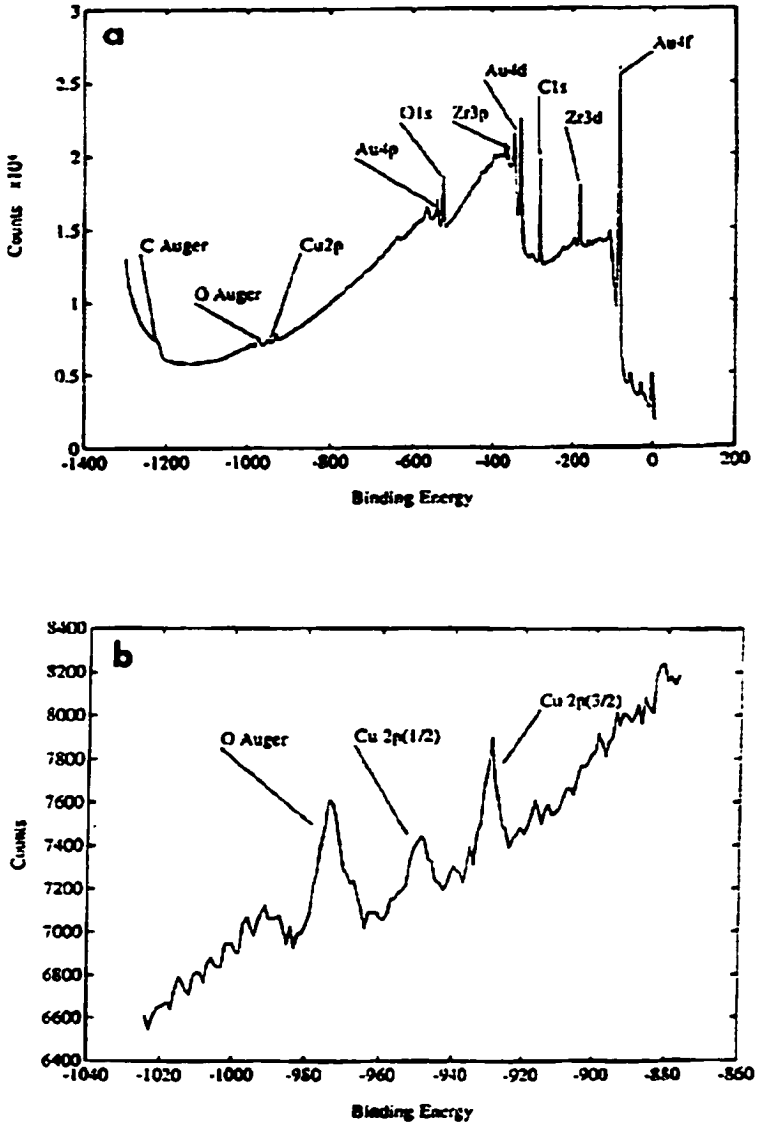

Figure 1.4. XPS spectra from ZrO_2 + 7 wt% Cu powder dispersed on a Au grid using Al Kα radiation. a) Scan over the full binding energy range, and b) Detailed scan of the Cu 2p region.

milling and therefore provide accurate imaging of the sputtered region. This leads to complete avoidance of unwanted contaminants, especially from the sample holder (Mo ring). Figure 1.5a is a display of an ion-induced secondary electron image while milling around the hole region of a Si sample with 1.5 keV oxygen ions normal to the surface. Figure 1.5b is a lower magnification image after the completion of the oxygen milling, with the white square corresponding to a SiO_2 layer formation. Figure 1.6a shows a precisely sputtered area within the oxidized square region, milled with 1.5 keV argon ions at 45° from the surface normal. Figure 1.6b is a lower magnification ion-induced image after the Ar milling was completed. The region is dark now and only Ar is left as a contaminant.

The SPEAR system originally had a Molecular Beam Epitaxy module as a fourth chamber, configured for thin film deposition of GaAs with Ga and As Knudsen cells. It was replaced afterwards with the SINBAD unit for ion-beam-assisted deposition of ultrahard thin films for nucleation and growth studies (Bengu et al. 1998). A new chamber, Molecular and Ion Beam Epitaxy (MIBE), has also been attached to SPEAR using one of the expansion slots. MIBE is dedicated for studies of coatings and multilayers grown by magnetron and ion-beam sources. In addition, a gas cell chamber is under construction and is meant for investigations of oxide surfaces at different pressures and under various atmospheres.

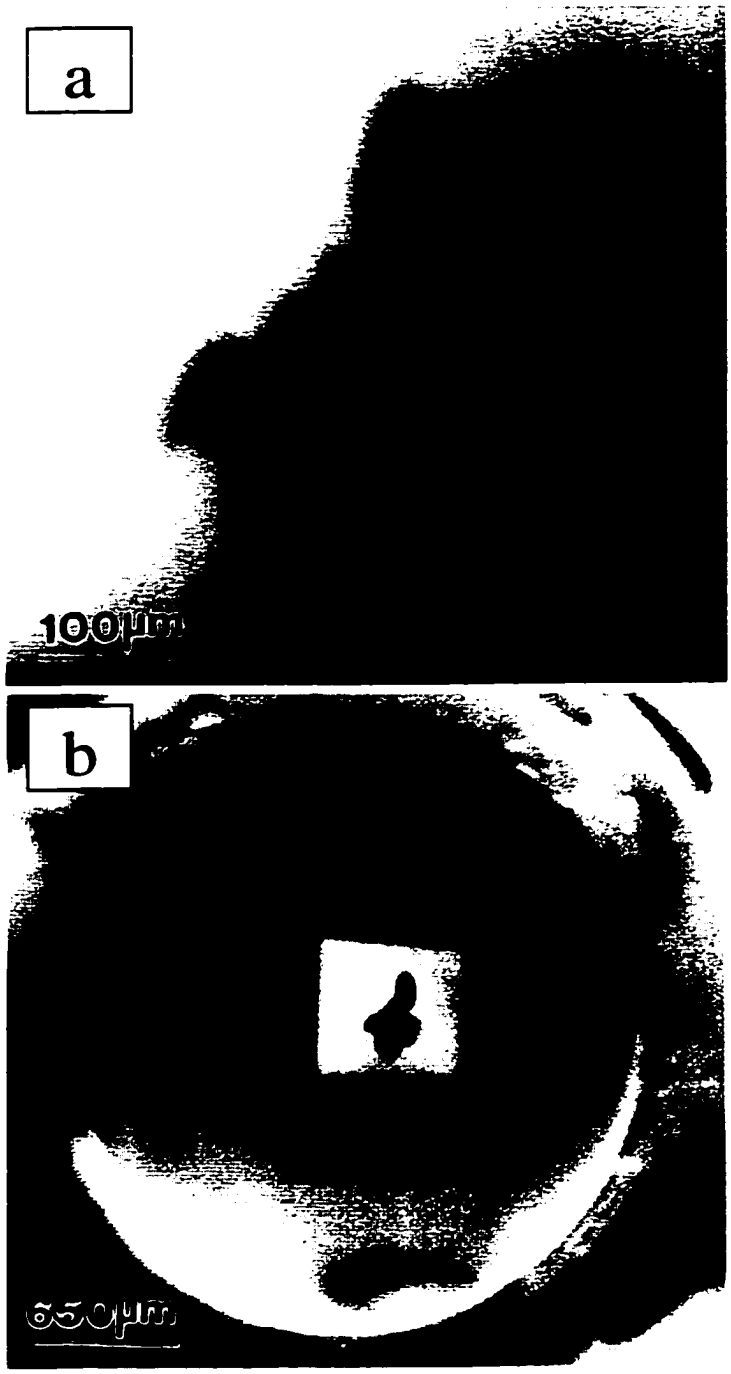

Figure 1.5. a) Ion-induced secondary electron image while O ion milling of a Si sample, and b) Lower magnification image after the completion of the ion milling.

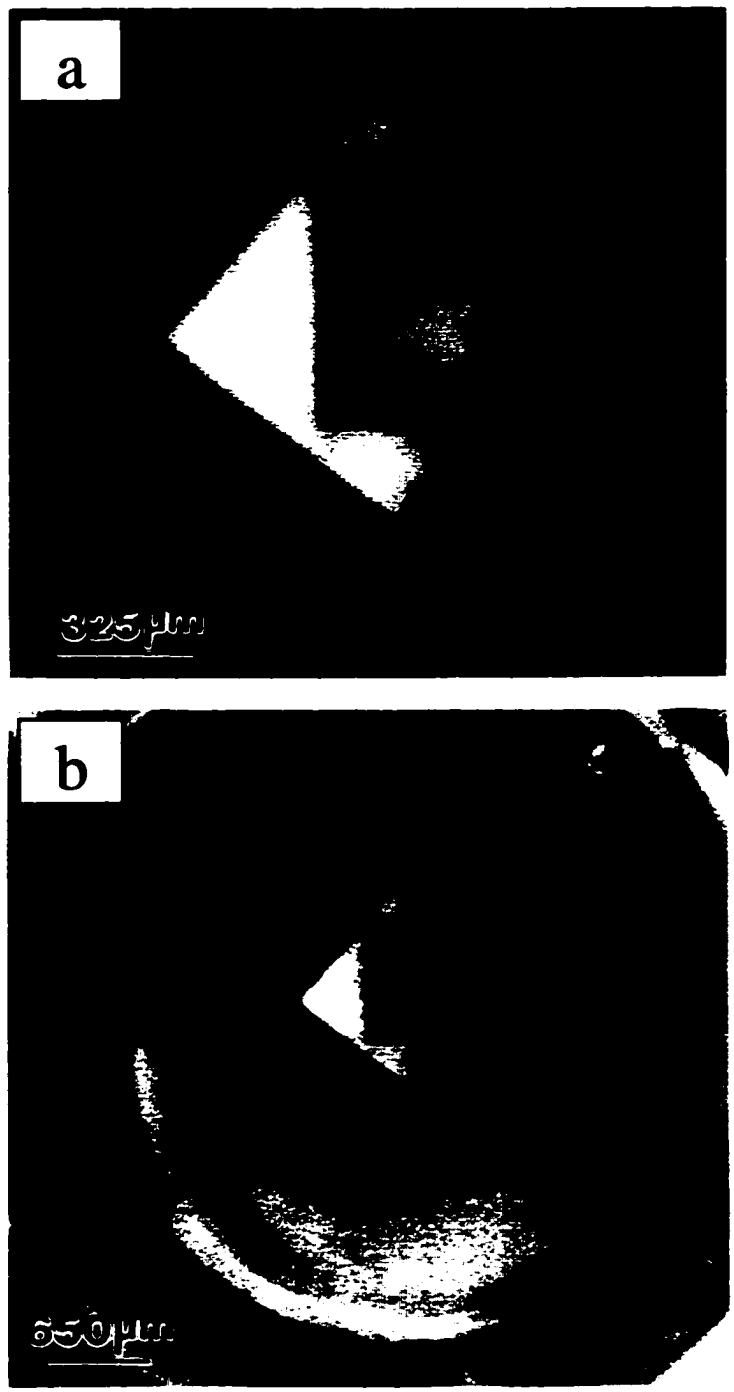

Figure 1.6. a) Ion-induced secondary electron image while sputtering an area within the oxidized region with Ar ions, and b) Lower magnification image after the completion of the ion milling.

1.4 Sample preparation

The surface of a solid exposed to atmospheric pressure is not a simple system to study. Its complexity is due to the presence of an adlayer of various adsorbates, whose chemical compositions and geometrical structure are not well-defined because the fresh, clean surface is very reactive. Therefore, the first step in a surface investigation, especially of the initial adsorption of a few monolayers, requires the preparation of a clean, contaminant-free, well-ordered, and characterized substrate. Several techniques can be used to produce such a substrate in UHV conditions, such as cleavage (limited to brittle materials), cycles of ion bombardment and thermal annealing, and evaporation of thin films.

Since the present studies involved the growth of thin metal films on semiconductor substrates, the sample preparation will focus on Si and Ge surfaces. Samples are prepared ex-situ by standard TEM sample preparation techniques. Three-mm disks are cut from wafers of 400 μm thickness using an ultrasonic cutter. Afterwards, they are mechanically thinned to 150-200 μm, dimpled, and polished to roughly 20-30 μm at the center. Before moving to the next step, it is important to thoroughly remove all the glue residue, since it is difficult to get rid of it during subsequent processing. Electron-transparent areas can be obtained either by ion milling or chemical etching. Since a great level of defects is induced by the former, the chemical etching is preferred. The samples are placed in a Teflon holder and, for the case of Si, dipped in a solution of HF:HNO_3 1:9. For a successful etching, it is necessary to constantly stir the solution with a magnetic stirrer. The samples are etched until small

holes, usually surrounded by electron-transparent areas, appear. The process is monitored by projecting a beam of light from the back of the specimen. The case of Si is straightforward: the thinner area changes color from red to orange, yellow, and white just before perforation. If the process is too rapid, the solution is replaced with a diluted one. In Ge samples, just a dark red spot appears, followed quickly by a hole, thus extra care should be used. As an etchant for Ge specimens, a diluted solution of HF:HNO_3 1:10 proves to avoid the formation of pin holes. The specimens are carefully washed and then mounted in Mo rings that are the sample holders designed for SPEAR. Figure 1.7 shows a schematic of the Mo ring. A key point of the ex-situ sample preparation is to avoid or minimize contamination through improper handling or employing unclean hardware or poorly deionized water.

For the in-situ processing, the samples are introduced into SPEAR. Typically, they are transferred to the analytical chamber for cleaning and chemical characterization. The as-etched samples display in the XPS spectra (Figure 1.8a) the presence of O, C, and maybe F from the chemical etchant. Both sides of the specimens are cleaned through cycles of low energy ion milling and thermal annealing. Oxygen ion beams work best for C contamination, followed by argon ion bombardment to clean the oxidized layer. Implanted ions and defects induced in the crystals due to ion milling and are eliminated by thermal annealing, usually using direct electron irradiation (Figure 1.8b). The electron beam bombardment is directed from the back side of the specimens in order to avoid the possibility of current-induced effects (Grozea, Landree, and Marks 1997). For the Mo

rings, decontamination is achieved using resistive annealing. In contrast to Si, the as-etched Ge samples have less contamination and are easier to clean (Figure 1.9).

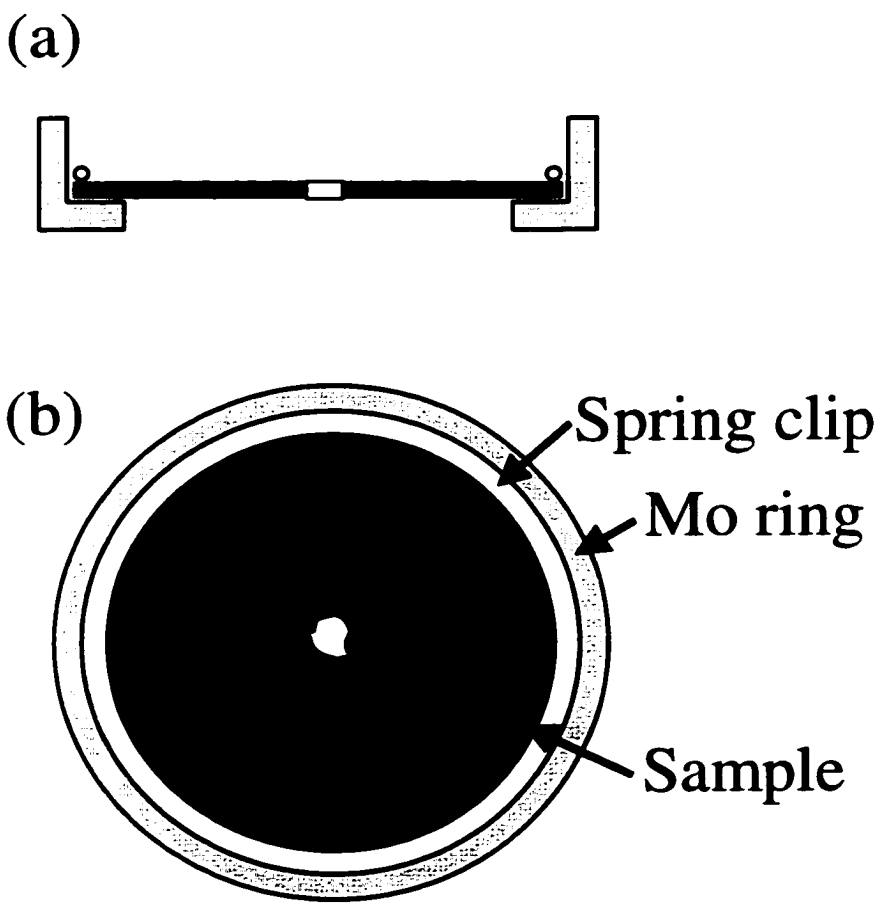

Figure 1.7. Schematic diagram of the Mo ring used as a sample holder in SPEAR. a) Cross-section side view, and b) Top view.

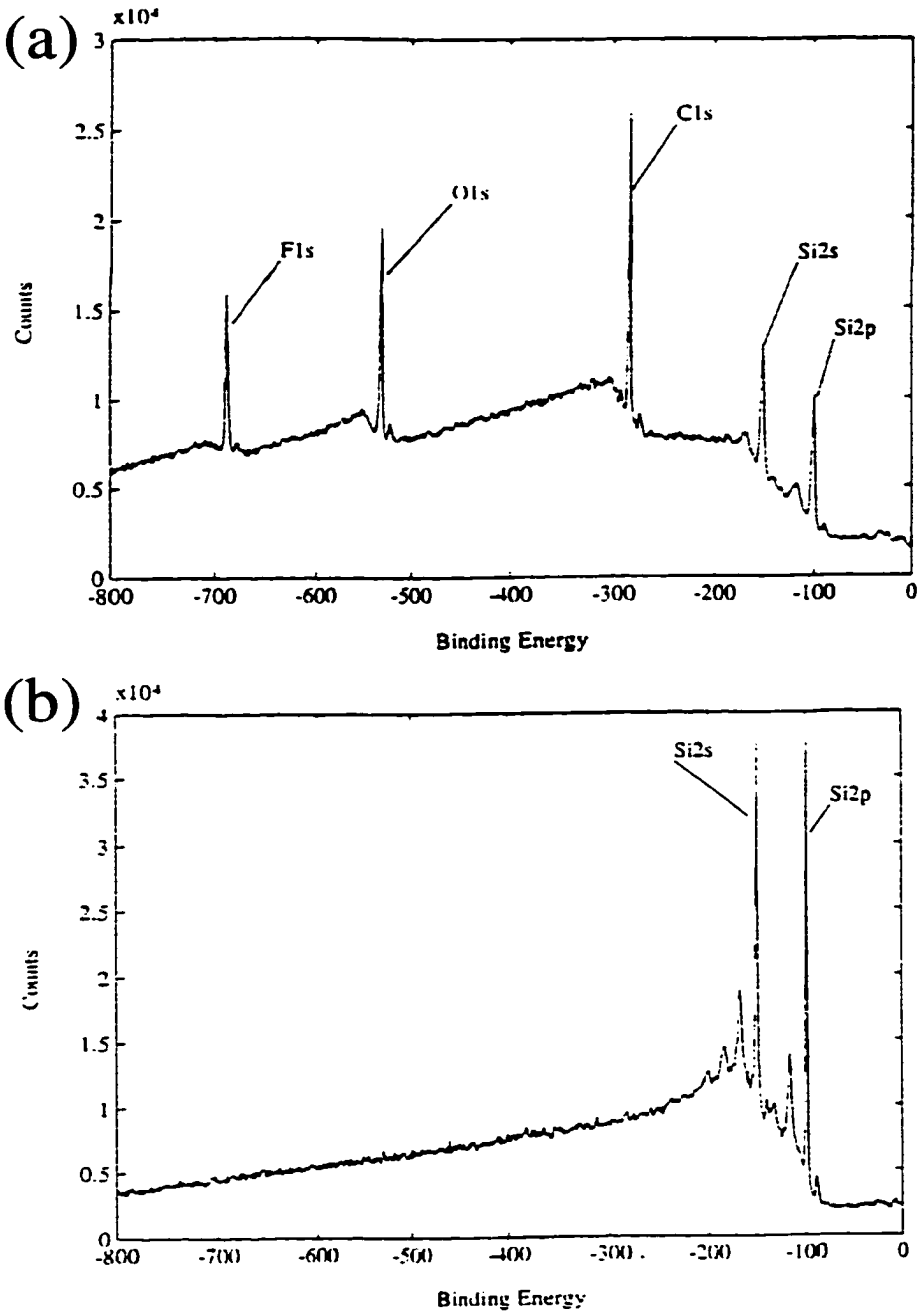

Figure 1.8. XPS spectra from a Si sample. a) As-etched surface, and b) Clean surface after cycles of ion milling and thermal annealing.

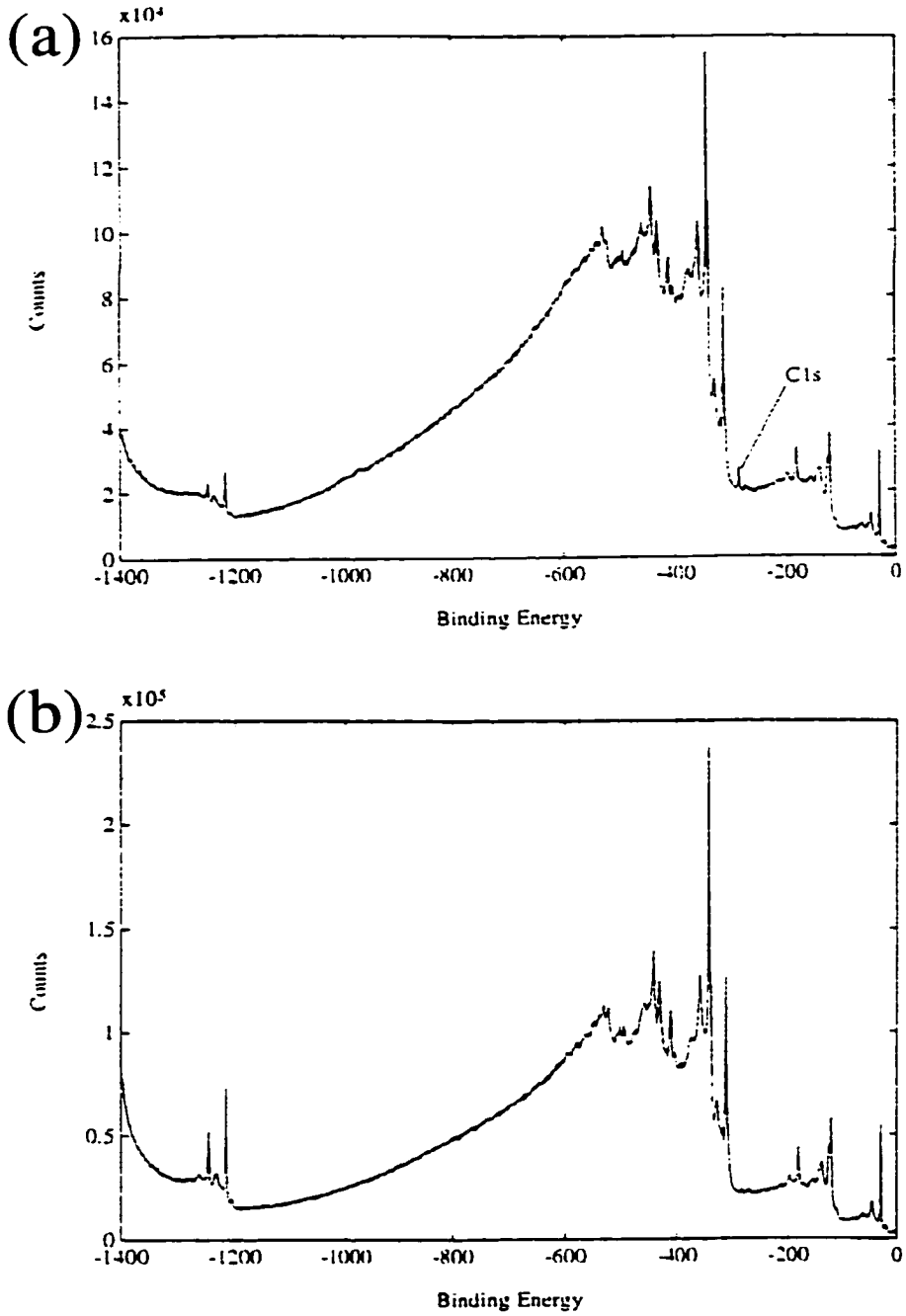

Figure 1.9. XPS spectra from a Ge sample. a) As-etched surface, and b) Clean surface after cycles of ion milling and thermal annealing.

The cycles of ion milling and thermal annealing are iterated several times before suitable surfaces are obtained. The final specimens should be thin, with low surface

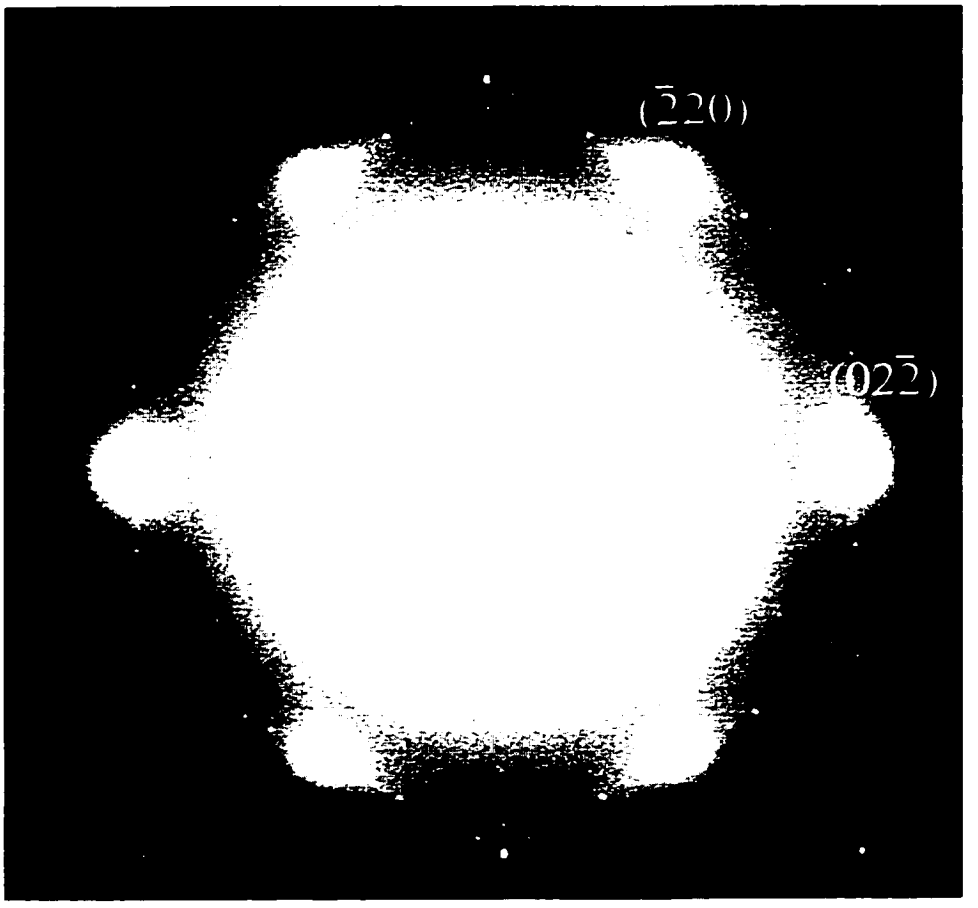

Figure 1.10. Diffraction pattern corresponding to the Si(111)-(7x7) surface reconstruction.

defect concentration, and reconstructed. The cleanliness of the substrate surface after treatment is monitored by surface chemical characterization techniques, such as XPS and AES, until the contamination levels are at or near the detection limit of the instruments, and by observing the strength and sharpness of surface superlattice diffraction spots by TED (since inducing native reconstructions is highly sensitive to the presence on the surface of small amounts of adsorbate atoms). Figure 1.10 displays the diffraction pattern corresponding to the Si(111)-(7x7) native reconstruction.

CHAPTER 2:

DETERMINATION OF THE ATOMIC GEOMETRY OF SURFACE STRUCTURES

A complete understanding of surface phenomena in electronic materials requires knowledge of the atomic arrangement. The investigation of the detailed atomic structure of a metal-on-semiconductor overlayer is of fundamental interest in surface physics because of its influence upon surface and interface properties such as Schottky barrier formation, surface metallization, and surface states.

2.1 Initial model

Diffraction techniques, while being very powerful for accurate refinement of the atomic positions, depend on the quality of the initial model of the structure. Direct Methods are applied to find an initial estimate for the refinement of atomic models using a Minimum Relative Entropy method coupled with a genetic algorithm for global optimization (Landree, Collazo-Davila, and Marks 1997; Marks and Landree 1998;

Marks, Bengu et al. 1998).

From diffraction techniques, only beam intensities/moduli of the structure factors can be obtained. To restore the charge density in the x-ray case or the scattering potential in the case of electron diffraction, the phases are also necessary. Direct Methods solve the diffraction phase problem using the probability relationships which exist between the intensities and the phases of the diffracted beams (Woolfson and Fan 1995). This is achieved through a routine search of sets of phases for a given set of measured intensities which best satisfy these probability relationships. The feasible solutions are defined by some figure of merit, and are in the form of potential maps generated using measured beam intensities and plausible sets of phases which satisfy self-consistent conditions. The maps are then used to construct initial models of the investigated atomic structure. Finally, the models are discriminated upon based on the comparison of the calculated and measured structure factors/beam intensities using, in general, a χ^2 minimization.

For the case of a structure with N non-overlapping identical atoms, a complete set of unitary structure factors U(**k**) will satisfy the Sayre equation:

$$U(\mathbf{k}) = N\sum_{\mathbf{h}} U(\mathbf{k}-\mathbf{h})U(\mathbf{h}) \qquad (1)$$

If some initial phases are known, the Sayre equation can be used to generate the missing phases via the Tangent Formula. The new phases are then fed back iteratively into the Sayre equation to restore all the missing phases and a self-consistency test is performed at each iteration. The process is not a true minimization, but rather a successive approximation method similar to a Picard iteration, and equation (1) can be rewritten as:

$$U_{n+1}(\mathbf{k}) = N\sum_{\mathbf{h}} U_n(\mathbf{k}-\mathbf{h})U_n(\mathbf{h}) \qquad (2)$$

where $U_n(\mathbf{k})$ includes the 'n' th iteration phase estimate. The equivalent of equation (2) in real space is:

$$u_{n+1}(\mathbf{r}) = u_n^2(\mathbf{r}) \qquad (3a)$$

or:

$$u_{n+1}(\mathbf{r}) = \hat{O}(u_n(\mathbf{r})) \qquad (3b)$$

where $\hat{O}$ is a sharpening operator applied on a given real space potential map $u_n(\mathbf{r})$, the Fourier Transform of $U_n(\mathbf{k})$. The operator enhances strong features which may correspond to potential atom sites and minimizes weak ones. After sharpening, the FOM is calculated and the process is iterated as long as the FOM continues to decrease.

This classic Direct Methods approach makes several assumptions that will preclude its straightforward application to solving surface structures. It is assumed that there are no missing strong reflections. The probability relationships on which the method is based are strongly dependent on the relative intensities of the reflections. However, in many surface diffraction patterns, the bulk reflections coincide with the strongest surface reflections, making them unmeasurable and leaving large holes in the data set. Another specific problem for surfaces is that the number of atoms for a particular surface structure is usually unknown. In addition, the atoms that have not been displaced far from bulk positions may well be masked in the phase map.

To overcome the problem of missing information, the Minimum Relative Entropy method uses a function similar to relative entropy as a self-consistent operator. Defining the relative entropy as:

$$S_r(\mathbf{r})=u(\mathbf{r})\ln[u(\mathbf{r})/e\langle u(\mathbf{r})\rangle]+\langle u(\mathbf{r})\rangle, \quad u(\mathbf{r})>0 \qquad (4)$$

$$=0, \qquad u(\mathbf{r})<0$$

where $\langle u(\mathbf{r})\rangle$ is the mean value of $u(\mathbf{r})$, the maximum information case is attained for $u(\mathbf{r})=\langle u(\mathbf{r})\rangle$, which minimizes $S_r(\mathbf{r})$ to zero. An operator based on equation (4) provides an interpolation of the unmeasured reflections and equation (3) becomes:

$$u_{n+1}(\mathbf{r})=u_n(\mathbf{r})\ln[u_n(\mathbf{r})/\langle u_n(\mathbf{r})\rangle] \qquad (5)$$

The application of this operator to a surface potential/charge density map reduces the background noise, minimizing it in the real space phase maps, and favors "peaks" which would correspond to potential atom sites.

To account for the finite number of reflections in a data set due to the measured intensities not extending to infinity, the unitary structure factors are modified by a window function:

$$U^{new}(\mathbf{k})=W(\mathbf{k})U^{old}(\mathbf{k}) \qquad (6)$$

chosen to satisfy, in real space, the equation ($w(\mathbf{r})$ being the Fourier Transform of $W(\mathbf{k})$):

$$w(\mathbf{r})=\alpha w(\mathbf{r})\ln[w(\mathbf{r})/\langle w(\mathbf{r})\rangle] \qquad (7)$$

where α is a constant. The window function can be considered as giving any single non-overlapping atom a relative entropy value of zero. The FOM utilized is selected as a measure of how close the relative entropy is to zero for the experimental reflections:

$$FOM = \sum{}' \left| U_n(\mathbf{k}) - \beta U_{n+1}(\mathbf{k}) \right| / \sum{}' \left| U_n(\mathbf{k}) \right| \qquad (8)$$

where Σ' is a sum excluding $\mathbf{k=0}$ and β is a scalar chosen to minimize the FOM. Since the experimental data set is not perfect, having non-zero errors and measured reflections which do not extend to infinity, a low FOM will correspond only to a plausible solution. However, a low FOM is a necessary condition for a correct solution.

2.1.1. Genetic Algorithm

Since the surface diffraction patterns are usually incomplete and noisy, there may be several possible local minima in the solution space, thus requiring the use of a global search routine such as a genetic algorithm. In the present method, the genetic algorithm is utilized mostly for the exploration of the possible unique solutions as opposed to looking for a single best solution.

Initially, phases are assigned randomly for a subset of the strongest reflections, usually 5-15% of the total number of beams. This set of starting phases is generated a total of **N** times, making a collection later referred to as a "population". For each starting set of initial guess phases, the phases of the remaining reflections are generated using the Minimum Relative Entropy method and a corresponding FOM is calculated. The assigned phases of the reflections from the subset are then translated into binary notation and strung end-to-end to create a single string of bits, or a "chromosome". Each chromosome will be considered with its associated FOM.

The genetic algorithm will act upon the chromosomes by simulating a process of natural selection (for more details Goldberg 1989). The initial set of chromosomes will be considered as the first set of "parent" chromosomes. Using the value of the FOM as a

likelihood for survival, the genetic algorithm selects two favorable (low FOM) parents, switches a random number of phases between them ("cross-over"), generating two new guesses or "children" for the starting phases, and introduces a degree of mutation in which the values of some of the phases are randomly changed. A number of parents with low FOM are just copied to the new population; this is an elitism process which preserves the best solutions. Thus a new population corresponding to a new set of plausible solutions evolves and is subsequently evaluated and assigned a FOM through Minimum Relative Entropy. The entire process is iterated for a given number of cycles or "generations".

The efficiency of the genetic algorithm as a global search technique is due to the large number of schemata calculated and its specific way of processing them (Holland 1975). A schemata is a similarity template describing a subset of chromosomes with similarities at certain positions, similar to phase combinations for different structure factors. Even for the case when the number of parents, **N**, is the same as the number of children, the algorithm processes around $\mathbf{N}^3$ schemata. Shorter schemata are favored and passed along each generation since crossover disrupts longer schemata by occurring within their length. Schemata being the equivalent to favorable phase combinations, the good combinations will be targeted and preserved.

2.2 Structure completion

Once solutions are generated by Direct Methods technique, the completion of an initial model may require the help of additional methods. Possible approaches include

the use of Fourier difference maps (Dorset 1995) or of a heavy-atom holography algorithm (Marks and Plass 1995).

Figure 2.1 shows the phase map generated for the known Si(111)-($\sqrt{3}$x$\sqrt{3}$)R30°Ag structure from TED data (Grozea, Landree et al. 1999). Both Ag and Si sites are very well resolved, circular in shape, and no artifacts are present. For this case, the map approaches restoration. For the Si(111)-(3x1)Ag surface, the potential map shown in Figure 2.2 displays four well-resolved peaks (A-D) along with an elongated area labeled E. The region E is considered to represent either two partially-occupied atom sites or an artifact arising from the lack of a complete set of intensities (Collazo-Davila, Grozea, and Marks 1998). Figure 2.3 displays the charge density map obtained from x-ray data taken from a Ge(111)-(4x4)Ag surface. All the atom sites are well resolved, but due to the relatively similar scattering factors of Ag and Ge it is not clear which sites are occupied by Ag atoms and which by Ge atoms (Collazo-Davila et al. 1998). Sometimes only part of the surface structure can be identified in the map. Figure 2.4 shows an initial fragment of the Si(111)-(6x6)Au reconstruction with twenty Au positions and three weaker Si sites (Grozea et al. 1998; Marks, Grozea et al. 1998).

To complete the structure, such as for the case from Figure 2.4, or to solve the problems raised by maps such as those in Figure 2.2 and Figure 2.3, a new step in the analysis is performed. Iterative steps of refinement of the atomic positions are combined with heavy-atom holography to determine new sites. Figure 2.5 shows the flow chart of the process. Cross-correlation of a map generated for a single atom with the phase map generated by Direct Methods produces a new map, highlighting the most likely atomic

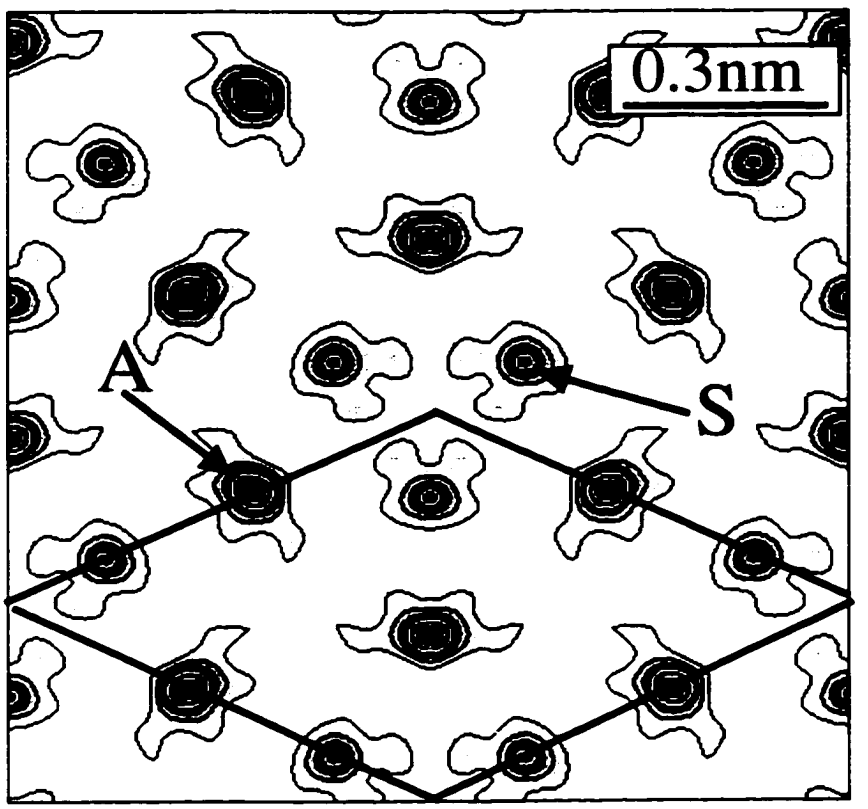

Figure 2.1. Contour map of the scattering potential generated using phases estimated through Direct Methods for the Si(111)-($\sqrt{3}$x$\sqrt{3}$)R30°Ag structure. One out of the three symmetry-equivalent sites is arrowed for Ag and Si respectively. The primitive unit cell is indicated by solid lines.

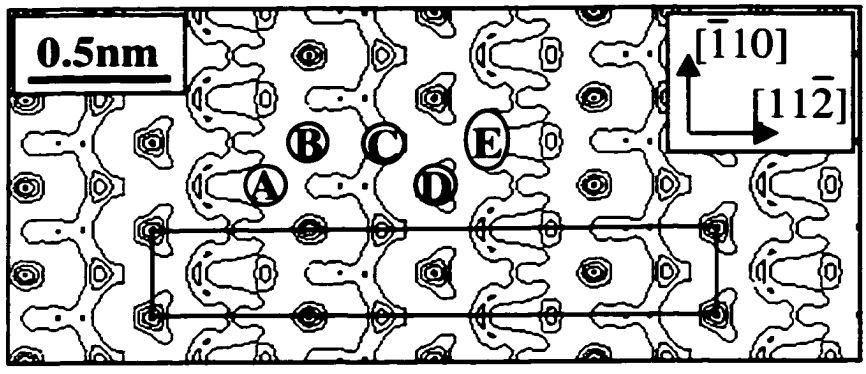

Figure 2.2. Contour map of the scattering potential found for Si(111)-(3x1)Ag. Peaks A, B, C, and D correspond to Si atoms and peak E corresponds to two half-occupancy Ag sites. A centered (6x1) unit cell is drawn, showing the cm symmetry.

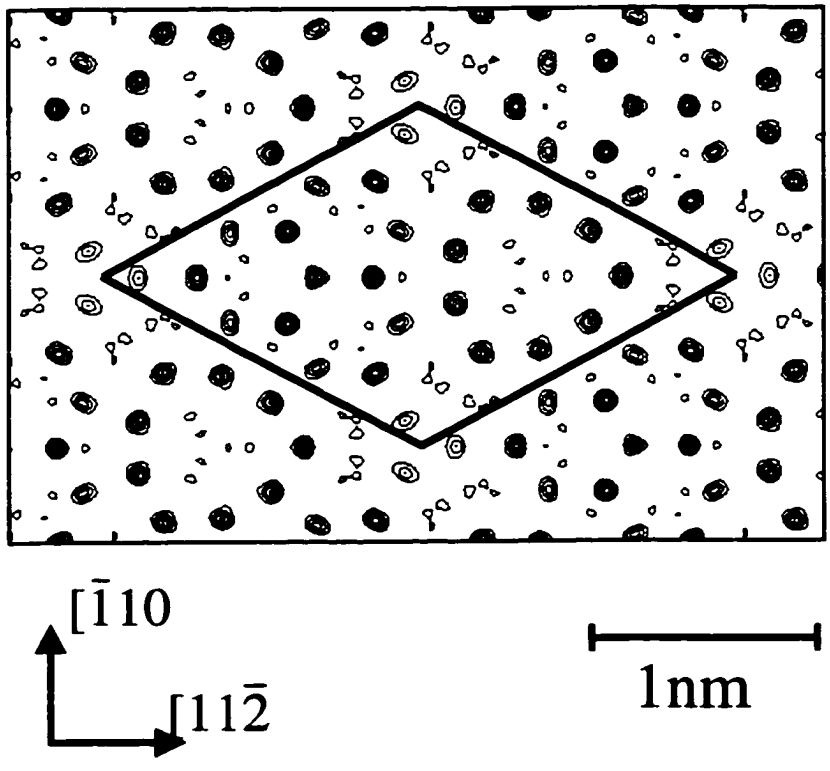

Figure 2.3. Contour map of the charge density map generated by Direct Methods, showing the best solution for Ge(111)-(4x4)Ag. The primitive unit cell is indicated by solid lines. (Courtesy of Dr. C. Collazo-Davila).

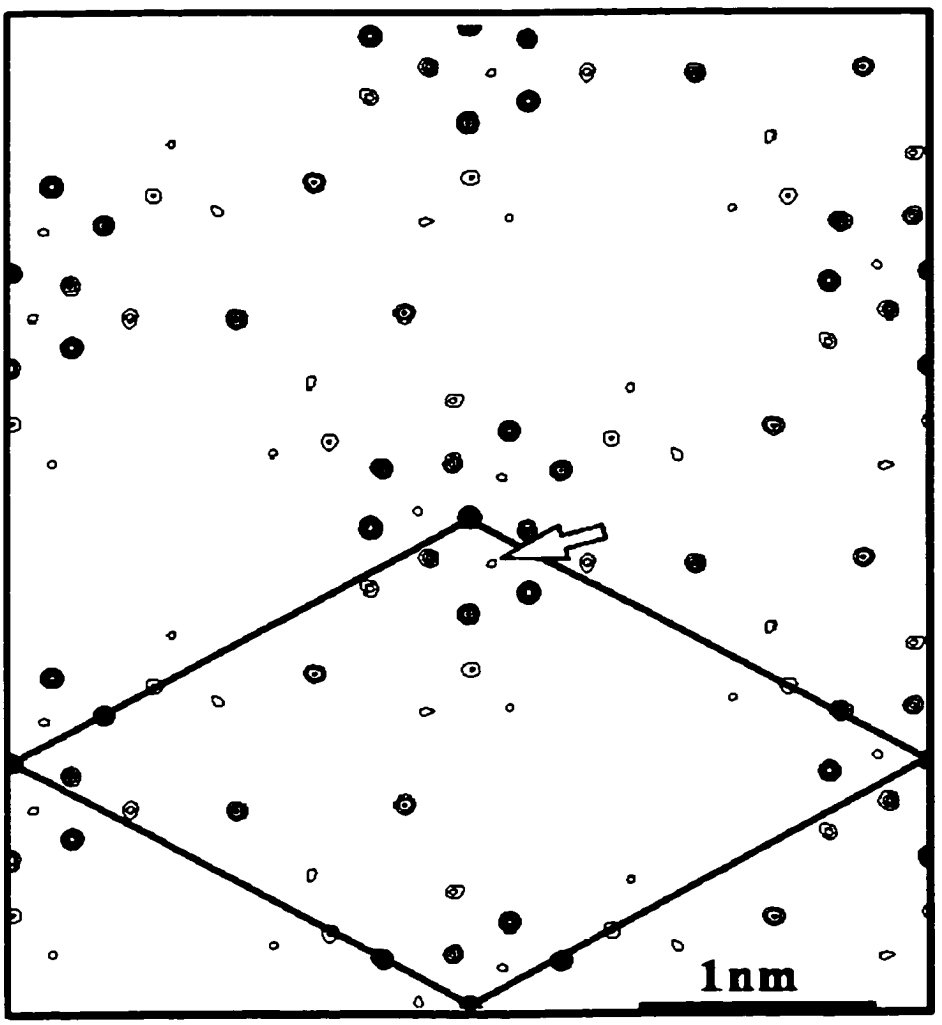

Figure 2.4. Contour map of the charge density calculated by Direct Methods, showing an initial fragment of the Si(111)-(6x6)Au structure. A weaker Si site, one of the three symmetry-equivalent sites, is arrowed, and all the other peaks correspond to Au sites. The primitive unit cell is indicated by solid lines.

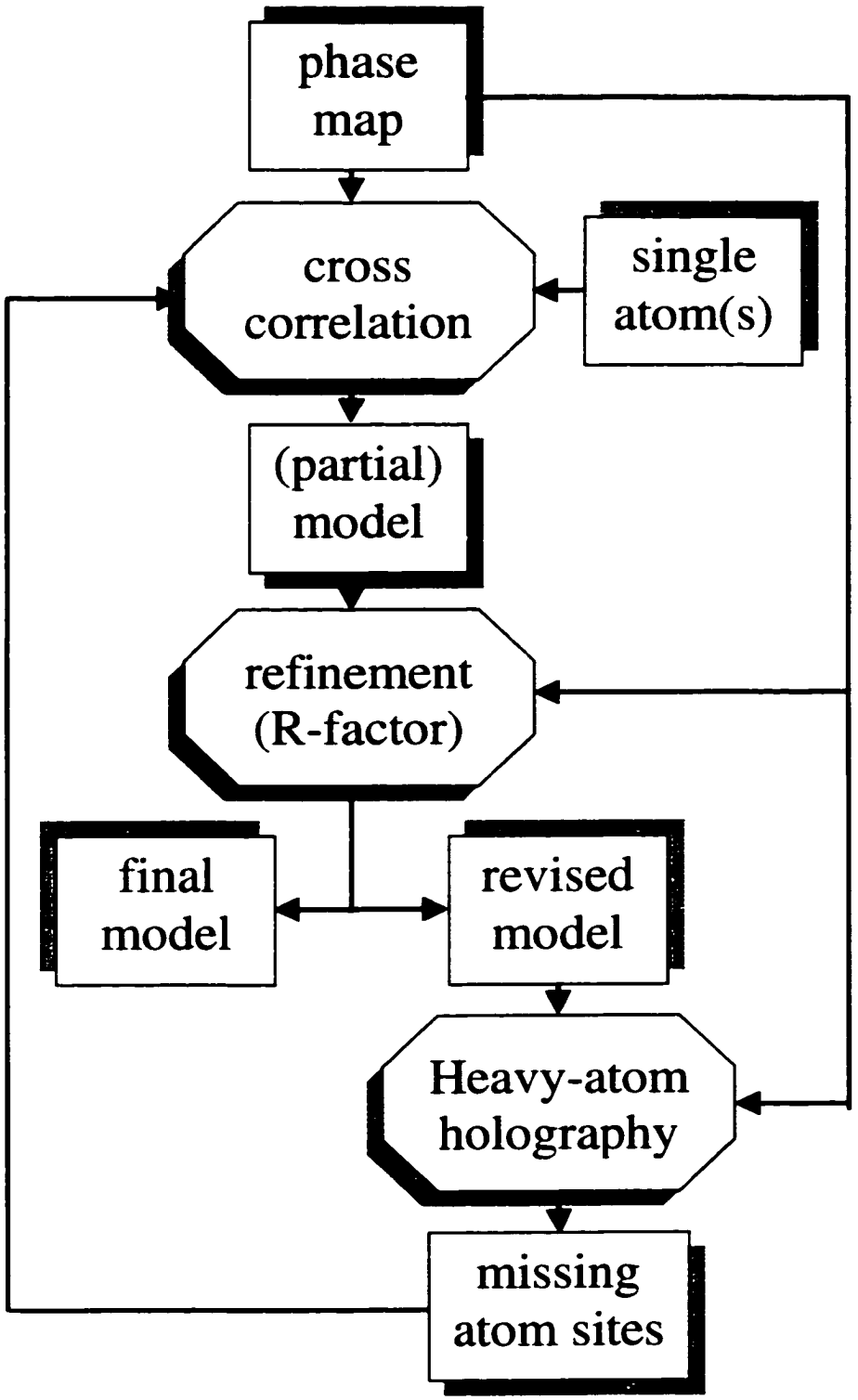

Figure 2.5. Flow chart of the iteration process of atomic position refinement/heavy-atom holography.

positions within the unit cell. The program lists all the possible sites in decreasing order of the peak intensity. The effect of each atom is estimated by calculating the diffraction intensities of the resulting structure and comparing them to the measured intensities, and only the additions leading to a better diffraction pattern fitting are considered.

The atomic positions are then refined using an R-factor defined as:

$$R \equiv \frac{\sum_{j=1}^{N} \left| I_{expt}^{j} - I_{calc}^{j} \right|}{\sum_{j=1}^{N} I_{expt}^{j}} \qquad (9)$$

where I_{expt} and I_{calc} are the experimental and calculated beam intensities, and N is the number of data points. After the refinement, new possible atomic sites are generated using the heavy-atom holography algorithm. The sites are also listed in decreasing order of peak intensity and only the most intense possible positions are selected during each iteration. The effect of placing an atom on a suggested site is evaluated through diffraction pattern fitting.

In the example from Figure 2.2, the area E was finally modeled as two half-occupied Ag sites, and the A-D sites as being Si atom positions. From the map shown in Figure 2.3, many different permutations of the Ag and Ge atoms distributed on the well-resolved atomic sites were tested to find the model yielding the lowest R-factor. The case for the Si(111)-(6x6)Au structure, Figure 2.4, will be discussed in detail later.

Heavy-atom holography utilizes the interference between a known wave, $\Psi(\mathbf{u})$, and an unknown wave, $w(\mathbf{u})$, in the diffraction plane to determine the phase. Starting

from an estimate for the wave $\Psi(\mathbf{u})$ obtained from a χ^2 minimization with a given number of atoms, the unknown wave $w(\mathbf{u})$ must minimize R^2 in equation (10):

$$R^2=[I(\mathbf{u})-\alpha|\Psi(\mathbf{u})+w(\mathbf{u})|^2]^2 \qquad (10)$$

where $I(\mathbf{u})$ is the experimental diffraction intensities of a single domain (in the simplest case) and α is a scaling factor determined by the χ^2 minimization. For the case when R=0, equation (10) is the analog of the general form of on-axis holography where both sidebands are invertible, hence the name of the algorithm. The Fourier transform of $w(\mathbf{u})$ is an approximation of the residual wave, and candidate atomic locations are displayed in the image.

2.3 Refinement

As a final step, the model's atomic positions are refined, usually using a reduced χ^2 minimization (Bevington, 1969), with n=2 in equation (11):

$$\chi^n = \frac{1}{N-m}\sum_{j=1}^{N}\left(\frac{\left|\mathbf{I}_{\text{expt}}{}^{j}-\mathbf{I}_{\text{calc}}{}^{j}\right|}{\sigma^{j}}\right)^n \qquad (11)$$

where I_{expt} and I_{calc} is the experimental and calculated beam intensity, σ the error of the measured intensity, N the number of data points, and m the number of fitting parameters. The value of χ^2 provides a measure of the probability of making a given set of observations. For a perfect fit of the model to the measured beam intensities within the experimental uncertainty, the χ^2 value should approach 1. The χ^2 analysis assumes Gaussian distributed errors between the measurements and the simulations. For the case

of exponentially distributed errors, a robust form χ can be used (n=1 in equation (11)). The χ factor is analogous to a χ^2 analysis, with a good fit of the model equivalent to a value of χ near 1, but it is less sensitive to outliers in the data set.

2.4 Discussion

The only pieces of information fed into the Direct Methods analysis are the experimental intensities and an assumption about the structure symmetry. The output is a list of plausible solutions, phase maps obeying the imposed symmetry, ranked in order of FOM and used as a starting point for constructing possible models of the surface structure. These maps can be rather accurate restorations of the scattering potential/two-dimensional charge density (electron/x-ray data), provided that the data set has small experimental measurement errors, is complete, and is not affected by non-kinematical scattering. If this is the case, the bright circular features displayed in the phase maps can be interpreted as atom sites since the projection of the charge density around individual atoms can be approximated as being circular. However, the missing information that often characterizes experimental data sets will induce distortions of features' shapes as well as artifacts.

In effect, with no additional information other than the symmetry group and the beam intensities, one has reduced the number of solutions from an infinite number of possible arrangements of atoms to some finite number of solutions. These solutions can be further discriminated by a χ^2 minimization and comparison with results from other surface sensitive techniques.

The application of Direct Methods to solving surface reconstructions is a new area which will continue to grow in scope and magnitude in the near future. The major differences between bulk and surface diffraction data that precluded the application of Direct Methods to surface determination have been overcome. In particular, this technique has proven useful not only as an interpolation tool for estimating unmeasured reflections, but also as an instrument for extrapolating information to higher spatial frequencies. In principle, this method offers the possibility of estimating intensities from beam reflections which coincide with bulk or 1x1 lattice intensities, information which has mostly gone unused or ignored.

Cases of surfaces where twinning is present or large structures where only an initial fragment is present in the phase maps are areas which require further development. In the latter case, the final model obtained after the heavy-atom holography method is often path dependent, requiring careful process monitoring. Hence, a more automated method is desired. More interestingly, the extension of the Direct Methods analysis to three-dimensional surface diffraction data (including the rel-rod information from x-ray surface diffraction measurements) is under investigation and already shows some degree of success (Marks 1999).

A more comprehensive way of approaching the phase problem is to consider the Direct Methods as a feasible set problem. Within this frame, the problem of retrieving the phase information lies in finding the intersection of several sets. One set should consists of all functions which satisfy all of the known real-space constraints, and other all functions which satisfy all reciprocal-space constraints. A member of the intersection

of all the sets will be the solution of the problem. An extensive presentation of this approach and its specific application to solving surface structures is found in Marks, Bengu et al. (1998) and Marks, Sinkler, and Landree (1999).

In the future, progress in both HREM imaging and Direct Methods has the potential to open the way for significant advances in even more challenging areas of research, such as solving the structure of buried interfaces (which by their nature are not accessible to almost all other surface probes), and investigating chemical reactions on reconstructed surfaces.

This is not to suggest that HREM and Direct Methods will be the only tools in surface characterization. To date, both techniques are only weakly sensitive to chemical composition or specific chemical bonding information. Nonetheless, these methods offer powerful tools which, when combined with other surface characterization techniques, can give a complete and accurate view of the surface structure.

CHAPTER 3:

EFFECT OF SMALL PARTICLES ON THE Au/Si(001) INTERFACE FORMATION AT ROOM-TEMPERATURE

Epitaxial thin films are prepared by a wide variety of techniques. Various growth processes, for example, Molecular Beam Epitaxy, require deposition on atomically clean surfaces under UHV conditions. The presence of contaminants, native oxides, or a high concentration of surface defects on the substrate, are known to influence the growth mode (Venables, Spiller, and Hanbucken 1984; Henzler 1996) and reduce the quality of the thin films.

Thin Au films on Si have been continuously investigated since the early seventies due to their importance in integrated circuit device applications. Although the Au/Si metallic contact has been found to be unsuitable for devices because Au atoms diffuse extremely quickly and serve as deep-trap centers in Si (Milner 1973), this interface is still of interest. Most studies concentrated on the Si(111) interface, and there are fewer

reports on the Si(100). A detailed picture of the interaction of Au on the Si(100) surface is not yet available.

Despite the fact that Au and Si are known to form no thermodynamically stable bulk compounds (Okamoto and Massalski 1983), several experiments apparently indicate that the Au/Si interface is diffuse even for room temperature deposition. This model of the interface, containing an intermixed Au-Si alloy (Braicovich et al. 1979; Perfetti et al. 1980; Salvan, Cros, and Derrien 1980) is in contrast with results suggesting that the room temperature grown interface is abrupt with the contact made by metallic Au on the Si substrate (Taleb-Ibrahimi et al. 1984; Yeh et al. 1993). Several studies also support the diffuse interface, but with a critical coverage below which the interface is abrupt (Okuno et al. 1980; Iwami et al. 1988; Meinel and Katzer 1992).

In the first part of this chapter, the effect of electron beam heating during the preparation of clean silicon surfaces suitable for epitaxial studies in UHV conditions is presented (Grozea, Landree, and Marks 1997). This is followed by results from the investigation of initial growth of Au on Si(001) at room temperature, and the importance of Au clusters size effects (Landree et al. 1997).

3.1 Surface roughening by electron beam heating

Silicon is one of the most common substrates for epitaxial growth, owing to its extensive use throughout the semiconductor industry. To clean the surface, several techniques are used based on wet chemical etching, ion sputtering, and thermal annealing.

High-temperature thermal treatment, in the range of 1000°C - 1200°C (Shiraki et al. 1978; Sugiura and Yamaguchi 1980) has been used to achieve a clean Si surface free of contaminants for thin film growth. However, the high temperatures involved in this method induce a high level of defects (dislocations, stacking faults, and slip lines) in the substrate, along with dopant diffusion and modification of the initial dopant concentration profile.

To avoid high-temperature treatment problems, several low-temperature techniques have been developed. Direct thermal radiation (Shiraki et al. 1978; Ishizaka and Shiraki 1986), passing current through the sample (Becker and Bean 1977; Takayanagi et al. 1985), laser annealing (Zehner, White, and Ownby 1980; Jong et al. 1983), galliation (Wright and Kroemer 1980), ECR (electron-cyclotron-resonance) assisted hydrogen plasma (Gao, Hariu, and Ono 1987; Ishii and Taga 1994), and direct electron beam annealing (Monch, Koke, and Krueger 1981; Wang, Liu, and Wang 1987; Jayaram, Xu, and Marks 1993; Plass and Marks 1995) are only a few of the many thermal techniques currently available. Direct electron beam annealing has an advantage over direct thermal radiation and conventional electrical heating of providing rapid temperature control and lower levels of outgassing. Also, this method does not have the post-treatment contamination problems associated with galliation or ECR plasma techniques.

3.1.1 Experimental

Samples were prepared ex-situ by standard TEM sample preparation techniques. Three-mm disks were cut from p-type doped Si(001) wafers of 13.5-18.5 Ωcm, mechanically thinned, dimpled, and polished to roughly 30 μm at the center. After chemical etching the samples to perforation in an $HF:HNO_3$ 1:9 solution, they were introduced into a surface preparation and analysis system (SPEAR).

Once inside the system, both sides of the samples were cleaned using cycles of low energy (1 keV) oxygen and argon ion milling followed by direct electron beam annealing. The annealing was performed at 3 keV and 0.1 mA beam current using an EMG-14 Kimball Physics electron gun. To obtain a strong and sharp (2x1) surface diffraction pattern, the specimens were annealed at 740°C for 4-5 min, and then at 550°C for 30-45 min.

Surface characteristics were monitored with XPS, AES, and TEM. Off-zone TED and dark field images were recorded at room temperature using a beam voltage of 200 kV to limit the surface damage effects of the microscope electron beam to the during investigations.

3.1.2 Results

A typical clean Si(001) sample displayed a strong 2x1 reconstruction in the TED pattern, a low concentration of defects, and well-ordered monoatomic surface steps in dark field images. For this experiment we deliberately selected samples with a relatively high density of bulk defects, higher than we normally use, so that the same area could be

repeatedly identified. Figure 3.1a is a dark field image of the Si(001) surface taken using a (220) type reflection and showing well-ordered steps. It was observed that the fringes from the surface steps did not overlap. The non-existence of crossing steps can be attributed to the presence of well-ordered steps on only one side of the specimen, although XPS and AES show that both sides had contamination levels at or near the detection limits of the instruments. Plan-view TEM images show both sides of the sample imaged at the same time, and one cannot distinguish on which surface a particular feature is.

Since the inelastic mean free path of 3 keV electrons in silicon is under 50 Å (Tanuma, Powel, and Penn 1991; Fujita, Schleberger, and Tougaard 1996) and our TEM samples typically have a thickness greater than 200 Å, we inferred that the electron beam irradiation during the thermal treatment induces a disordering of the incident sample surface. We investigated this fact by alternate disordering of the specimen surfaces and subsequent observation in the microscope. The reported results are from several such experiments. To simplify the discussion, we will refer to the side of the sample upon which the electron beam is incident during annealing as side A, and the exit side as side B. Figure 3.2 shows a diagram of the sample's beam exposure: Figure 3.2a displays the direction of the electron beam, and Figure 3.2b,c shows the direction of the Ar ion beam for the case of disordering side B and side A, respectively.

Surface B was disordered using 600 eV Ar ions for 5 seconds at 50° from the surface normal, shown in Figure 3.2b. This ion energy was the minimum attainable with our ion gun and was found to be sufficient to disorder the surface steps. Figure 3.1b shows the

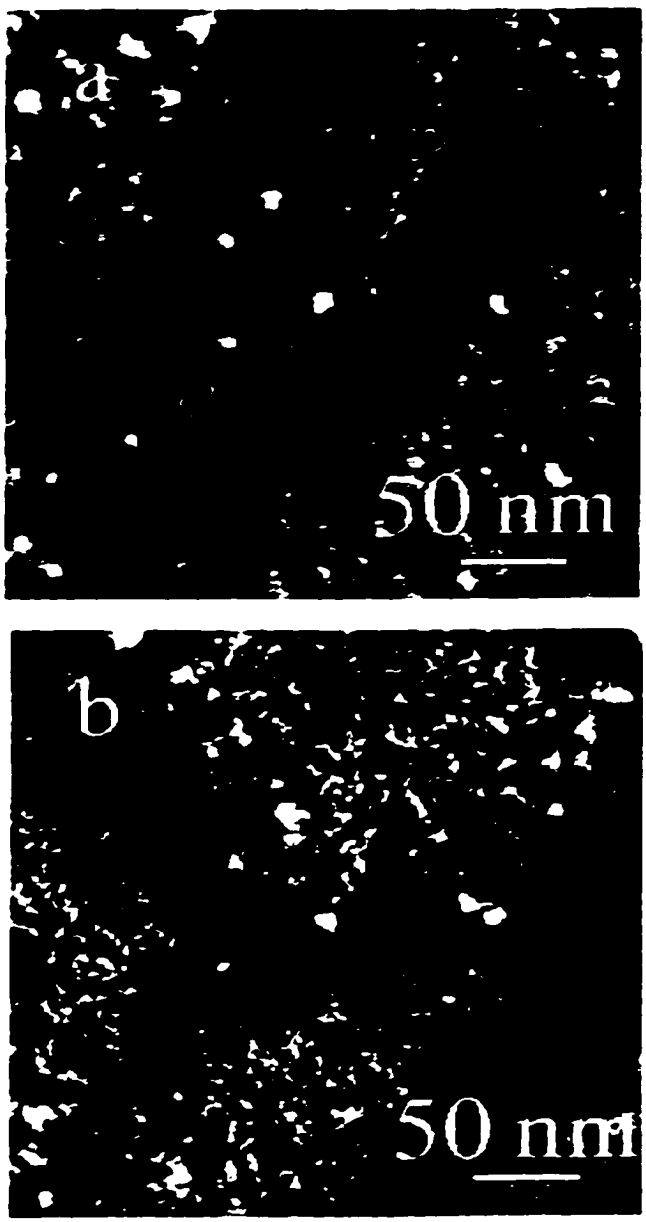

Figure 3.1. Dark field image of the Si(001) surface using the Si(220) reflection: a) Showing well-ordered steps prior to ion beam disordering of surface B, and b) After ion beam roughening, when the surface steps are no longer present. Identical bulk defects can be observed in a) and b). A step has been arrowed for reference.

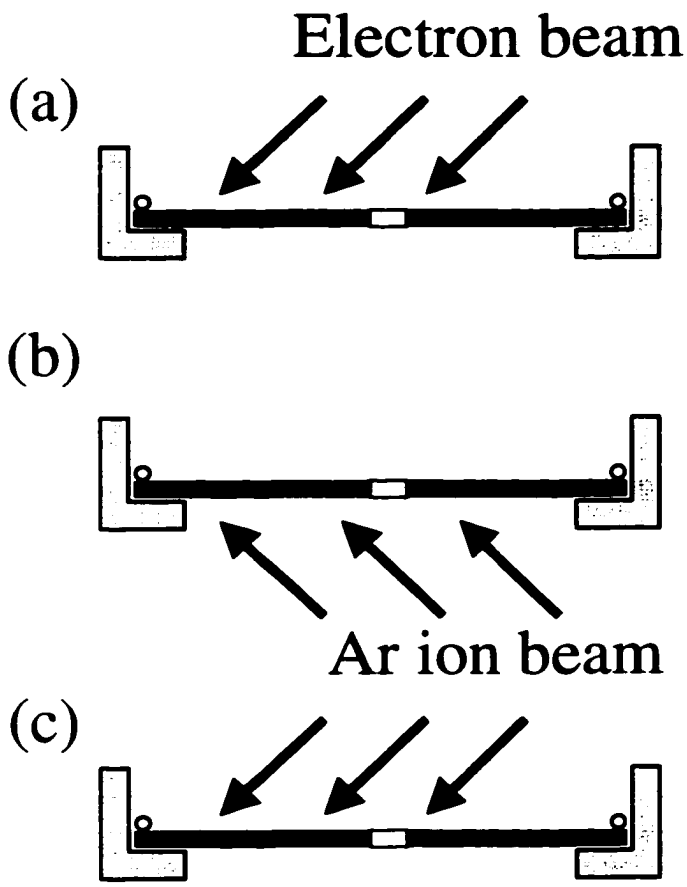

Figure 3.2. Diagram of the sample's beam exposure: a) Direction of electron beam, and Direction of Ar ion beam for b) Side B, and c) Side A.

same area as Figure 3.1a, after ion sputtering, but the steps are no longer present. Common features in the images, i.e. bulk defects, were used to identify the same area.

The initial state of the sample was recovered after reannealing the specimen, and Figure 3.3a is similar to Figure 3.1a, showing a different area of the sample. Using the same conditions for disordering, surface A was Ar ion milled, Figure 3.2c. Figure 3.3b shows the same region as Figure 3.3a, but in this case the steps are still present. The mottled contrast also present in the image suggests a slight additional disordering. Therefore, it can be assumed that the electron beam annealing produced a disordered surface with non-uniformly distributed steps on the incident side of the sample to the electron beam, and well-ordered monoatomic steps on the exit surface.

Reversal of the current direction during resistive heating of the reconstructed Si(001)-2x1 surface has been shown to cause the rearrangement of surface atomic steps (Kahata and Yagi 1989; Ichikawa and Doi 1990). When direct current is supplied in the step-down direction, see Figure 3.4a, 1x2 domains where the dimer axis is perpendicular to the current direction dominate over the 2x1 domains. The roles of the domains convert as the current direction is changed to the step-up direction, Figure 3.4b. This suggests that random surface currents lead to atomic scale disordering during annealing.

LEED or Reflection High-Energy Electron Diffraction (RHEED) techniques could have also been used to detect surface roughness on an atomic scale (Morrison 1990) of silicon samples annealed with a different electron gun, but to the authors' best knowledge there is no such published study.

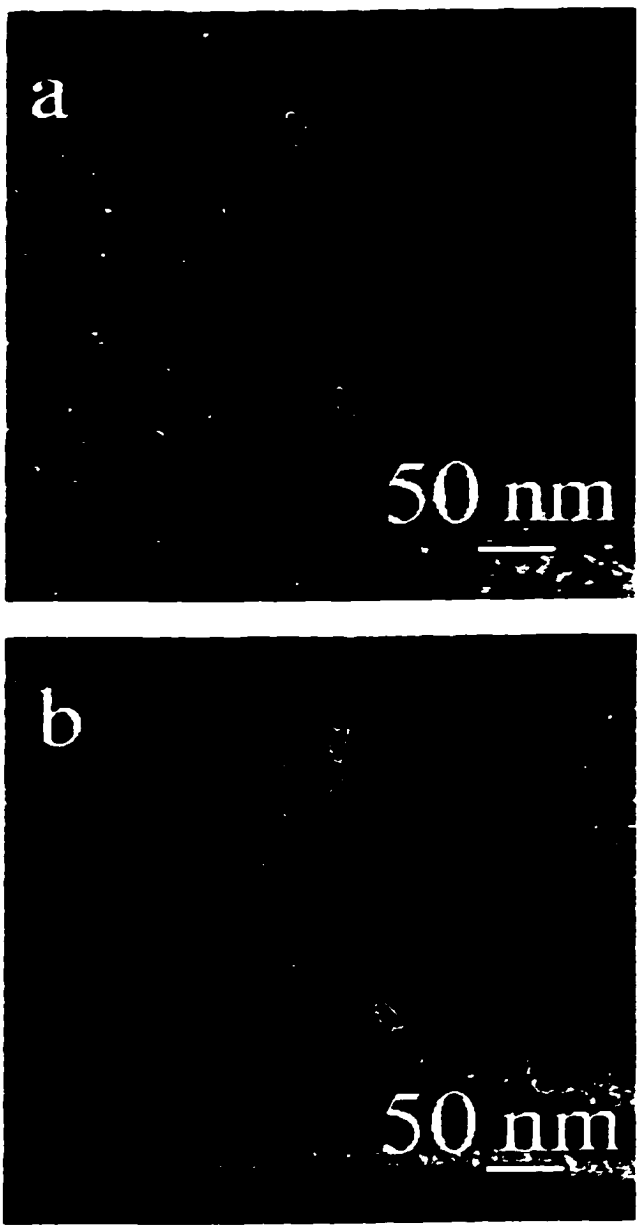

Figure 3.3. Dark field image of the Si(001) surface showing the presence of well-ordered steps: a) Prior to, and b) After the ion beam disordering of the sample surface A. A step has been arrowed for reference.

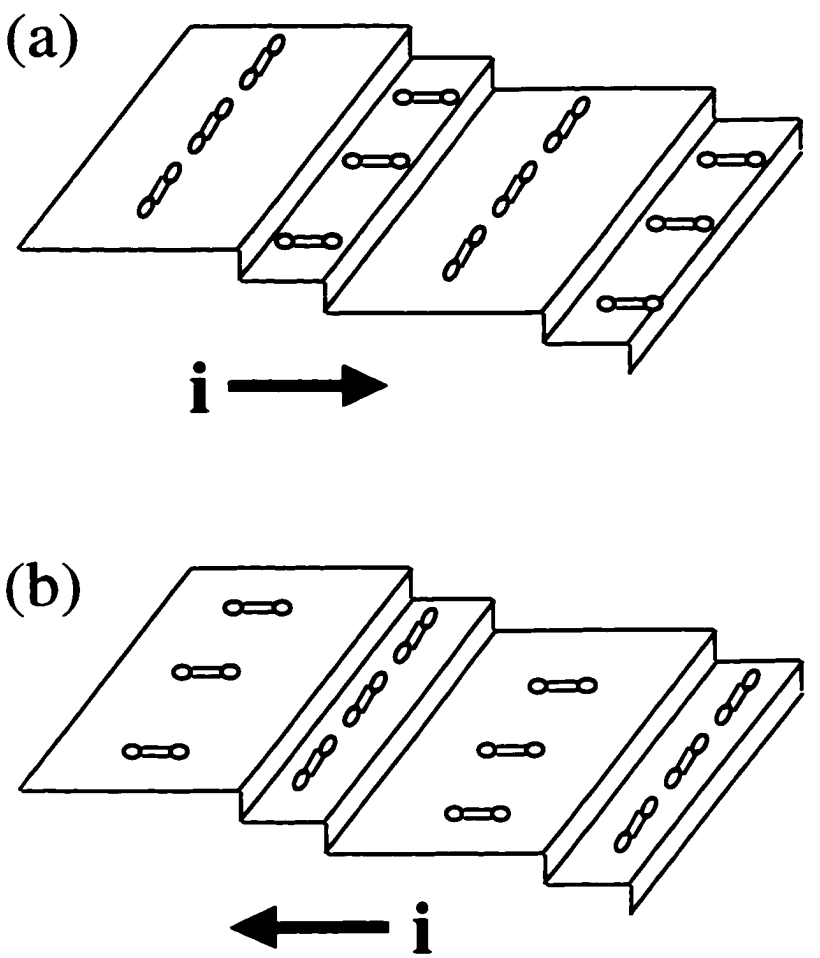

Figure 3.4. Schematic of the Si(001)-(2x1) surface during heating with a direct current showing the motion of monoatomic steps. The direction of the current flow is: a) Step-down, and b) Step-up.

As an example of the important role played by the monoatomic steps, Isikawa et al. (1996) have reported recently improved properties, suitable for nanofabrication, of the oxide layer used as resist mask on a GaAs substrate. Their study suggested that the use of an epitaxial surface with non-uniformly distributed atomic steps led to degraded characteristics of the film. Fabrication of epitaxial thin films on silicon substrates (Miura, Ohtaka, and Shindo 1995) may be similarly influenced by the relative order or disorder of the surface steps.

The application of direct electron beam annealing to thermal treatments has been shown to disorder the incident surface of Si(001) substrates even at energies as low as 3 keV. In spite of successfully cleaning the incident area, the secondary effect, disordering, will potentially reduce the quality of epitaxial thin films grown thereupon. The results have important significance for the use of electron beam annealing for thin film growth and processing.

3.2 Role of small particles in the Au/Si interface formation

In this section, out of the study of room-temperature Au deposition on Si(001)-(2x1) by Landree, Grozea, and Marks (1997), the results pertaining to the role of small Au particles in the interface formation and properties will be reviewed.

The Au/Si interface has continuously being investigated in recent years with various complementary techniques. However, there is no agreement over the morphology of the interface, whether it is abrupt or diffuse, the existence of a room

temperature Au-Si reaction and silicide formation and the necessity of a critical thickness to promote it, or the growth mode of the Au deposit.

There may be several reasons for these experimental discrepancies in the investigation of the initial stages of Au film formation. They have used reconstructed surfaces, but not well-characterized substrates, with a low surface defect density and known domain size and density of surface steps. A rather uncertain Au coverage and the assumption of a layer-by-layer film growth, neglecting the possibility of the formation of metal clusters, in the interpretation of the spectroscopic results can also be counted.

The evidence for the formation of a silicide layer, despite the Au being a very stable, non-reactive metal, was mostly based on the occurrence in the AES spectra of the Si LVV 92 eV peak splitting into two components at 90 and 95eV (Narusawa, Komiya, and Hiraki 1973; Hiraki and Iwami 1974; Nakashima, Iwami, and Hiraki 1975). There is no consent over the required Au coverage; the Si peak splitting is reported to occur from 1 ML of Au to several ML (Okuno et al. 1980; Perfetti et al. 1980; Dallaporta and Cros 1986). Moreover, several studies (Dallaporta and Cros 1986; Cros and Muret 1992) disagree over this correlation.

Structural LEED investigation (Green and Bauer 1976; Oura, Makino, and Hanawa 1976; Perfetti et al. 1980) reported that crystalline gold silicides formed after heat treatment of Au films deposited on Si substrates. However, for depositions at room temperature, only one study (Oura and Hanawa 1979) found a weak, diffuse ring whose spacing did not correspond to either Au or Si at 30 Å of Au on Si(001)-(2x1) surface. Other studies typically mention only a gradual fading of the surface spots into a highly

diffuse background with increasing Au coverage (Green and Bauer 1976; Oura, Makino, and Hanawa 1976; Okuno et al. 1980; Le Lay 1981; Taleb-Ibrahimi et al. 1984).

Also controversial are analyses from UPS and EELS data. Some supported the formation of a silicide at the Au/Si interface, or only as a thin surface layer floating on top of a pure Au metallic layer, at varied Au coverages (Braicovich et al. 1979; Okuno et al. 1980; Salvan, Cros, and Derrien 1980; Lu et al. 1990). Features of the spectra, attributed to early alloy formation, were reinterpreted as being due to Au clustering (Hricovini et al. 1989). Consistent with this possible island growth, a study by Mathieu et al. (1998) also indicates the presence of pure Au clusters in the first few Au layers, in opposition to most reports which generally show a layer by layer growth (Oura and Hanawa 1979; Narusawa et al. 1981; Carrière, Deville, and Maachi 1986).

3.2.1 Experimental

Samples were prepared as described in Section 3.1.1. They need to be sufficiently thin for high resolution electron microscopy and have low surface defect density. The surface morphology was monitored using dark field TEM, due to its possible influence on the film growth mode.

Figure 3.5 is an off-zone HREM micrograph, taken at 200 kV, of a clean Si(001)-(2x1) surface prior to Au deposition, with its diffraction pattern as inset. The lines of contrast correspond to the Si(001) surface dimers along the <110> direction and are spaced 7.68 Å apart. The boundary line separating the 1x2 and 2x1 domains across the center of the image is a single atomic step on the surface.

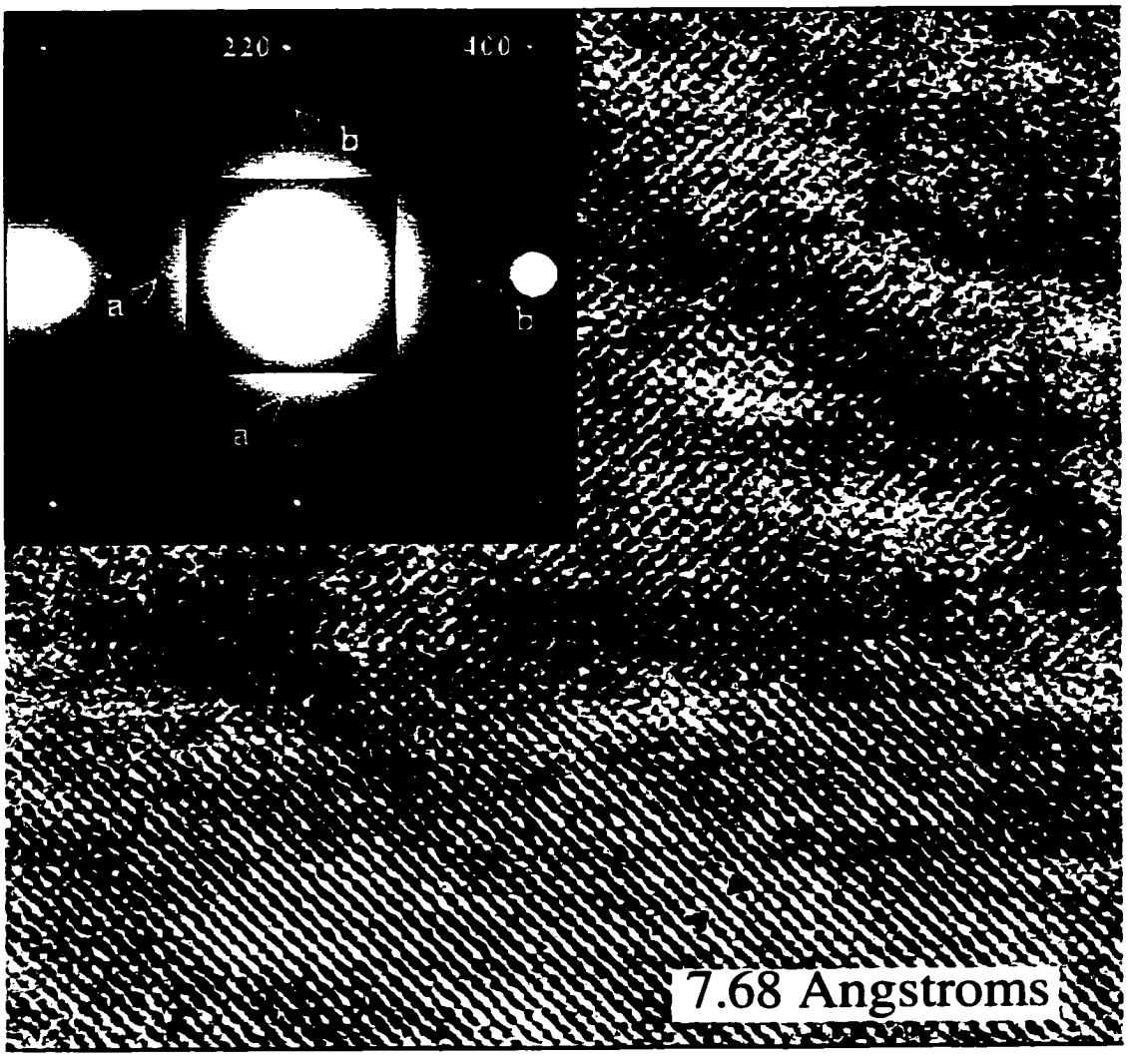

Figure 3.5. Off-zone HREM image of Si(001)-(2x1) surface taken at 200 kV. The 7.68 Å spacing is two times the 1x1 surface unit mesh and corresponds to the spacing between the Si dimer rows. Inset: the diffraction pattern with arrows for (a) (1x1) spots, and (b) (2x1) surface spots.

It was determined that the electron beam annealing produced a disordered surface on the side of the sample on which the electron beam was incident, and well-ordered steps on the exit surface (Section 3.1). Consequently, all Au depositions were performed only on the ordered surface.

The Au films were deposited at room temperature using SPEAR's metal evaporation stage. The Mo boat was carefully outgassed prior to the deposition. The Au coverage was estimated using the relative Si 2p and Au 4f XPS peak intensities averaged over an 800 μm diameter area. Since relatively low Au coverages were investigated, one monolayer was defined as the number of Au atoms equal to the surface atomic density of the substrate (6.8×10^{14} atoms/cm^2) corresponding to 1.2 Å. After each deposition, XPS and AES spectra were collected, and TED and HREM images were recorded at 300 kV.

3.2.2 Results

XPS spectra were acquired for different Au coverages. The binding energies of Au $4f_{7/2}$ and Si 2p as a function of Au coverage are shown in Figure 3.6. Both spectra show shifts from regular bulk values. The binding energy of Au $4f_{7/2}$ increases suddenly at the beginning of the Au deposition (up to around 2 Å) and decreases later to saturate at the value of the binding energy of pure gold. The binding energy change of Si 2p is in the opposite direction to that of Au $4f_{7/2}$. First it shifts to lower values, followed by a slow increase to the bulk Si binding energy for higher Au coverages.

The observed XPS spectra are similar in their trend to two other studies, except for the onset of the shifts. Braicovich et al. (1979) reported unchanged binding energies

for both Au and Si peaks up to 3ML of Au coverage, while a study by Iwami et al. (1988) shows spectra with Au 4f and Si 2p peaking at around 1ML Au coverage.

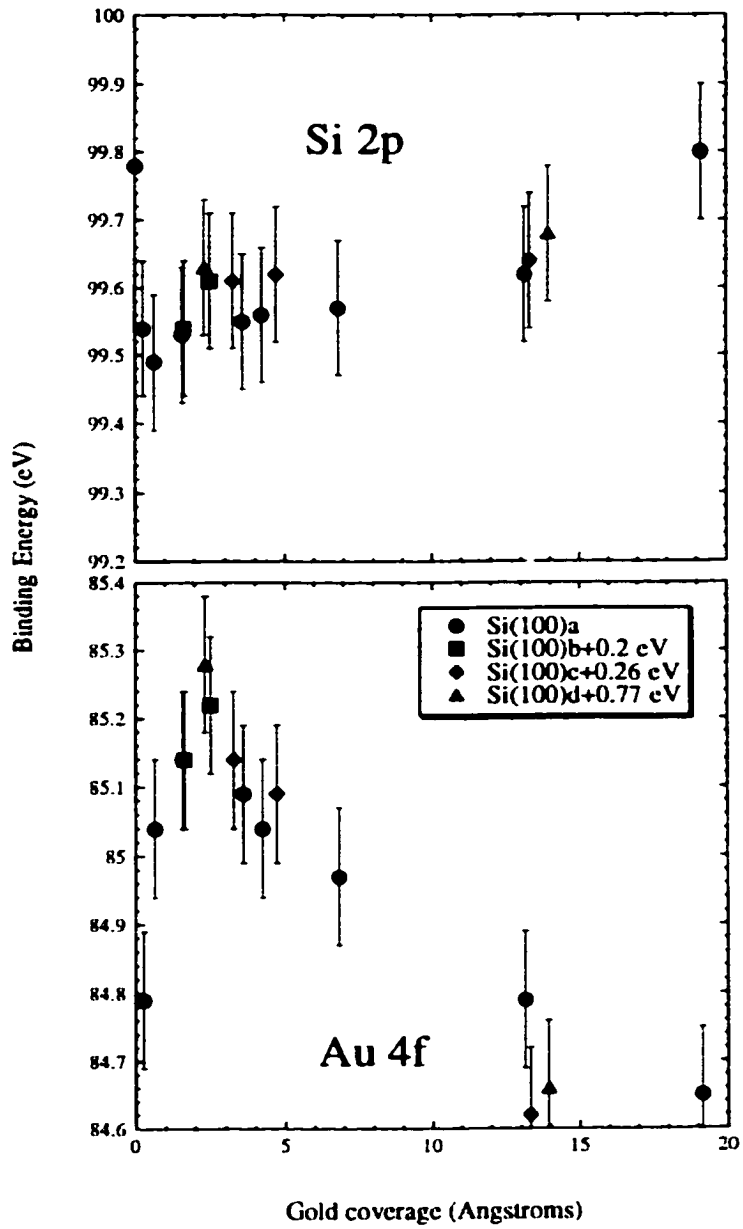

Figure 3.6. Shifts in the Si 2p and Au $4f_{7/2}$ peaks as a function of Au coverage. Si(001) a-d are four different samples studied, including the relative calibration offset. These offset values were measured using XPS by scanning over the Si 2p peak for each sample prior to Au deposition, and then adjusting relative to the Si 2p bulk value.

Both those groups associated the binding energy shifts to a Au-Si alloy formation or an intermixing reaction. However, the results are also consistent with a different interpretation. Oberli et al. (1981), and Rao et al. (1993) reported a shift to a higher binding energy of the Au $4f_{7/2}$ peak in the XPS spectra of small Au particles deposited on various substrates. They observed a decrease in the shift with the increase in size of the clusters.

In addition to XPS spectra, AES data were collected as shown in Figure 3.7. Two distinguishing features could be observed: the controversial peak splitting of the Si LVV at 13 Å of Au coverage, and a decrease of the Auger electron kinetic energy for Au NVV peak at lower coverages. The second feature is in agreement with the study of small Au particles by Oberli et al. (1981), who reported the shift of the Au peak to lower values when the size of the Au clusters decreases, and it correlates with Au clustering in the film. The first experimental characteristic is apparently in accord with the other view of the interface, the Au-Si room temperature chemical reaction. The Si 2p splitting was usually associated with a silicide formation (Narusawa, Komiya, and Hiraki 1973) based on Si spectra of vapor-quenched thin films of metastable Si-noble metal alloys.

Therefore, the results of these electron spectroscopic data were open to two different and possibly opposed views of the nature of the interface. They provide electronic but not atomic information such as structural changes of the Si substrate or displacements of Si atoms at the Si/Au interface due to possible reactions.

TEM micrographs, HREM images, and off-zone diffraction patterns were recorded for different Au coverages. Figure 3.8 shows the presence of multiply twinned

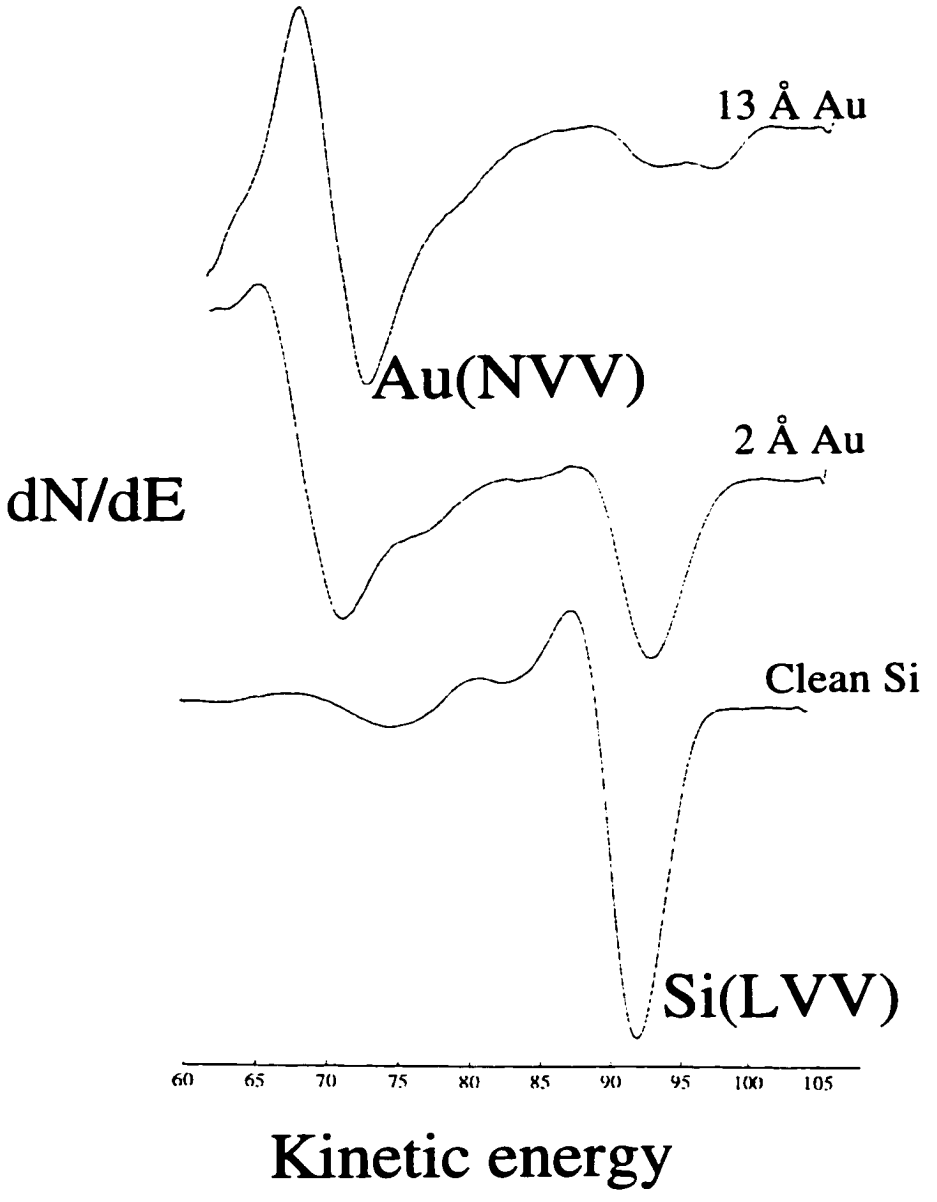

Figure 3.7. Line shape of the Si LVV and Au NVV Auger transitions as a function of Au coverage. Each spectrum has an uncertainty of σ=0.8 eV.

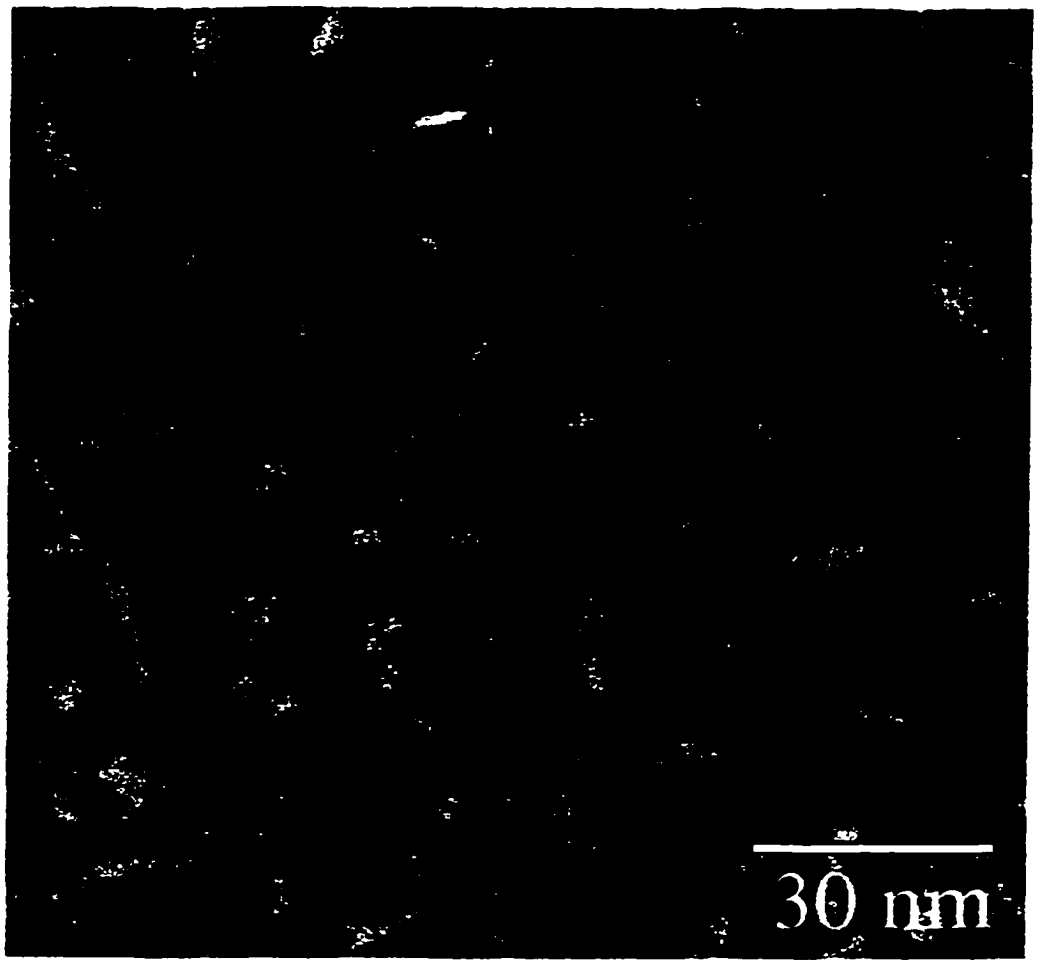

Figure 3.8. HREM image of the Si(001) surface following 13 Å of Au deposition.

and single-crystal small Au particles growing on the surface, at 13 Å of Au coverage. The same growth mode was reported by Doraiswamy, Jayaram, and Marks (1995) for Ag thin films deposited at room temperature on a Si(001)-(2x1) surface. The diffraction pattern for this Au layer thickness, Figure 3.9, displays rings coincident with the Au(111) and Au(200) spacings. The rings' shape indicates the presence of small-domain polycrystalline Au. The bright spots along the rings point to a Au(110)//Si(001) epitaxy on the two domains, 1x2 and 2x1, of the Si(001)-(2x1) reconstruction. In no micrograph we were able to observe any unidentifiable features not belonging to Au or Si to support the formation of a structured gold silicide at the interface.

Another interesting result, in disagreement with previous LEED studies of the Au/Si interface which reported a gradual fading of the Si (2x1) surface spots into a highly diffuse background during the Au deposition, is the presence of surface spots in the diffraction pattern even for a Au layer of 13 Å thick. Moreover, for a deposit of 8 Å, the spots indicating the preservation of a (2x1) periodicity at the interface were still apparent after a week of sample storage in SPEAR. The specimen was also analyzed using XPS and its spectrum showed chemisorbed oxygen on both sides and no Au on the undeposited side. Therefore, we can rule out the conservation of the Si native reconstruction on that side due to the destructive effect of water vapor on the Si(001)-(2x1) reconstruction (Boland 1990). The preservation of the native superstructure is not unique; a similar report of a (7x7) periodicity at the buried interface of Si(111)/Pb was published by Edwards et al. (1996).

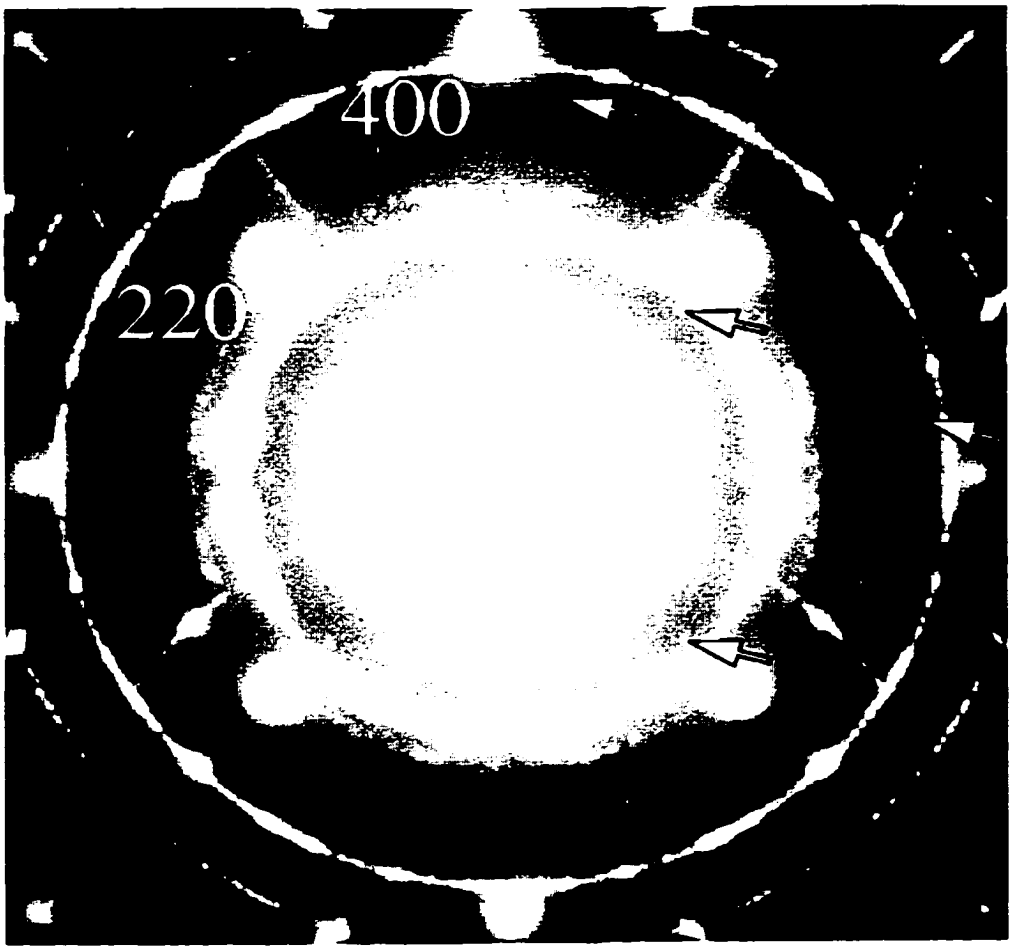

Figure 3.9. TED pattern of the Si(001) surface following 13 Å of Au deposition. The Si(001)-(2x1) surface superstructure spots have been arrowed for reference.

3.2.3 Discussion of Results

The structural information provided by TEM images suggests a different growth mode than the one previously assumed (Okuno et al. 1980; Narusawa et al. 1981; Dallaporta and Cros 1986). The HREM images and diffraction patterns clearly reveal a Stransky-Krastanov growth mode, layer plus island, and not a layer-by-layer mode (Frank van der Merwe). Aside from single-crystal structure, the off-zone HREM images display multiply twinned particles with different epitaxies relative to the substrate. Thus, the interface for the Au/Si(001) system is similar to that of the Ag/Si(001) system (Doraiswamy, Jayaram, and Marks 1995). For that system, previous reports presumed a simple single-crystal structure (Hanbücken and Le Lay 1986; Kimura and Takayanagi 1992).

The layer-by-layer growth that most of the studies assumed in their spectroscopic data analyses biased their structural interpretation . The shifts in the binding energy of Si 2p and Au 4f peaks were taken as a sign of the occurrence of a chemical reaction, even at room temperature, whereas they can be also induced by the surface growth morphology.

Vijayakrishnan and Rao (1991) and Rao et al. (1993) investigated the relationships between different metals' (including Au) binding energies and the size of the metal clusters in the nanometric range, on various semimetallic and insulating substrates. The cluster size was estimated by direct measurement with HREM and STM. They reported that the shift in Au binding energy is evidently the effect of cluster size . An increase in the binding energy was observed as the cluster size decreases, similar to the case of Cu and Ni clusters.

The variation in the Au 4f energy is explained as a screening effect. The hole created by photoemission is not compensated for by the transfer of a screening electron from the substrate to the cluster within the time scale of the photoemission process. A lowering of the kinetic energy of the escaping electron results, due to the Coulomb interaction between the remaining hole and the escaping photoelectron. Thus, a shift in the binding energy occurs. In addition to this effect, they also found that the nature of the substrate influences the shifts in the binding energy, a larger shift being induced by insulating substrates.

The explanation of the AES spectra was based on observations of Si peak splitting for vapor-quenched films of Si-Au (Narusawa, Komiya, and Hiraki 1973; Hiraki and Iwami 1974; Nakashima, Iwami, and Hiraki 1975). It was used as the proof of silicide formation in all subsequent studies of Au/Si interface. A neglected aspect of the original reports was that they observed the same double-peaked Si LVV spectra for vapor-quenched films of Si-Ag and Si-Cu. However, for the Si-Ag interface there is a general consensus that it is abrupt with no Ag silicide or alloy forming during Ag deposition.

From the HREM and TED images, the silicon atoms at the surface appear to sit in two different environments, leading to the peak splitting of the Si LVV transition observed in AES spectra. The two different cases arise due to the presence of small particles on the Si substrate. Some of the Si atoms are under the Au clusters while the others are beneath the amorphous or disordered layer that exists between the particles. Hence, there are two possible distinct contributions to the Si LVV line. The TEM data set allowed for a more accurate interpretation of the Au/Si spectroscopic data. It showed

that there is no silicide present in a quantity large enough to explain the recorded shifts in the XPS spectra and the Si peak splitting noticed in the AES spectra.

The properties of noble metal (Au, Ag)-covered Si surfaces have been one of the most intensively investigated systems with the use of a variety of surface science techniques. Previous studies of the initial stages of the Au film formation have yielded inconsistent conclusions of either an intermixed interface or a sharp one. Only by combining structural TEM information with spectroscopic data was a better picture of this controversial interface obtained.

CHAPTER 4:

STRUCTURE DETERMINATION OF Si(111)-(6x6)Au SURFACE

The gold on Si (111) surface in the 0-2 monolayers (ML) coverage range has been extensively studied, but many of the details are still unclear and the underlying physics uncertain. Below one monolayer, two distinct phases, the Si(111)-(5x2)Au, or (5x2) (Marks and Plass 1995, and references cited therein), and Si(111)-($\sqrt{3}$x$\sqrt{3}$)R30°Au, or ($\sqrt{3}$x$\sqrt{3}$) (Plass and Marks 1995, and references cited therein), structures are known to exist. Both of these are stable to temperatures far in excess of the unusually low bulk eutectic melting point of 363°C of the Au/Si system.

In this coverage regime, a new approach has provided a better understanding of surface structures. Plass and Marks (1997) proposed a phase diagram for the submonolayer Au on Si(111) system, which obeys Gibbs phase rules and with phase boundaries based on thermodynamics principles. This approach for surfaces is replacing the more familiar phase maps, which show the temperature versus coverage regime for

surface phases. Extending the surface phase diagram to higher Au coverages requires knowledge of the atomic structure of the surface phases present above 1 ML of Au.

4.1 Background

In the 1.0-1.5 ML range (and perhaps with slightly lower coverages), diffraction experiments show strong ($\sqrt{3}$x$\sqrt{3}$) intensities and additional diffuse or ordered structures (Higashiyama, Kono, and Sagawa 1986; Dornisch et al. 1991; Takahashi, Tanashiro, and Takayanagy 1991; Yuhara, Inoue, and Morita 1992a, 1992b; Takami et al. 1994; Khramtsova and Ichimiya 1997). Star-like spots and sharp spots surrounded by ring-like structures (simple diffuse rings, rings with a double-spot hexagon pattern, or incomplete rings) have been observed. The most well-defined of these structures is the Si(111)-(6x6)Au, or (6x6), surface phase occurring at around 1.4 ML of coverage, which forms very close to the bulk eutectic temperature. However, other studies (Huang and Williams 1988; Nogami, Baski, and Quate 1990) have reported the formation of the (6x6) structure at 1.0 ML, thus the exact Au coverage is still controversial. At higher coverages, gold particles form, suggesting a Stranski-Krastanov growth mode (LeLay et al. 1976; Higashiyama, Kono, and Sagawa 1986), although Święch, Bauer, and Mundschau (1991) reported the formation of 3D Au particles as preceding and continuing in parallel with the 6x6 structure formation and growth.

It should be noted that quenching the bulk eutectic is known to produce a glass (Klement, Willens, and Duwez 1960) which appears to crystallize at similar temperatures into a number of poorly determined phases (Okamoto and Massalski 1983; Baumann and

Schroter 1991; Robison, Sharma, and Eyring 1991). In addition, there is some evidence from XPS (Hiraki and Iwami 1974), LEED (Green and Bauer 1976), and RHEED (Ichimiya et al. 1995) data for a gold-silicide. Understanding the Au (6x6) structure can shed light on the transition from a 2-D surface to a more bulk-like behavior. Furthermore, because the temperatures are very close to the bulk eutectic and glass formation/crystallization temperatures, unusual phenomena may be present. For instance, in this temperature and coverage range, strong homoepitaxial growth of silicon has been observed (Wilk et al. 1994).

The Au (6x6) phase was first reported by Lander (1964) and subsequently studied by almost all surface-sensitive methods: LEED (Lander 1964; Higashiyama, Kono, and Sagawa 1986; Huang and Williams 1988; Yuhara, Inoue, and Morita 1992b), TED (Takahashi, Tanashiro, and Takayanagy 1991), AES (Salvan et al. 1985; Yuhara, Inoue, and Morita 1992b), Rutherford backscattering spectroscopy (RBS) (Yuhara, Inoue, and Morita 1992b), x-ray diffraction (XRD) (Dornisch et al. 1991), impact-collision ion-scattering spectroscopy (ICISS) (Huang and Williams 1988), and STM (Salvan et al. 1985; Nogami, Baski, and Quate 1990; Takami et al. 1994).

Several results indicated that the (6x6) structure is closely connected to the Au ($\sqrt{3}$x$\sqrt{3}$) structure, and can be considered as a low-temperature precursor phase for the unknown surface which displays a ($\sqrt{3}$x$\sqrt{3}$) + ring-like diffraction pattern. Higashiyama, Kono, and Sagawa (1986) found the phase transition between these two structures to be reversible. The Au (6x6) diffraction pattern transformed into the ($\sqrt{3}$x$\sqrt{3}$) + ring-like structure by annealing at high temperature, and transformed back into the (6x6) structure

by annealing at low temperatures. Based on a kinematical analysis of LEED spot profiles, the same study suggested that the unusual ($\sqrt{3}$x$\sqrt{3}$) patterns are due to the early stages of the (6x6) phase formation. Using, in addition, the STM observations by Salvan et al. (1985), which showed the (6x6) surface displaying structural units in which four maxima are arranged with ($\sqrt{3}$x$\sqrt{3}$) periodicity, Higashiyama, Kono, and Sagawa (1986) explained the reversible transition between the two phases as a gradual ordering/disordering of the structural units. On the other hand, other studies (Nogami, Baski, and Quate 1990; Takahashi, Tanashiro, and Takayanagi 1991) found an irreversible transition, with the (6x6) diffraction pattern forming only by additional gold deposition onto the ($\sqrt{3}$x$\sqrt{3}$) + ring-like structure during heating in the low temperature regime.

Okuda, Daimon et al. (1997) reported a strong spectral resemblance between ($\sqrt{3}$x$\sqrt{3}$) + ring-like and (6x6) surfaces, based on angle resolved photoelectron spectroscopy (ARPES) and Si 2p surface core level shifts (SCLS) results. They inferred that the local structures of these two phases are almost the same, with the ordering of domain walls leading the transition to the (6x6) Au surface from the other structure.

From ICISS experimental data, Huang and Williams (1988) proposed a (6x6) honeycomb structure composed of a centered hexagonal array with 25 % empty hexagons. Thus, the structure is consistent with the honeycomb model for ($\sqrt{3}$x$\sqrt{3}$), which they considered to be a precursor and an incomplete (6x6) phase with centered and empty hexagons lacking long-range order. An STM study (Nogami, Baski, and Quate 1990) of the (6x6) structure, formed at a gold coverage slightly above 1 ML, shows sets

of three maxima surrounded by triangular domain walls and a number of bright "protrusions". In this model the (6x6) structure is described as a periodic arrangement of small ($\sqrt{3}$x$\sqrt{3}$) domains. At a higher coverage (1.4 ML), another STM study (Takami et al. 1994) suggested a slightly different structure, a rectangular array of protrusions with a smaller periodicity than the (6x6) unit cell.

A previous attempt to look at this surface using x-ray diffraction data and a Patterson approach by Dornisch et al. (1991) was at best only partially successful. However, the Patterson map clearly showed that Au trimers are an essential part of the structure. This x-ray study concluded that the (6x6) phase is not an ordered superstructure of the ($\sqrt{3}$x$\sqrt{3}$) phase and that the main feature of their model was Au trimer triplets.

4.2 Experimental

The x-ray data set used for this study was received from Dr. R. Feidenhans'l in the form of symmetry-averaged intensities with estimated measurement errors.

The Si(111) surface was cleaned by annealing at 900°C and slowly cooling to produce a sharp (7x7) LEED pattern. Gold was deposited from an effusion cell held at 1180°C onto the Si surface at a rate of 0.3 ML/min. The sample was then transferred under UHV conditions to a small portable UHV x-ray cell, mounted on a diffractometer. The pressure in the cell was in the 10^{-10} mbar region and no decay of intensities of the samples was observed over the measurement period (one day).

The x-ray diffraction experiments were performed on the vertical scattering diffractometer at the wiggler beamline W1 at the Hamburger Synchrotron Radiation Laboratory. The samples were aligned on their optical surface by total reflection, such that the angle of incidence of the x-rays to the surface could be kept fixed during data collection. In order to maximize the diffracted intensity and minimize the background, the angle of incidence was set to the critical angle for total external reflection. The exit angle was near the critical angle, so the momentum transfer in the direction normal to the surface was close to zero. Reproducibility between symmetry-equivalent reflections was checked for six reflections, giving about 10% systematic error. The final data set consisted of 139 independent intensities in the p6mm plane group and 248 in the p3 plane group.

4.3 Initial Model

The Direct Methods approach used for solving the Au (6x6) structure (Grozea et al. 1998; Marks, Grozea et al. 1998) involved a Minimum Relative Entropy method coupled with a genetic algorithm for global optimization. Ideally, with small or no experimental measurement errors, and a complete set of intensities, the maps of the calculated electron density using phases estimated through Direct Methods will be accurate restorations of the charge density. In practice, sometimes only part of the structure is identifiable in the initial analysis, the case herein since the true structure is p3 with twinning. However, even with a relatively small fragment of the structure known the remainder can be uniquely determined by one of many different methods.

Working from an initial fragment identifiable in the charge density maps, the full structure was determined by combining iterative steps of refinement of the atomic positions and heavy-atom holography to determine new sites.

Shown in Figure 4.1a is an initial fragment with about 20 gold atoms, found among the top phasing solutions using p3 symmetry. Including the peak at the origin which turned out to be only partially occupied, the peaks are very close to gold positions in the final refinement, and three weaker silicon peaks are also observable. Other maps showed different fragments of the total structure. For reference, in p3 symmetry, incoherent twin domains were assumed, yielding p6mm Patterson symmetry. While not obvious in the initial stages of the analysis, all the top solutions in both p3 and p31m symmetry showed 20 or more of the gold atoms. Building from this structure we were able to generate the gold framework shown in Figure 4.1d, with a total of 14 independent sites (42 atoms without the partially occupied sites). Intermediate steps in constructing the model are shown in Figure 4.1b,c, with the corresponding diffraction patterns in Figure 4.2a-d. Figure 4.3 shows missing sites suggested by heavy-atom holography applied to the partial model from Figure 4.1c; the three most intense symmetry-equivalent spots were chosen as the next step (one of them is arrowed in the figure).

4.4 Structure Refinement

As the final step, the atomic positions determined from heavy-atom holography analysis were refined using a conventional χ^2 minimization. In terms of an R-factor and a reduced χ^2, the structure gave R=0.25 and χ^2=50. While the χ^2 value is rather high, it is

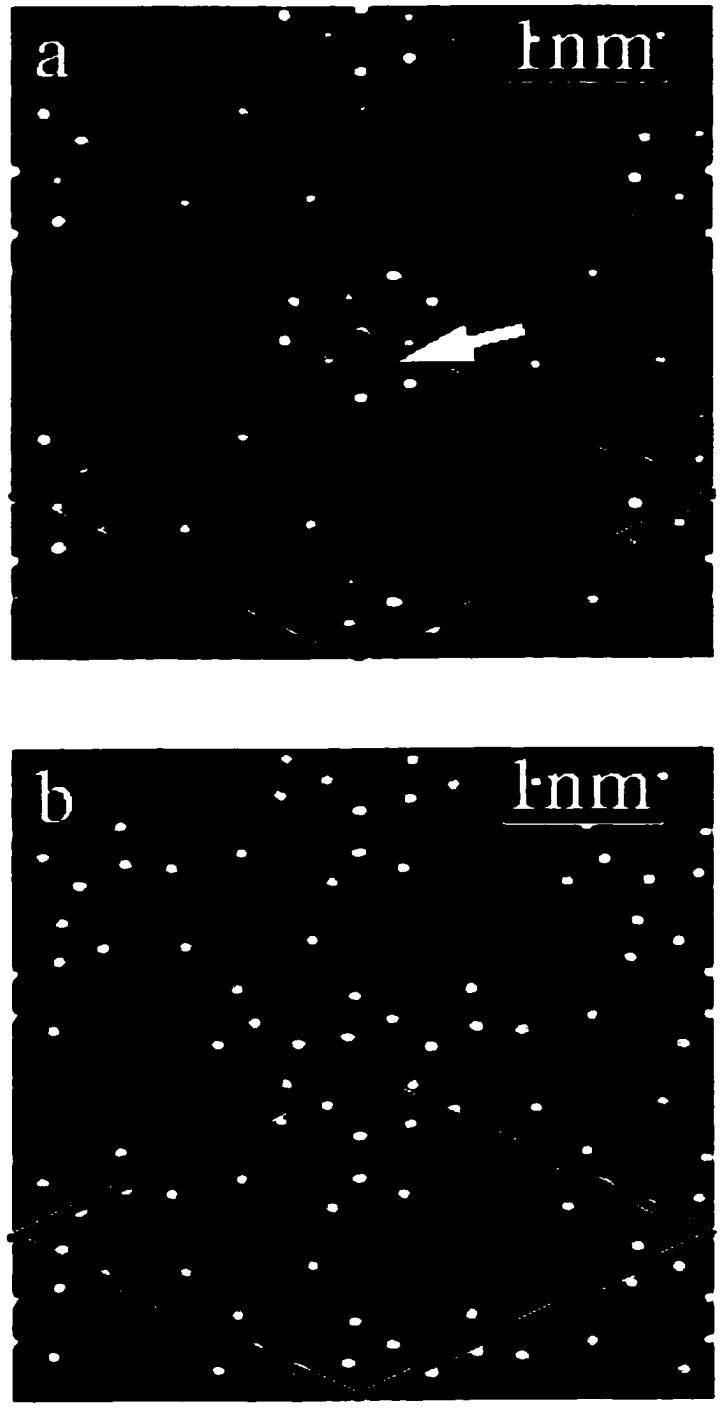

Figure 4.1. a) Charge density map of the initial fragment used, with the primitive unit cell indicated by solid lines (unit cell length 6a, a=3.83 Å). A weaker Si site (one of the three symmetry-equivalent) is arrowed, and all other peaks correspond to Au sites; b), c) Intermediate steps in constructing the model; d) Final model with 42 gold atoms.

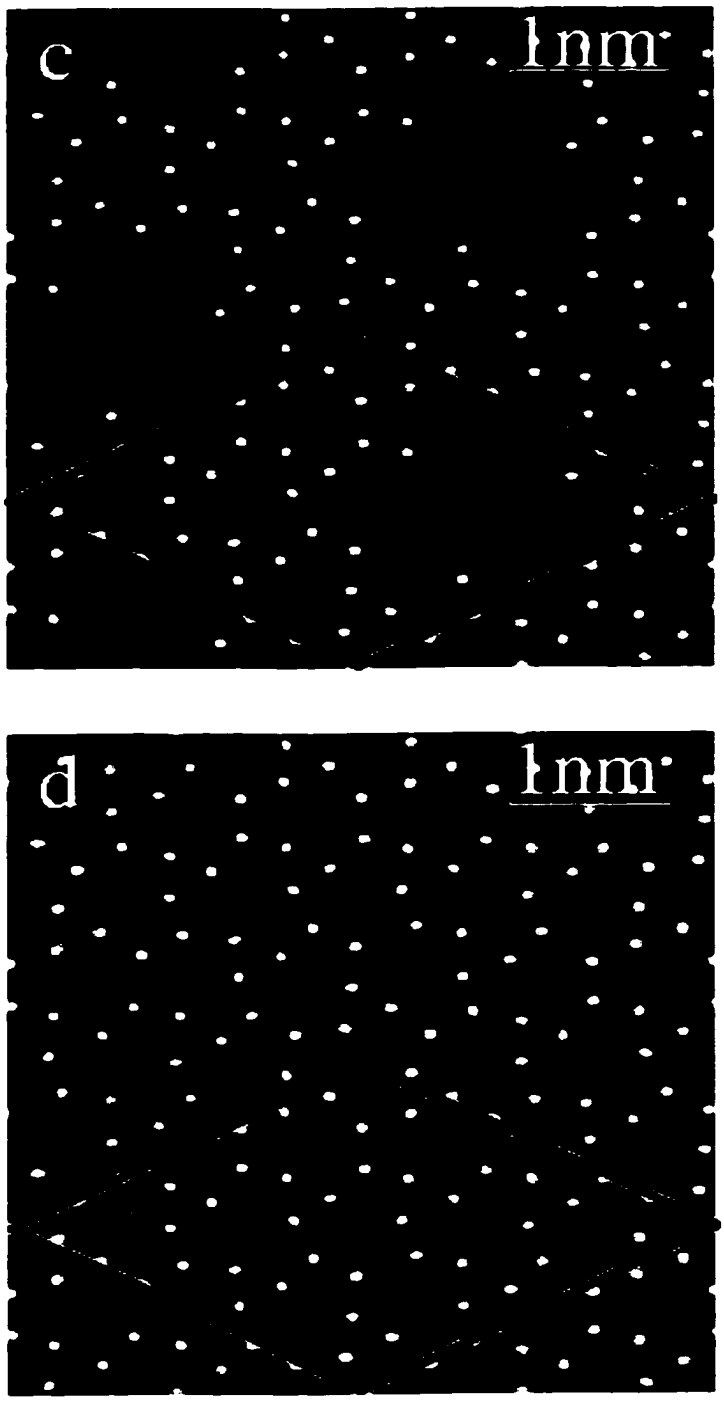

Figure 4.1. Continued.

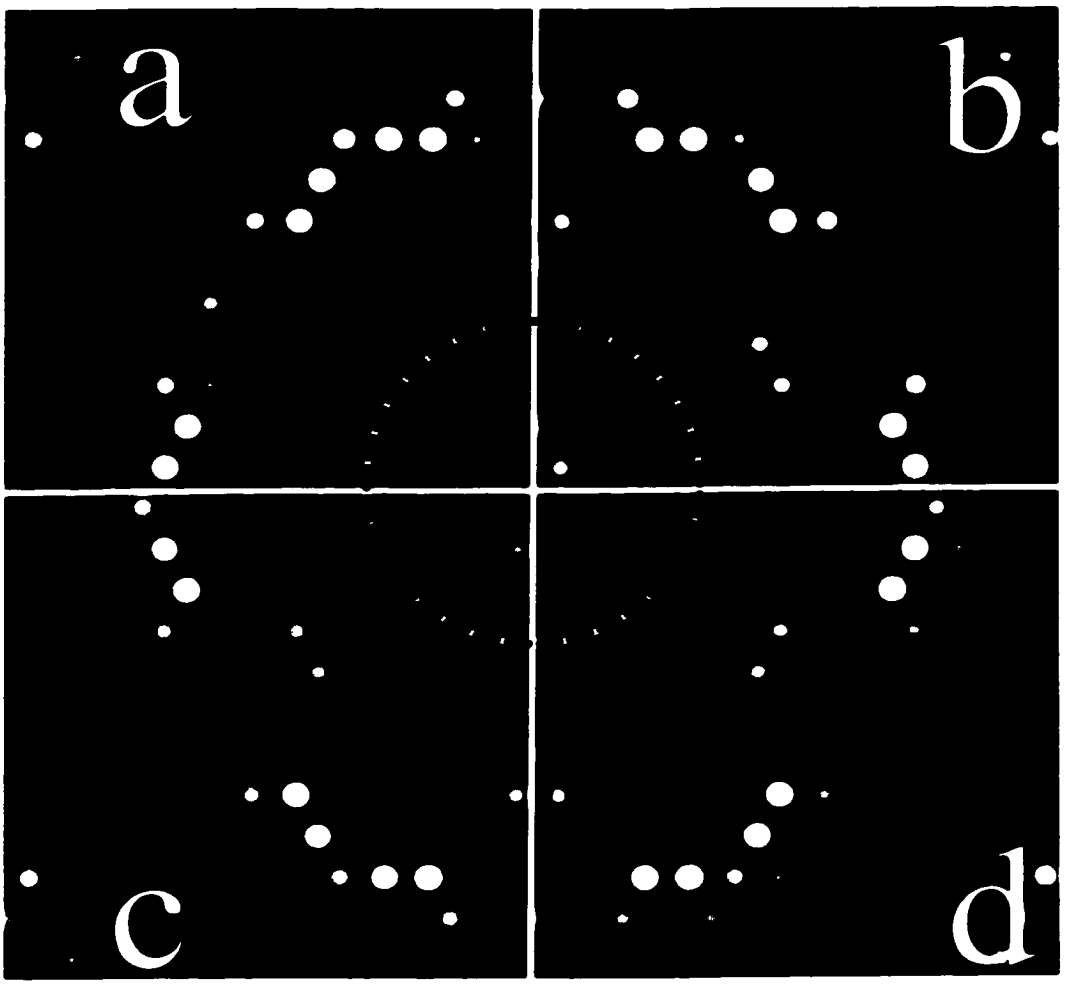

Figure 4.2. a)-d) Corresponding diffraction patterns for Figure 4.1a-d. The dashed circle is added to highlight a region where some beam intensities vary at different stages of model completion.

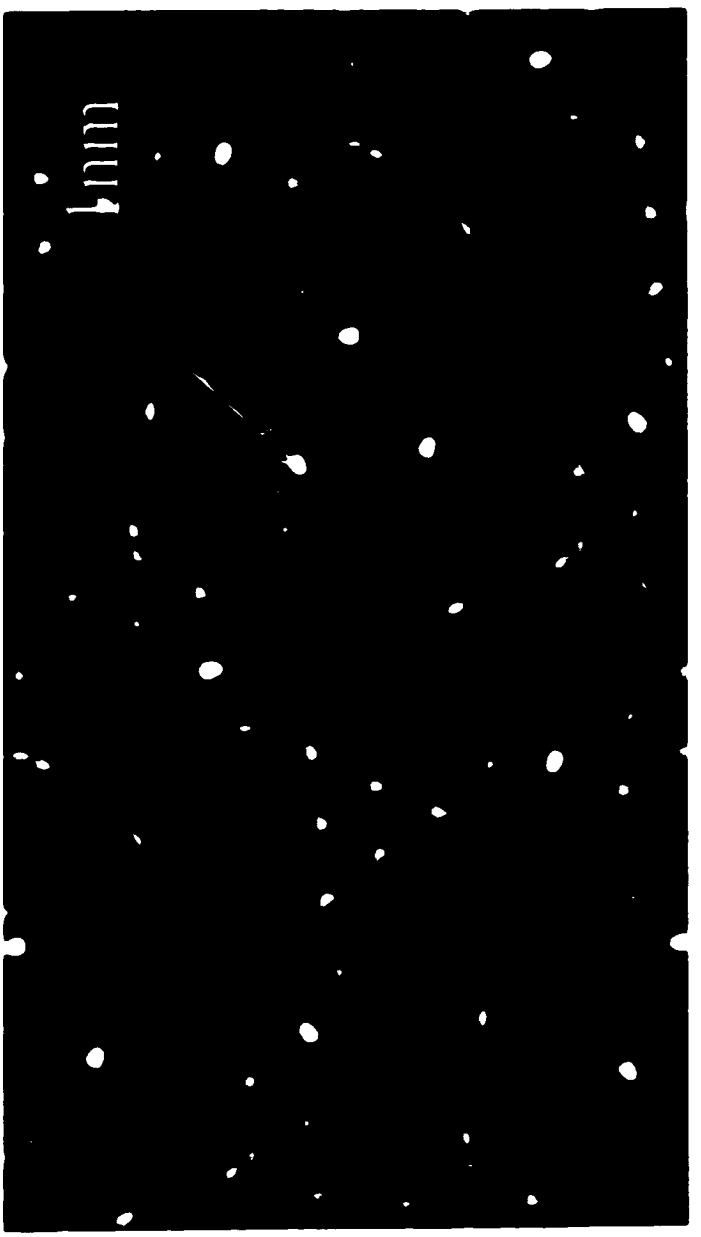

Figure 4.3. New possible atom sites generated by heavy-atom holography after processing the partial model from Figure 4.1c. The most intense sites were chosen as the next step (one of the three symmetry equivalent is arrowed).

more than two orders of magnitude better than that found in a previous analysis (Dornisch et al. 1991). A strong possibility exists that the experimental results were obtained from a two-phase ($\sqrt{3}$x$\sqrt{3}$) and (6x6) mixture (both phases have the same plane group symmetry); eliminating reflections which overlap with the ($\sqrt{3}$x$\sqrt{3}$) reduced χ^2 to 32 and R to 0.2. (This reduced the number of reflections in p3 plane group from 248 to 234.) Adding a double silicon layer reduced χ^2 and R again by about a factor of two; similarly, a second double silicon layer reduced χ^2 to about 8.

Based upon previous work (Plass and Marks 1995) with the ($\sqrt{3}$x$\sqrt{3}$) structure, the relaxation is assumed to extend several layers into the substrate. However, in p3 symmetry there are only 234 reflections (about half of these independent), so including large numbers of silicon atoms (12 per layer) is not justifiable in terms of the number of measurements. To compensate for not including independent variables for all subsurface atom positions, a subsurface strain field expanded as the gradient of a two-dimensionally periodic harmonic (Love 1944; Jayaram, Xu, and Marks 1993) was used to model displacements into the substrate. The strain field is constrained to decay exponentially into the bulk. For the final stages of the minimization, the more robust form χ was utilized, which is less sensitive to outliers (points with large errors) in the data (Press et al. 1986). For one double layer of silicon we obtained χ=2.7; for two, χ=2.0. Including partial occupancy at the three special sites ((0,0), (1/3,2/3), and (2/3,1/3)) and the subsurface strain field had a large effect, yielding χ^2=3.8 and χ=1.7, with a partial occupancy of approximately 0.5 (total coverage of 1.2 ML).

Atom positions for two silicon double layers and some of the calculated and experimental intensity values are shown in Tables 4.1 and 4.2 respectively, and the final model including Au and Si atoms is shown in Figure 4.4. For the atom positions, we averaged four calculations, two each using χ^2 and χ, with two different registries for the third double layer of silicon atoms, and then used these to determine the errors. The gold site errors are about 0.01 Å, the silicon about 0.05 Å. However, since the gold Debye-Waller factor refined to a rather high value (0.16 Å R.M.S. displacement), implying substantial static disorder consistent with partial occupancy, a multiplicative factor of 2-3 on the errors might be appropriate. Most of this is almost certainly rotation of the gold trimers, similar to the ($\sqrt{3}$x$\sqrt{3}$) (Plass and Marks 1995). We were not able to refine the surface silicon Debye-Waller term, which tended to drop to unreasonable values, implying more subsurface relaxations than can reasonably be matched with the available data.

4.5 Discussion of Results

The most interesting aspect of the (6x6) structure is that it is astonishingly simple, and at the same time complicated. There is a strong relationship to the parent ($\sqrt{3}$x$\sqrt{3}$) with three sets of three gold trimers. More interesting is the placement of the additional gold atoms which form incomplete pentagons and trimer units; if all the special sites were occupied, complete pentagons would be formed. Every gold-gold separation is close to 0.28 nm, the bulk gold interatomic distance. At the center of these incomplete pentagons, probably at the lower apex of a pentagonal prism, are the silicon atoms of the next layer.

Table 4.1. Average atomic positions with 14 gold sites and two Si double layers (24 sites). Only two-dimensional diffraction data were available, so no heights could be refined. Values for the errors (δX,δY) as well as the displacements from bulk sites for the subsurface silicon atoms (ΔX,ΔY) are given. Gold Debye-Waller factor (B)=1.98 (0.02); occupancy of special (protrusion) sites = 0.504 (0.004)

Gold Sites:

X	δX	Y	δY
0.3435	(0.0012)	0.8670	(0.0005)
0.3090	(0.0005)	0.3018	(0.0002)
0.1852	(0.0006)	0.1804	(0.0011)
0.8647	(0.0004)	0.3488	(0.0003)
0.2545	(0.0005)	0.0315	(0.0008)
0.4470	(0.0007)	0.3553	(0.0005)
0.9560	(0.0003)	0.0926	(0.0007)
0.6276	(0.0003)	0.2048	(0.0005)
0.4712	(0.0004)	0.8840	(0.0005)
0.0089	(0.0006)	0.3582	(0.0001)
0.2501	(0.0003)	0.7164	(0.0015)
0.7832	(0.0003)	0.8687	(0.0002)
0.4523	(0.0008)	0.2356	(0.0007)
0.5880	(0.0004)	0.8725	(0.0003)

Silicon layer 1:

X	δX	ΔX(Å)	Y	δY	ΔY(Å)
0.0309	(0.0021)	-0.569	0.9320	(0.0026)	-0.286
0.4116	(0.0009)	0.524	0.6237	(0.0014)	0.291
0.7445	(0.0014)	0.512	0.3147	(0.0032)	0.850
0.3681	(0.0024)	-0.478	0.1072	(0.0006)	-0.090
0.3577	(0.0043)	-0.719	0.2350	(0.0021)	-0.985
0.2369	(0.0036)	0.338	0.1390	(0.0083)	0.643
0.1960	(0.0031)	-0.604	0.3002	(0.0042)	0.517
0.1738	(0.0024)	-1.115	0.3970	(0.0017)	-1.093
0.0908	(0.0008)	0.812	0.3398	(0.0021)	1.428
0.5261	(0.0010)	-0.679	0.4502	(0.0008)	0.133
0.5798	(0.0049)	0.558	0.5665	(0.0049)	-1.027
0.3955	(0.0010)	0.152	0.4152	(0.0015)	-0.674

Silicon layer 2:

X	δX	ΔX(Å)	Y	δY	ΔY(Å)
0.0582	(0.0002)	0.060	0.1099	(0.0007)	-0.028
0.2220	(0.0004)	-0.005	0.6090	(0.0001)	-0.049
0.7198	(0.0001)	-0.056	0.4453	(0.0012)	0.019
0.2249	(0.0006)	0.061	0.1144	(0.0002)	0.076
0.3882	(0.0007)	-0.015	0.1113	(0.0007)	0.004
0.3870	(0.0010)	-0.044	0.2756	(0.0006)	-0.050
0.0570	(0.0002)	0.033	0.2832	(0.0006)	0.125
0.2211	(0.0002)	-0.027	0.2794	(0.0007)	0.038
0.2189	(0.0001)	-0.077	0.4392	(0.0007)	-0.122
0.3926	(0.0007)	0.086	0.4408	(0.0008)	-0.083
0.5545	(0.0014)	-0.024	0.4469	(0.0015)	0.057
0.5591	(0.0010)	0.081	0.6086	(0.0010)	-0.057

Table 4.2 List of the intensities of the stronger reflections (using crystallographic notation, not fractional indices), the corresponding calculated values, the weighted error and absolute errors for χ^2=3.8.

H	K	Expt	Calculated	Wt Err	Abs Err
7	2	0.488E+02	0.489E+02	-0.330E-01	-0.134E-01
8	1	0.469E+02	0.449E+02	0.285E+01	0.200E+01
9	0	0.311E+02	0.304E+02	0.241E+01	0.767E+00
7	3	0.229E+02	0.228E+02	0.254E+00	0.866E-01
9	7	0.208E+02	0.205E+02	0.556E+00	0.279E+00
5	5	0.175E+02	0.173E+02	0.609E+00	0.190E+00
6	3	0.128E+02	0.131E+02	-0.132E+01	-0.344E+00
4	3	0.117E+02	0.120E+02	-0.183E+01	-0.296E+00
8	0	0.862E+01	0.896E+01	-0.132E+01	-0.345E+00
9	1	0.937E+01	0.964E+01	-0.995E+00	-0.263E+00
11	5	0.122E+02	0.124E+02	-0.608E+00	-0.179E+00
13	2	0.111E+02	0.111E+02	-0.580E-01	-0.174E-01
14	1	0.993E+01	0.119E+02	-0.303E+01	-0.195E+01
10	6	0.873E+01	0.883E+01	-0.462E+00	-0.993E-01
10	7	0.810E+01	0.768E+01	0.190E+01	0.421E+00
16	1	0.793E+01	0.817E+01	-0.595E+00	-0.238E+00
7	5	0.718E+01	0.610E+01	0.437E+01	0.108E+01
6	5	0.689E+01	0.454E+01	0.184E+01	0.235E+01
15	4	0.596E+01	0.642E+01	-0.118E+01	-0.460E+00
15	0	0.592E+01	0.622E+01	-0.922E+00	-0.298E+00
3	5	0.584E+01	0.598E+01	-0.599E+00	-0.143E+00

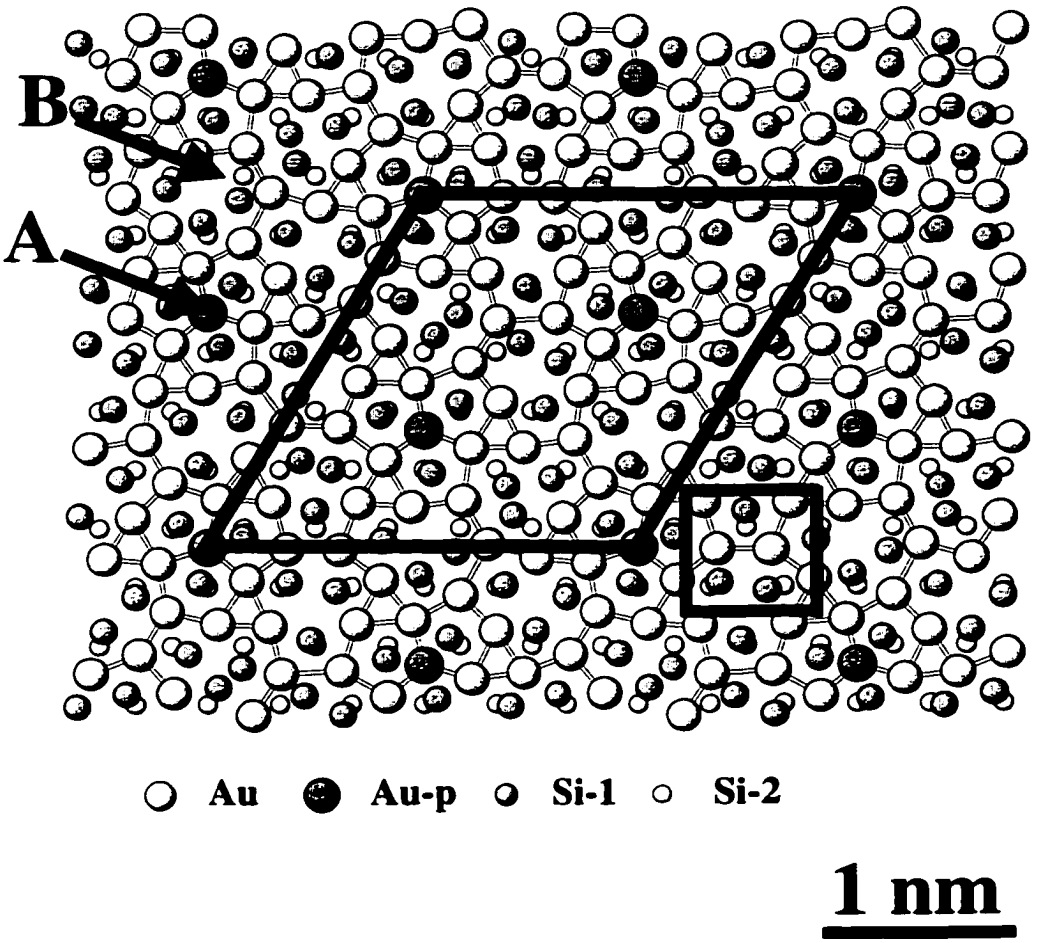

Figure 4.4. Diagram of the structure, with the primitive unit cell indicated by solid lines and the notation Au-p for the partially occupied sites. The second double layer silicon atoms are only slightly displaced from bulk sites — see Table 4.1. The structure can be described in terms of incomplete pentagons and trimer units, or the two gold ring configurations A and B discussed in the text. One of the rectangular units observed in domain boundaries of the ($\sqrt{3}$x$\sqrt{3}$) structure is shown.

In a number of cases silicon atoms are separated by about 0.2 nm, implying the presence of second-layer dimerization.

The correspondence at a qualitative level between this structure and the STM images (Nogami, Baski, and Quate 1990; Takami et al. 1994; Falta et al. 1995) at lower coverages is good. Similar to the parent ($\sqrt{3}x\sqrt{3}$) structure, the trimers are not properly resolved, and the protrusions are the partially occupied special sites -- these match the STM images not only in location within the unit cell but also in terms of their local symmetry. The overall symmetry of the structure is close to p31m, again matching the STM images well. The trimers are arranged in rectangular arrays (Figure 4.4) which have previously been observed in the domain walls of the ($\sqrt{3}x\sqrt{3}$) structure, where they become more abundant with increasing coverage (Takami et al. 1994) and the ($\sqrt{3}x\sqrt{3}$) LEED pattern becomes more diffuse. This suggests that the domain walls in the ($\sqrt{3}x\sqrt{3}$) break up with increasing coverage and reorganize as part of the (6x6) structure, which is in agreement with ARPES results (Okuda, Daimon et al. 1997).

This structure is remarkably similar to what would be expected for a two-dimensional glass with pentagonal units, trimers, and a fixed gold-gold separation. To understand this, note that the structure can be considered as a combination of the two Au ring structures A and B in Figure 4.4 surrounding three silicon atoms in the next layer, with two rotational variants of B. The center of A rings correspond to the partially occupied special sites, and for full occupancy, the Au coverage will vary from 1.2 ML to 1.25 ML. Furthermore, filling the center of all B rings will increase the Au coverage to 1.5 ML, thus correlating with the experimental observations of the 6x6 structure's

presence for coverages from around 1.0 ML up to 1.5 ML (Higashiyama, Kono, and Sagawa 1986; Yuhara, Inoue, and Morita 1992b, Takami et al. 1994). Both rings sit at ($\sqrt{3}$x$\sqrt{3}$) lattice sites, the particular configuration shown giving the (6x6) structure with triangular domain walls consisting of arrays of B rings surrounding A units (Figure 4.5). A similar array of triangular domain walls was recently proposed by Nagao et al. (1998) together with a description of the ($\sqrt{3}$x$\sqrt{3}$) structure at high Au coverage as an 'amorphous-like' (glass-like) structure in the arrangement of domain walls, as opposed to a 'crystalline' arrangement for the case of (6x6) phase.

Pure A units with vacancies give the known ($\sqrt{3}$x$\sqrt{3}$) structure. Other tilings yield a combination of trimers and incomplete pentagon units breaking the long-range order to produce a glass-like structure. However, this would not be a true glass because relatively sharp diffraction spots would be obtained at the ($\sqrt{3}$x$\sqrt{3}$) unit cell reciprocal lattice points, with diffuse scattering elsewhere in agreement with experimental data, as shown in Figure 4.6. A glass-like tiling using A and B gold units sitting at ($\sqrt{3}$x$\sqrt{3}$) lattice sites and its corresponding diffraction pattern are shown in Figure 4.7. We hypothesize that the whole 0.8-1.5 ML coverage range is really a surface solution pseudo-glass. As such, it is a two-dimensional analogue of the bulk glassy state, which may well have similar structural units.

Many questions about the (6x6) structure remain open. It would obviously be useful to obtain more precise information about the silicon sites, which would require collection of a larger data set using either x-ray or transmission electron diffraction. Electron diffraction will be more sensitive to the silicon sites, e.g. in the case of the

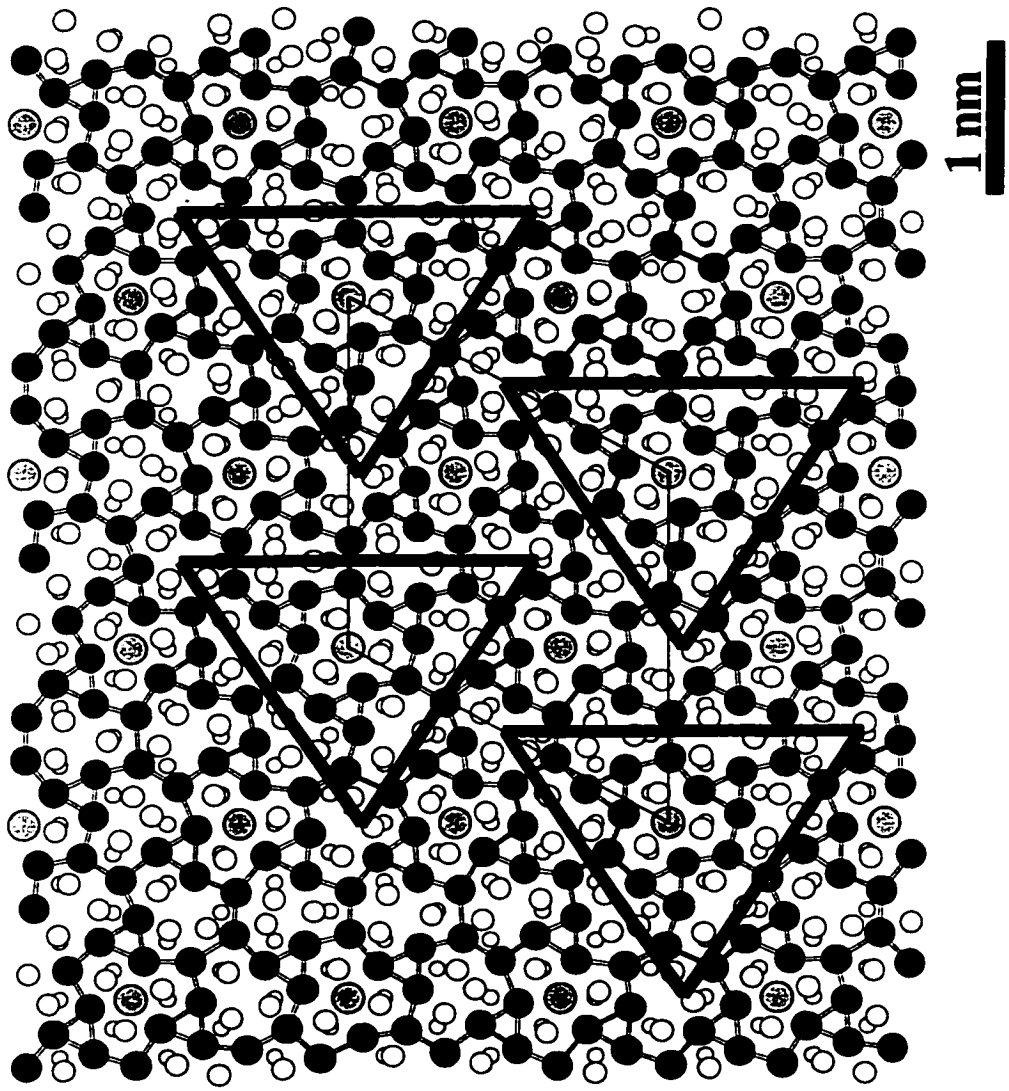

Figure 4.5. Triangular domain walls of Si(111)-(6x6)Au, indicated by solid lines.

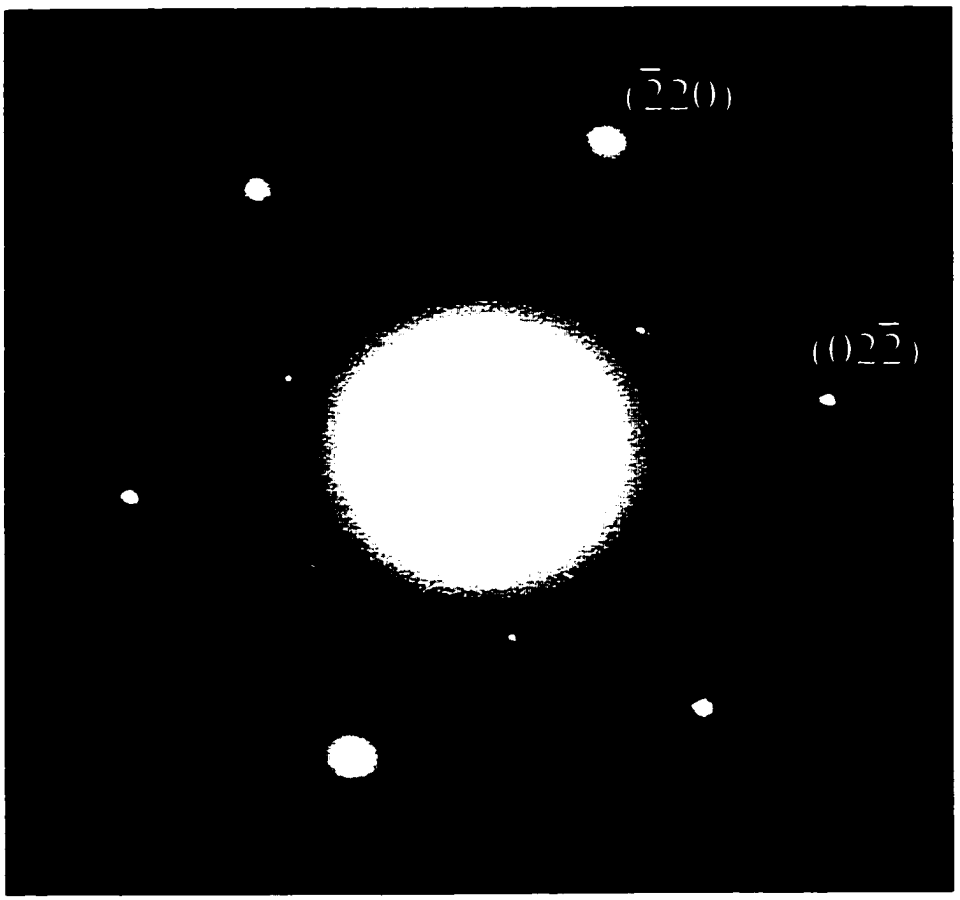

Figure 4.6. Experimental diffraction pattern of ($\sqrt{3}$x$\sqrt{3}$) + ring-like structure.

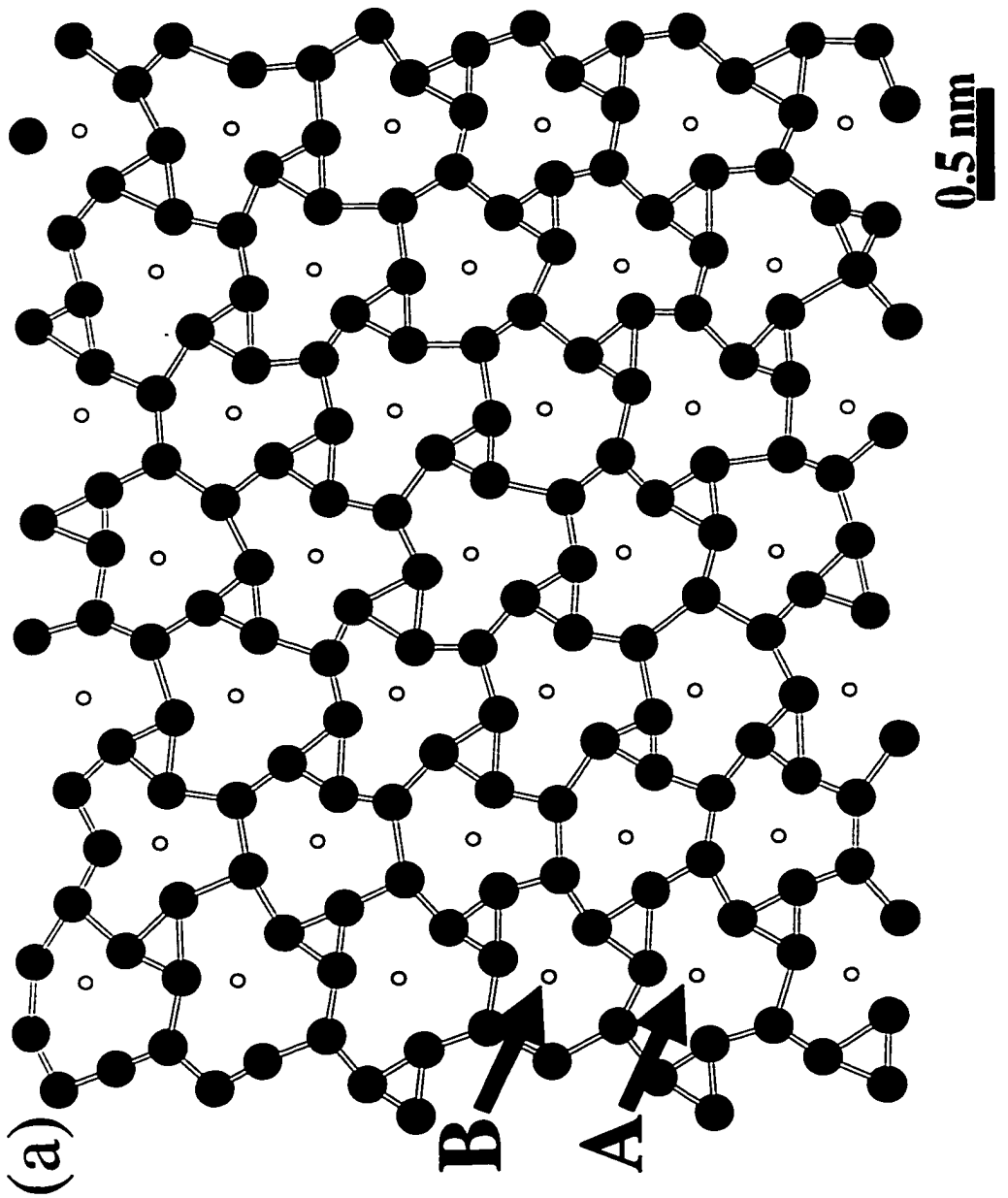

Figure 4.7. a) Glass-like tiling using A and B gold units (Au atoms are large dark circles, and the small empty circles mark the ($\sqrt{3}$x$\sqrt{3}$) lattice); b) Corresponding diffraction pattern showing sharp diffraction spots at the ($\sqrt{3}$x$\sqrt{3}$) unit cell reciprocal lattice points and diffuse scattering elsewhere. A (3x$\sqrt{3}$) unit cell is marked.

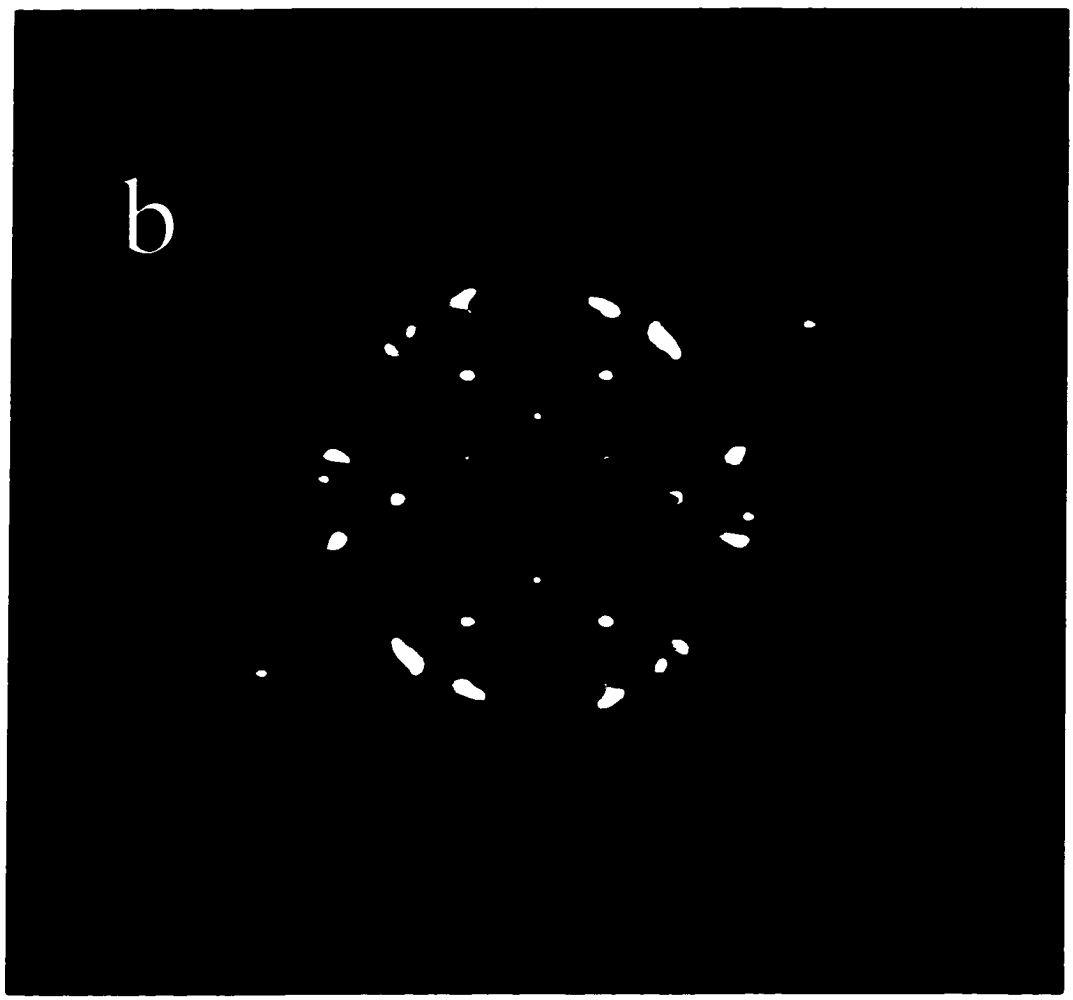

Figure 4.7. a) Glass-like tiling using A and B gold units (Au atoms are large dark circles, and the small empty circles mark the ($\sqrt{3}$x$\sqrt{3}$) lattice); b) Corresponding diffraction pattern showing sharp diffraction spots at the ($\sqrt{3}$x$\sqrt{3}$) unit cell reciprocal lattice points and diffuse scattering elsewhere. A (3x$\sqrt{3}$) unit cell is marked.

Si(111)-($\sqrt{3}$x$\sqrt{3}$)R30°Ag reconstruction, where all Ag and Si sites are clearly visible in the scattering potential maps (Grozea, Landree et al. 1999). We also suspect that there may be other ordered structures, and there is some evidence for this already from electron diffraction, LEED (Si(111)-(2$\sqrt{3}$x2$\sqrt{3}$)Au) (Yuhara, Inoue, and Morita 1992a), RHEED (Si(111)-(2$\sqrt{21}$x2$\sqrt{21}$)R10.9°Au) (Khramtsova and Ichimiya 1997), and STM data (Takami et al. 1994). Aside from the structural aspects, an intriguing question is the character of the electronic states in this two-dimensional structure. In addition to standard surface spectroscopic techniques, matching the already available STM data at different biases with theoretical calculations would be very interesting.

CHAPTER 5:

STRUCTURAL INVESTIGATION OF THE 3x1 RECONSTRUCTION

The formation of metallic overlayers on elemental semiconductor surfaces is of continuing scientific and technological interest. The (3x1) reconstruction, a low-coverage metal-induced structure, has been the subject of extensive investigations in the last decade. One of the reasons is its unusual chemical and electronic properties; for example, its presence results in passivation with respect to surface oxidation when induced by alkali metals, and it has an unexpectedly large surface band gap. Another interesting characteristic of the (3x1) structure is the mounting evidence for only one common atomic structure regardless of the identity of the adsorbate.

5.1 Background

Observed first on alkali metal/Si(111) surfaces (Daimon and Ino 1985), the (3x1) reconstruction was also reported to be induced by Ag (Le Lay 1983), Mg (Quinn and

Jona 1991), and Ba (Weitering 1996) on Si(111), and by alkali metals (Fan and Ignatiev 1989) and Ag (Hammar et al. 1993) on Ge(111) surfaces.

Usually, the room temperature adsorption of a submonolayer of alkali metal on a semiconductor surface reduces its work function, enhancing the surface oxidation, e.g. Na, K on Si(111)-(7x7) (Boishin, Tikhov, and Surnev 1991; Muscat, Rjeb, and Roy 1994). In contrast, when the metal is deposited at elevated temperature and the (3x1) structure occurs, its presence promotes a passivation effect with respect to surface oxidation, e.g. Si(111)-(3x1)Na (Tikhov, Surnev, and Kiskinova 1991). In the case of Li deposition, the desorption energy of Li atoms when they are involved in the reconstruction is higher than that of Li atoms desorbing from the Si(111)-(7x7) surface, a result compatible with the passivation of the Si(111)-(3x1)Li structure against oxidation (Kleine et al. 1998). This effect may lead to a lower-temperature gate oxide formation process for the microelectronics industry.

With respect to the electronic properties, because of its single valence electron configuration, the monovalent metal-covered (3x1) surface was expected to be metallic (Jeon et al. 1992). Instead, it has a semiconducting nature with an unusually large surface band gap, around 1eV, on both Si and Ge (Jeon et al. 1992; Carpinelli and Weitering 1996; Weitering and Carpinelli 1997).

The (3x1) structure's atomic geometry was a subject of controversy for a long time. The first pieces of the puzzle came from LEED intensity-voltage (I-V) curves (Fan and Ignatiev 1989; Fan and Ignatiev 1990; Quinn and Jona 1991) which are almost identical regardless of the type of alkali metal causing the reconstruction on the Ge(111) surface and, respectively, of alkali metals, Ag, and Mg on Si(111). Therefore, it was

argued that the structure of the surface was the same irrespective of the adsorbate. In addition, Fan and Ignatiev (1990) inferred that this I-V curves' behavior was indicative of a minute (0.01 ML) metal coverage, a conclusion disputed by Kleine et al. (1998). After being proposed to be as high as 2/3 ML (Daimon and Ino 1985; Wan, Lin, and Nogami 1992; Jeon et al. 1992), adsorbate coverage was later determined to be 1/3 ML based on coaxial impact-collision ion scattering spectroscopy (Hashizume et al. 1993) and AES combined with STM (Fukuda 1994). Okuda et al. (1994) confirmed the metal coverage and estimated the surface Si atom density as four atoms per (3x1) unit cell (however, none of their proposed structure models fits this value). Recently, a precise determination of the number of Si atoms from Si mass transport balance (Hasegawa et al. 1998; Saranin et al. 1998) resulted in the same value.

The STM images of the (3x1) structure on Si(111) and Ge(111) are very similar; they show a cm symmetry plane group with a slight break of the mirror plane in the case of the Ag-induced reconstruction (Jeon et al. 1992; Wan, Lin and Nogami 1992; Hammar et al. 1993; Hashizume et al. 1993; Jeon, Hashizume, and Sakurai 1996; Weitering and Carpinelli 1997). Regarding the electronic properties of the (3x1) surface, the Li (Weitering, Shi, and Erwin 1996), Na (Okuda, Sakamoto et al. 1997), and K (Sakamoto et al. 1994) on Si(111) surface state bond dispersions given by ARPES measurements were alike, and the dispersion width and curvature were similar to those of the π-bonded chain structure on the Si(111)-(2x1) surface (Pandey 1981). SCLS spectra for the Na (Okuda et al. 1994), Li (Weitering, Shi, and Erwin 1996), and Mg (An et al. 1995) (3x1) reconstructions on Si(111) were comparable to each other, in addition to being similar to that of Si(111)-(2x1) (Himpsel et al. 1994).

In summary, the investigation of the (3x1) structure has reinforced the possibility of only one unique structure induced by different metals on the Si(111) and Ge(111) surfaces. This reconstruction has, as distinguishing features, an absolute metal coverage of 1/3 ML and four semiconductor atoms per unit cell, a semiconducting surface with a large band gap, and it is likely to have π-bonded chains formed by the top semiconductor atoms.

Various structural models have been proposed (Fan and Ignatiev 1990; Jeon et al. 1992; Wan, Lin, and Nogami 1992; Okuda et al. 1994; Sakamoto et al. 1994; Weitering et al. 1994; Erwin 1995; Jeong and Kang 1996; Hasegawa et al. 1998; Lottermoser et al. 1998; Saranin et al. 1998). The more plausible and stable from a first-principles total-energy theoretical calculation point of view are those models based on a Seiwatz chain (Seiwatz 1964) with the adsorbate sitting in rows in T_4 or T_1 sites (Okuda et al. 1994; Sakamoto et al. 1994; Weitering et al. 1994), and the model called an extended Pandey chain (Okuda et al. 1994; Erwin 1995), Figure 5.1a,b. While being able to account for the adsorbate-independent nature of the I-V LEED curves, chemical passivation against oxidation, and the semiconducting nature of the surface (but not the large surface band gap (Kang, Kang, and Jeong 1998)), both models were not completely consistent with all of the experimental observations. The Seiwatz and the extended Pandey models' density-functional theory (DFT) calculations of the surface state dispersions were in disagreement with ARPES experimental measurements (Weitering, Shi, and Erwin 1996). Most importantly, these models had an incorrect number of semiconductor atoms in the (3x1) unit cell.

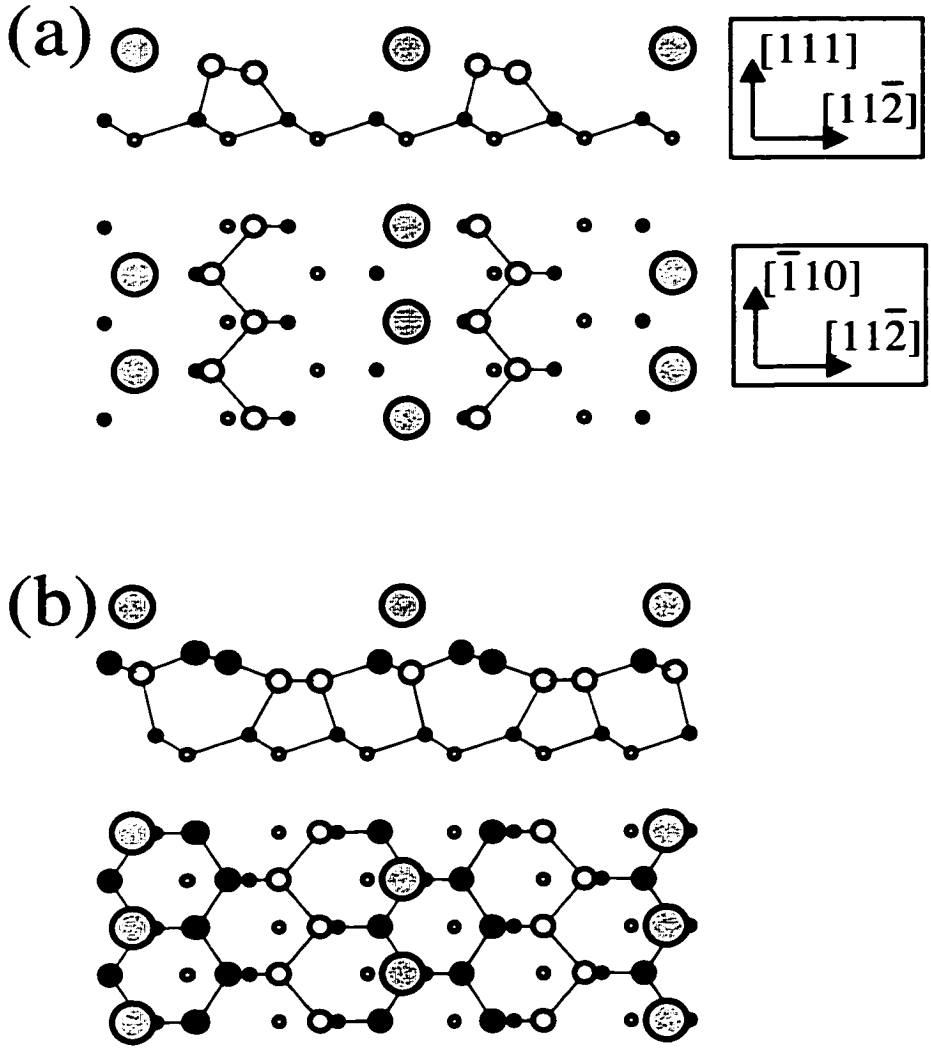

Figure 5.1. Models proposed for the (3x1) reconstruction: (a) Seiwatz chain, and (b) Extended Pandey chain. The grey circles represent adsorbate atoms and all other circles are semiconductor atoms.

5.2 Si(111)-(3x1)Ag

5.2.1 Experimental

Standard TEM samples were prepared from B-doped Si(111) wafers of resistivity 7-30 Ωcm. The 3 mm disks were mechanically thinned, dimpled, and polished to roughly 20 μm at the center. After being chemically etched using a solution of $HF:HNO_3$ 1:9 until small holes, usually surrounded by electron transparent thin areas, appeared, the samples were introduced into SPEAR. Cycles of low energy ion milling (1 keV Ar^+) and direct electron beam annealing were used to clean both sides of the samples.

Surface characteristics were monitored with XPS and off-zone TED. After a sharp, strong Si(111)-(7x7) diffraction pattern was observed in the microscope, Ag was deposited at room temperature only on the side of the sample that has not been exposed to electron beam annealing. A thermal evaporation stage was used, with the pressure never exceeding $2x10^{-10}$ Torr during deposition. An anneal at 550°C for 5 s induced the presence of both (3x1) and ($\sqrt{3}x\sqrt{3}$)R30° phases, Figure 5.2a. Repeating the annealing of the sample converted the surface to only the (3x1) structure, Figure 5.2b.

TED patterns were recorded form two different regions of the sample and at varying values of crystal tilt. Therefore, two data sets were measured and reduced to give a total of 90 different (3x1) surface spots. Of the 90 measured intensities, 56 had errors between 4% and 30%, 26 had errors between 30% and 55%, and 8 had errors between 55% and 90%.

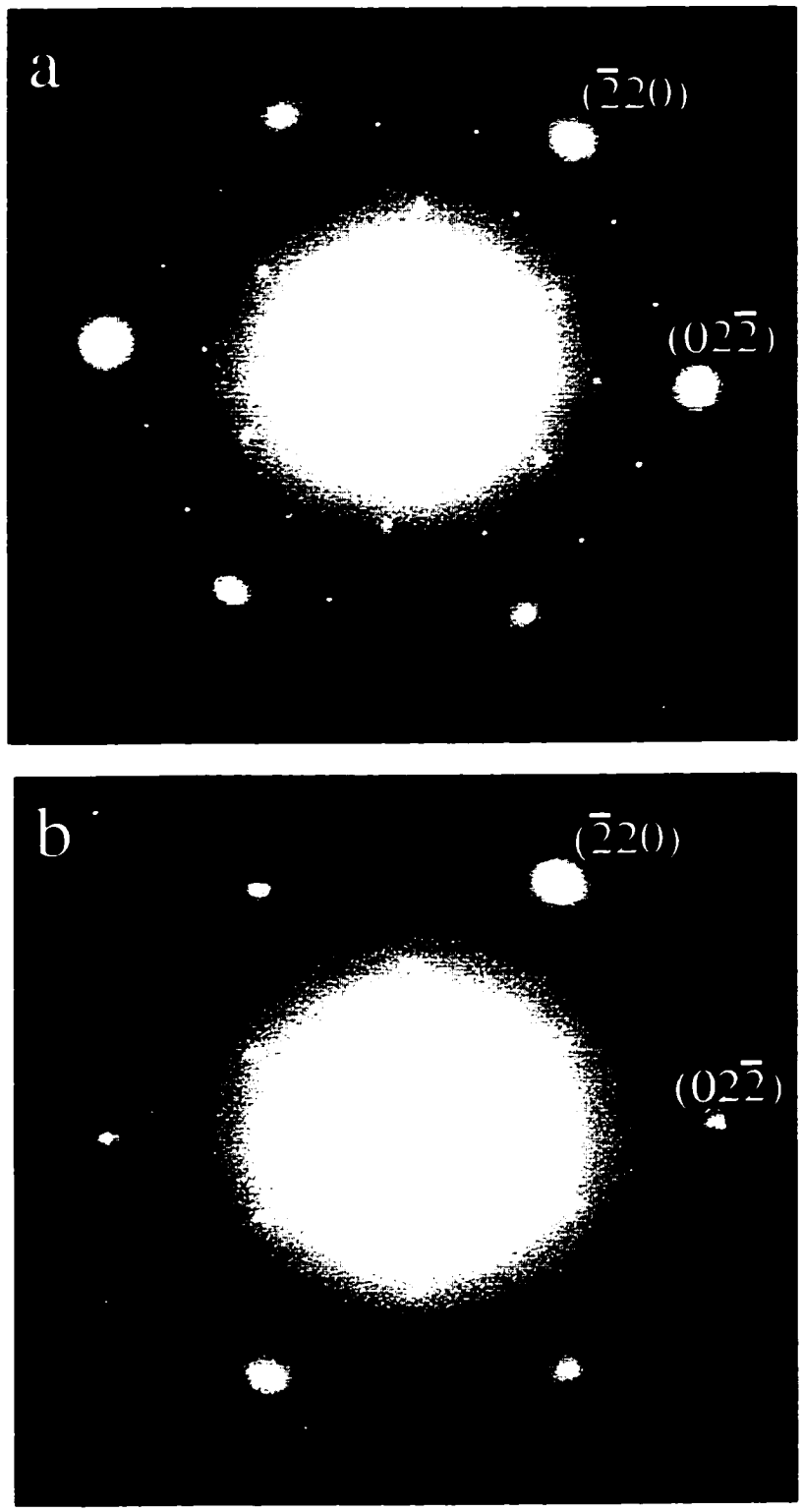

Figure 5.2. Experimental diffraction pattern showing the presence of a) Both (3x1) and ($\sqrt{3}$x$\sqrt{3}$) phases, and b) Only the (3x1) phase.

5.2.2 Initial model

To determine the atomic geometry of the (3x1) reconstruction (Collazo-Davila, Grozea, and Marks 1998), an approach based on Direct Methods to generate initial structure estimates from surface diffraction data was selected.

In the Direct Methods technique, in addition to the measured beam intensities, the possible symmetry of the structure has to be specified. The reported STM images suggest for the (3x1) Ag reconstruction a minor breaking of the mirror plane of the cm symmetry, resulting in a p1 plane group. Therefore, both cases were investigated by generating maps of the scattering potential obeying p1 and cm symmetry respectively.

The contour map of the scattering potential (the other solutions were close variations) shown in Figure 5.3a displays four well-resolved peaks (A-D) along with an elongated area labeled E. The region E was considered to represent either two partially-occupied atom sites or an artifact arising from the lack of a complete set of intensities. For the record, when using a later, improved version of the Direct Methods approach, the area E is replaced by two well-resolved, albeit less intense peaks, Figure 5.3b.

To arrive at an initial model of the structure, various possibilities for the area E were explored. An initial diffraction intensity fitting step was used, kinematically modeling only one layer of atoms and neglecting the effects of the bulk crystal and dynamical diffraction. The area E was finally modeled as two half-occupied Ag sites and the A-D sites as being Si atom positions, with a reduced χ^2 of 4.49. Other permutations of Ag and Si atoms among the A-E sites gave larger χ^2 values, the lowest being equal to 8.46.

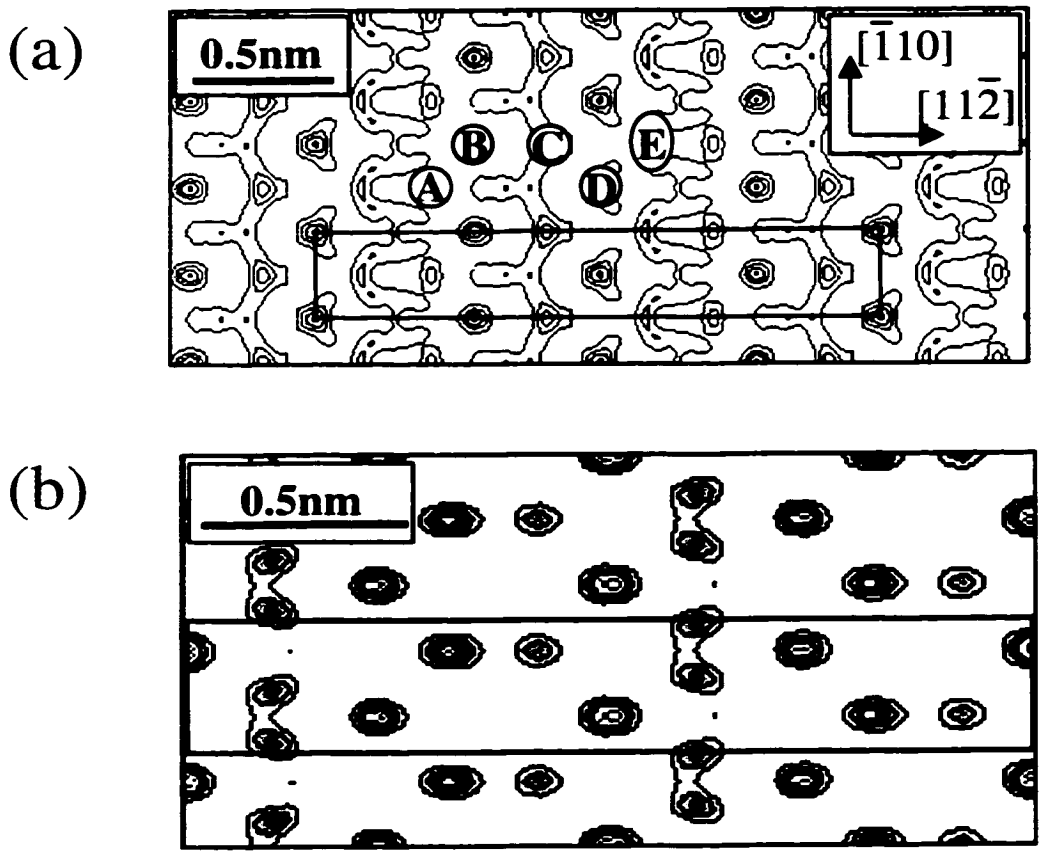

Figure 5.3. a) Contour map of the calculated surface scattering potential using phases estimated through Direct Methods for Si(111)-(3x1)Ag, and b) Contour map of the calculated surface scattering potential using an improved Direct Methods. In each figure a (6x1) cm unit cell is outlined.

5.2.3 Structure Refinement

As the final step, the atomic positions determined from the Direct Methods analysis were refined using a χ^2 minimization with dynamical multislice calculations.

The bulk crystal parameters were found from a multislice calculation by fitting the experimental bulk diffraction intensities with two variables, the angle of crystal tilt and the sample thickness. The values for sample thickness for the two areas investigated, 45 nm and 48 nm respectively, were in agreement with the thickness estimated from PEELS data (Malis, Cheng, and Egerton 1988).

A χ^2 value of 2.81 was obtained for the model while allowing one double layer to relax. The calculations used 14 variables: 12 for the atomic sites and two Debye-Waller factors for Ag and Si surface sites. To model the two equivalent Ag positions, where the Ag atom occupies an asymmetric location with respect to the $[\bar{1}10]$ direction, the occupancy factor for both locations was kept at 0.5.

Keeping the total number of variables between 12 and 16 and always allowing one double bulk layer to relax, the calculations were repeated for the other proposed models from the literature, and resulted in values for χ^2 between 4.33 and 7.54.

Ag and Si atom positions and the Debye-Waller factors for the final fit, which let two bulk double layers to relax and yielded a χ^2 value of 1.62, are shown in Table 5.1 and the model is shown in Figure 5.4. The Ag occupancy factor refined to a value of 0.43, giving a lower coverage than 1/3 ML in accord with Weitering et al.'s (1994) suggestion that different surface preparation conditions may lead to different levels of adsorbate vacancy defects.

Table 5.1. Ag/Si(111)-(3x1) atomic positions in terms of the c(6x1) unit cell in the cm plane group: a=19.953Å, b=3.840Å. All y positions were fixed except for the Ag site, $\sigma_y = \pm 0.0029$. Ag occupancy was fit with 0.43 ±0.04, and isotropic Debye-Waller factors (defined as $B=8\pi^2\langle u^2\rangle$, where $\langle u^2\rangle$ is the mean square atomic displacement) were fit at 6.32 ±1.5 Å^2 for Ag, 3.20 ±0.46 Å^2 for surface Si, and 0.47 ±0.22 Å^2 for layers 1 and 2 of Si. (In pure bulk samples at 280K, B=0.70 Å^2 for Ag and B=0.46 Å^2 for Si [31]).

Atom	x	x [unrelaxed]	y	z [inferred]	σ [layer]	<σ rel>
Ag	0.132	-	0.350	Surface layer	0.0015	0.0015
Si	0.449	-	0.000			
Si	0.028	-	0.000			
Si	0.327	-	0.000			
Si	0.252	-	0.500			
Si	0.000	0.000	0.000	Layer 1	0.0020	0.0012
	0.172	0.167	0.500			
	0.344	0.333	0.000			
Si	0.068	0.056	0.500	Layer 2	0.0040	0.0014
	0.229	0.222	0.000			
	0.397	0.389	0.500			
Si	0.068	0.056	0.500	Layer 3	0.0084	0.0014
	0.235	0.222	0.000			
	0.401	0.389	0.500			
Si	0.139	0.111	0.000	Layer 4	0.0023	0.0009
	0.309	0.278	0.500			
	0.470	0.444	0.000			

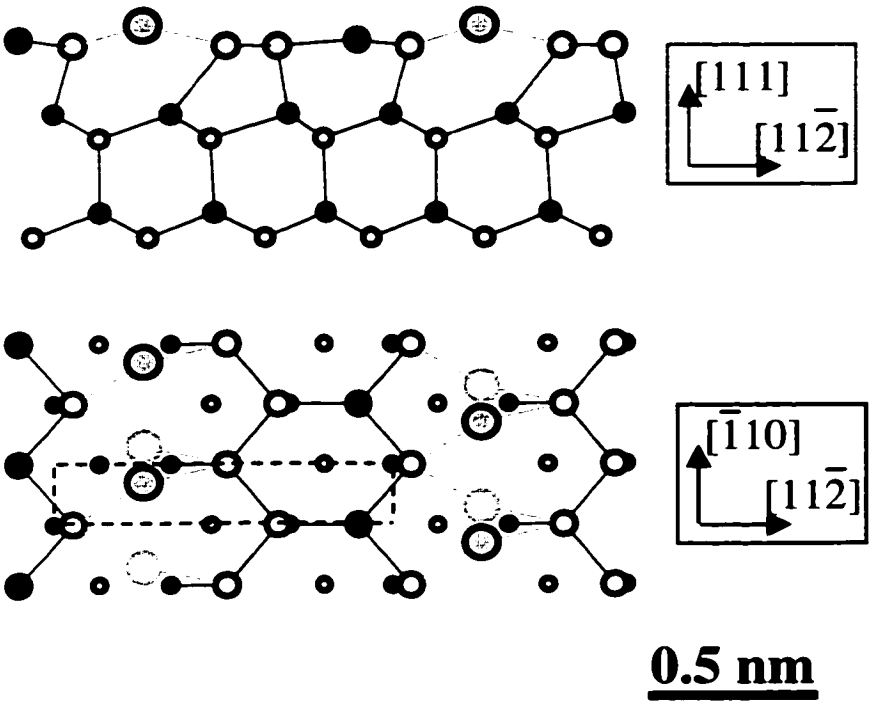

Figure 5.4. Model proposed for the (3x1) reconstruction. The grey circles represent adsorbate atoms (the two equivalent half-occupied Ag sites) and all other circles are semiconductor atoms. One asymmetric unit is outlined in the top view, with the bottom left corner of the unit corresponding with the origin for atomic positions listed in Table 5.1.

5.2.4 Discussion of Results

The (3x1) reconstruction consists of a partial Si double layer with a Si chain and a missing row where the metal is adsorbed. There are two equivalent Ag positions, with the Ag atoms shifted in the same direction for rows parallel to [$\bar{1}$10], breaking the mirror plane symmetry. A similar model was later proposed for alkali metals (Li, Na on Si(111) and Rb on the Ge(111)) from surface x-ray diffraction, LEED I-V measurements, and DFT calculations (Lottermoser et al. 1998). The X-ray model for alkali metals has no deviations from the cm symmetry, leading to an overall accord with STM images for both the alkali metal and Ag cases.

The unusual result for the Ag site agrees well with another STM observation, the flipping of rows in (3x1) domains due to STM tip-surface interaction (Carpinelli and Weitering 1995). The model also correlates well with the LEED I-V curves since it is comprised mostly of silicon atoms. Finally, the proposed model is similar to other linear reconstructions on Si(111), (4x1)-In (Collazo-Davila, Marks et al. 1997) and (5x2)-Au (Marks and Plass 1995), in which a partial silicon double layer containing a Si chain and either one or two missing rows that leave a trench parallel to [$\bar{1}$10] in which the adsorbate atoms lie.

5.3 Theoretical confirmation of the model

Total-energy calculations from first principles (Kang, Kang, and Jeong 1998; Erwin and Weitering 1998) showed the atomic model proposed for the Si(111)-(3x1)Ag reconstruction to be by far more stable than any other models. Erwin and Weitering

(1998) proposed the existence of a true Si double bond (Figure 5.5), possibly one of the reasons for the model's low energy. The model has five-fold rings formed by the Si atoms which create a buckling surface stress that is only partially relaxed by the presence of missing rows, and thus this new element, the Si-Si double bond, may be the cause for the stability of the (3x1) structure. Despite the fact that double bonds are unknown in ordinary compounds of Si and Ge, their possible occurrence at the surfaces of these elements has also been proposed by Seiwatz (1964), based on indirect empirical evidence. In addition, Erwin and Weitering (1998) compared simulated surface band dispersions for Si(111)-(3x1)Li with ARPES experimental measurements, and simulated STM images (filled and empty states) with experimental images finding excellent agreement every time. They also suggested, based on the geometry of this reconstruction, an appropriate name, "honeycomb chain-channel" (HCC), for the solution to the (3x1) structure.

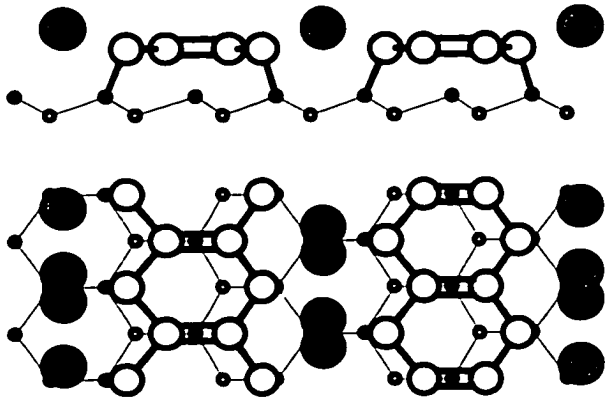

Figure 5.5. Honeycomb chain-channel model with the Si double bond. The grey circles represent adsorbate atoms (the two equivalent half-occupied Ag sites) and all other circles are semiconductor atoms.

Further extensive confirmation of this model came from Kang, Kang, and Jeong (1998), who compared DFT calculations with experimental data from Si(111)-(3x1)Na, reproducing the ARPES band structure, the STM images, the Si 2p SCLS data, and a close value for the energy band gap.

5.4 Ge(111)-(3x1)Ag

The Ag/Si(111) interface has received considerable attention, due partially to the limited reaction or intermixing present, and because it serves as an example of an abrupt interface (Le Lay 1983; Stöhr et al. 1983). Although there are similarities between the systems, Ag/Ge(111) has not been as widely investigated since the interest in germanium surface physics has been rather limited. While both semiconductor surfaces display a π-bonded chain (2x1) reconstruction on the UHV cleaved surface, at elevated temperatures they undergo irreversible transitions to the stable Ge(111)-c(2x8) and the more complicated Si(111)-(7x7) structure, respectively. The lower-coverage Ag phases are also very different (Le Lay 1983). Ag/Ge(111) forms (4x4) and (3x1) structures (around 1/3 ML) prior to forming a 1 ML ($\sqrt{3}$x$\sqrt{3}$)R30° structure. The Ag/Si(111) system forms only the 1/3 ML (3x1) followed by the 1 ML ($\sqrt{3}$x$\sqrt{3}$)R30° structure. The ($\sqrt{3}$x$\sqrt{3}$)R30° surfaces have the same basic structure in both cases (Huang et al. 1994). Ge(111)-(3x1)Ag has only been seen as small insets, narrow strips at most two unit cells wide, bordering large (4x4) domains or between the (4x4) domains and domains of the native Ge(111)-c(2x8) reconstruction, in STM images (Hammar et al. 1993; Weitering and Carpinelli 1997; Spence and Tear 1998). The filled and empty state STM images were

very similar to those of Si(111)-(3x1)Ag (Hammar et al. 1993; Weitering and Carpinelli 1997).

5.4.1 Experimental

Ge(111) samples were prepared by cutting 3 mm disks from undoped Ge(111) wafers of resistivity greater than 40 Ωcm (Grozea, Bengu et al. 1999). The samples were thinned, dimpled, polished, and chemically etched to electron transparency in a diluted solution of $HF:HNO_3$ 1:10. After sample transfer to SPEAR, both sides of the samples were cleaned by cycles of low energy (1 keV) argon ion milling and direct electron beam annealing (400° C for 30 min).

Surface characteristics were monitored with XPS and off-zone TED. The sample processing resulted in good TED patterns with clearly visible 1/2 order spots of the c(2x8) structure. Ag was deposited in situ at room temperature using a thermal evaporation stage, only on the side of the samples that was not exposed to electron beam bombardments during annealing. The Mo boat used was carefully outgassed prior to deposition with the base pressure never exceeding $1x10^{-10}$ Torr during depositions. Ag coverage was estimated utilizing the relative Ag and Ge 3d XPS peak intensities.

TEM images were collected at room temperature using an electron beam voltage of 200 kV to limit beam damage effects. Dark field images were taken using an objective aperture large enough to include only one (220) bulk Ge spot and surface diffracted beams. The final TED data set was comprised of 29 measured intensities with small errors: only one beam had an error of 45%, three beams had errors between 21% and 30%, and the remaining errors were under 21%.

5.4.2 Initial model

After Ag deposition at room temperature on the Ge(111)-c(2x8) surface and a 400° C anneal of the specimen for a few minutes, TED patterns displayed the (4x4) reconstruction. Dark field images, Figure 5.6a, show large triangular domains of the (4x4) phase, and its corresponding (4x4) diffraction pattern is displayed in Figure 5.6b. On some of the edges of the triangular (4x4) domains, one or two linear features can be observed. They belong to the (3x1) structure, present only as narrow strips similar to those reported from STM data.

Repeated annealing of this surface, again at 400° C for a few minutes, produced the transformation of the (4x4) phase into large, independent (3x1) domains and ($\sqrt{3}$x$\sqrt{3}$)R30° regions. Dark field images, Figure 5.7a, show the complete disappearance of the (4x4) phase and the presence of (3x1) domains. No triangular (4x4) domains can be observed anymore, and only linear features due to the (3x1) phase are visible throughout the figure. The TED pattern, Figure 5.7b, exhibits both (3x1) and ($\sqrt{3}$x$\sqrt{3}$) phases.

The TED data were analyzed using the Direct Methods aproach and heavy-atom holography. Figure 5.8 shows a contour map of the scattering potential; all the other solutions were practically the same. Compared with Figure 5.3, which shows the solution obtained for the case of Si(111)-(3x1)Ag based on a larger data set, the presence of several additional features in Figure 5.8 is observed, leading to two possible alternatives: (a) the atomic structure for Ge(111)-(3x1)Ag is different than the HCC model, the solution for the Si(111) case (and moreover, different than another similar case, Rb on

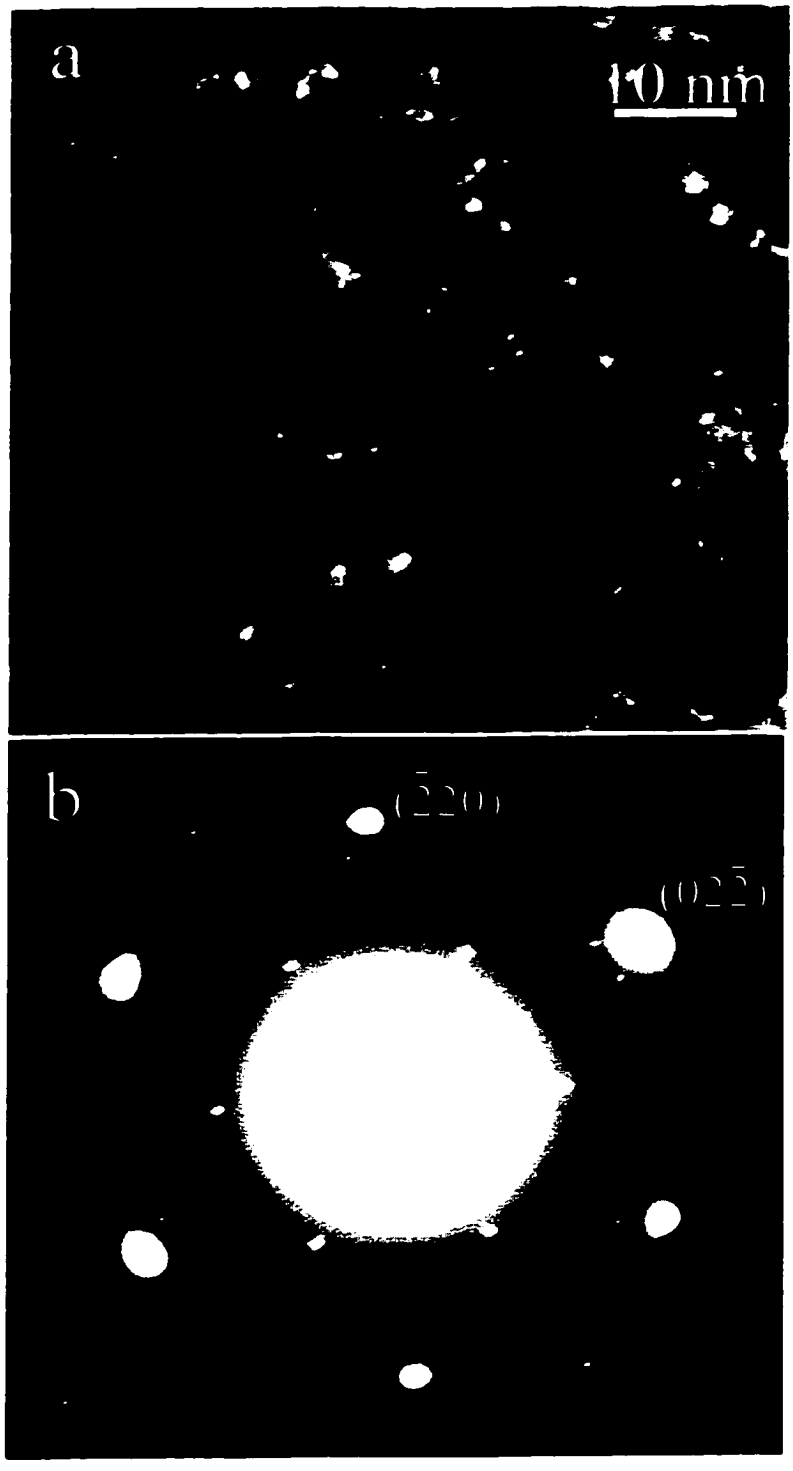

Figure 5.6. (a) Dark field image of the (4x4) triangular domains with narrow strips of (3x1) structure visible on the edge as one or two linear features, and (b) Corresponding (4x4) diffraction pattern.

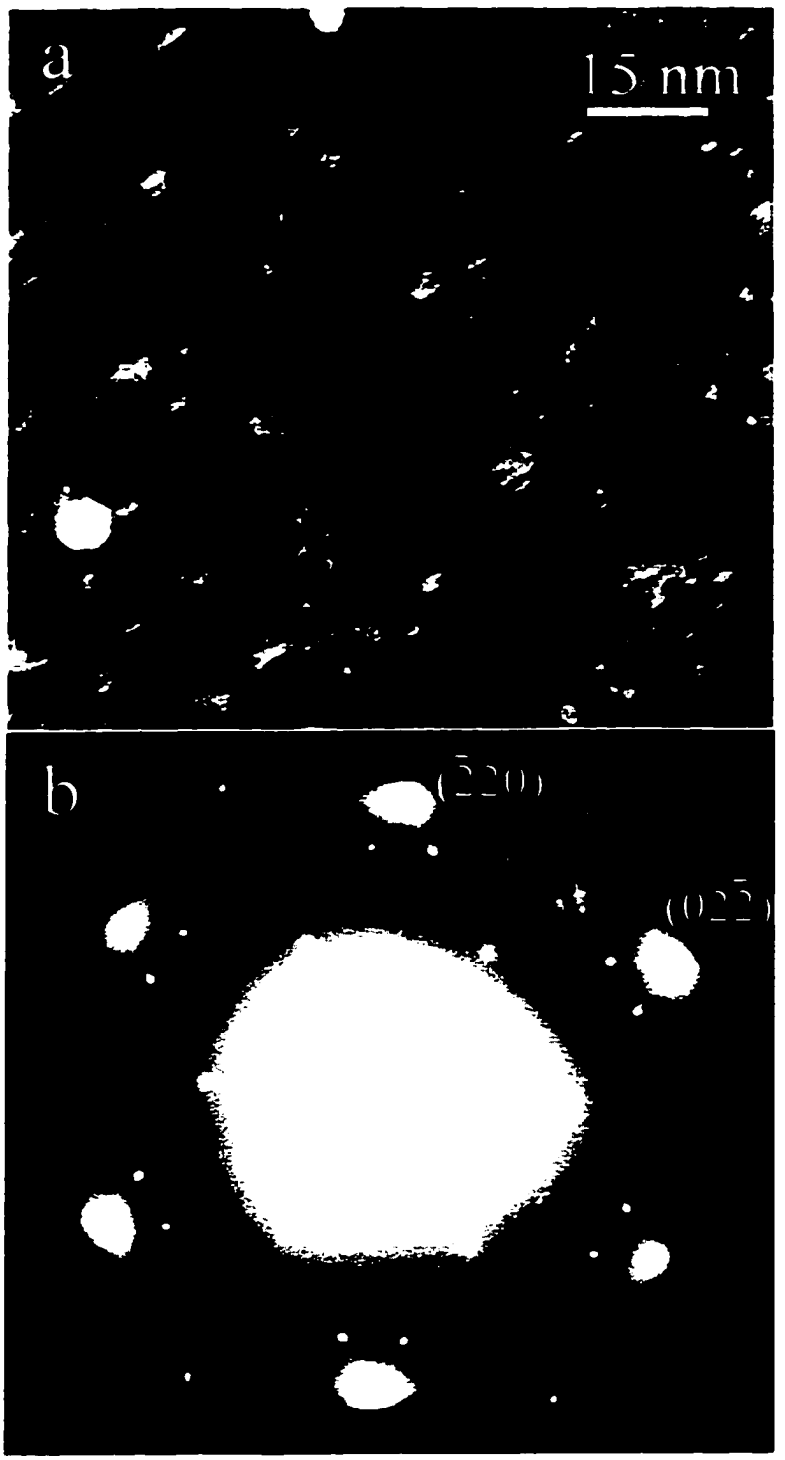

Figure 5.7. (a) Dark field image showing linear features due to one domain of the (3x1) structure, and (b) Corresponding diffraction pattern displaying both (3x1) and ($\sqrt{3}$x$\sqrt{3}$) phases.

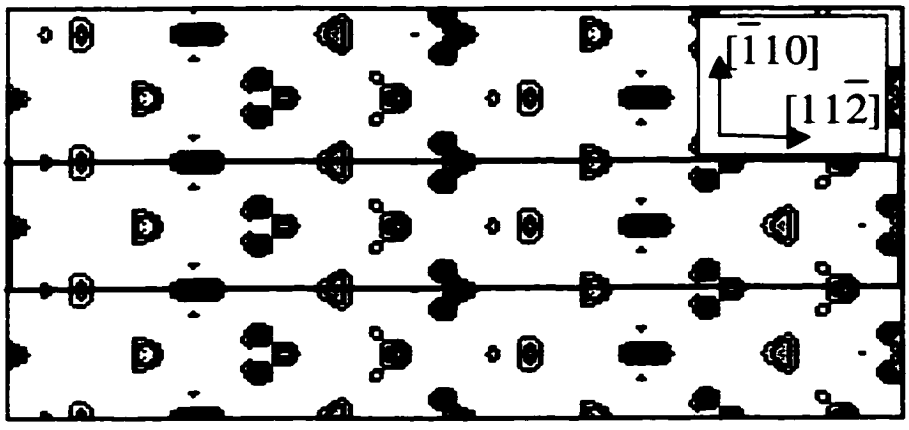

Figure 5.8. Contour map of the calculated surface scattering potential using phases estimated through Direct Methods for Ge(111)-(3x1)Ag. In the center of the figure a (6x1) cm unit cell is outlined

Ge(111)); or (b) the extra features are artifacts, and not atomic sites, due to missing information in the relatively smaller experimental data set.

To determine the correct alternative, the maps were used to construct several models by combining iterative steps of refinement of the atomic positions with heavy-atom holography (Marks and Plass 1995; Grozea, Landree et al. 1999). At the end of this analysis, an HCC model similar to the solution for the Si(111) (3x1) reconstruction proved to be the best model with a quick drop to the lowest value of R and no suggestion of new strong peaks by the maps. Other models based on different arrangements of Ge atoms and using full occupancy of Ag led to higher values of R and/or induced the algorithm to move the atoms to sites close to those of the Si(111) case.

5.4.3 Structure Refinement

As the next step, the atomic positions of the model were refined using a χ^2 minimization with full dynamical multislice calculations including the effects of bulk crystal diffraction and dynamical effects to arrive at the final structure. The bulk crystal parameters were determined similarly to the Si(111)-(3x1) case. The sample thickness was 47 nm, as confirmed by the comparison of simulated and experimental diffraction patterns.

A reduced χ^2 value was calculated for the model while allowing one bulk double layer to relax. It gave a χ^2 value of 6.73. The number of variables (atomic positions, Debye-Waller factors for Ag and top surface Ge sites, and a scaling factor) was equal to 15 for 65 data points. The Debye-Waller factor for the relaxed bulk double layer was fixed at the value for bulk Ge. The occupancy factor for the two equivalent Ag sites was kept at 0.5, as in the Si(111)-(3x1)Ag case.

Keeping the same total number of variables and one relaxed bulk double layer, the calculations were repeated for the other models. The x-ray model, with the position for the adsorbed atom not breaking the cm symmetry, gave a χ^2 of 8.2, while the extended Pandey and Seiwatz models yielded values between 9.0 and 15.0.

Further refinement of the HCC model, letting a second bulk double layer relax, reduced χ^2 to 3.01, with the number of variables increased to 21. Again the Debye-Waller factors for both relaxed bulk double layers were set. Adding the occupancy factor for Ag as an additional parameter, together with a variable Debye-Waller factor for the first relaxed bulk double layer, led to a χ^2 value of 2.51, with 23 variables. The Ag

occupancy refined to 0.48, confirming the disordered placement of Ag in the two equivalent sites.

5.4.4 Discussion of Results

In addition to the three structural elements, adatoms, dimers, and π-bonded chains, which are frequently encountered as "building blocks" of the Si and Ge reconstructions, Erwin and Weitering (1998) proposed a new one, a true Si double bond, to explain the very low energy of the HCC model for the Si(111)-(3x1) structures.

The similarity between the Ge(111)-(3x1)Ag and Si(111)-(3x1)Ag structures may lead to the conclusion that the unusual double bond is not limited to Si but can also be formed by Ge atoms. Moreover, this double bond could be significant in stabilizing other reconstructions. With respect to the Ag/Ge(111) system, we have already mentioned that the (3x1) has been observed as small domains bordering large (4x4) areas, a reconstruction which occurs at a slightly higher Ag coverage. It has also been suggested (Collazo-Davila et al. 1998) that the two structures are related and a double bond formation in this case also eliminates all the dangling bonds from the (4x4)'s Ge ring and contributes to its stability.

Based on the links between the (3x1) and (4x4) structures and the models for their atomic geometry, we propose a model for the domain boundary between the two phases, Figure 5.9. The structures are shown with one relaxed bulk double layer, leading to the apparent minor misalignment of the substrate. The (4x4) structure is composed of two triangular subunits and Ge trimers at the corners of the unit cell. One triangular subunit is a missing top layer reconstruction with six Ag atoms situated on Ge substitutional sites

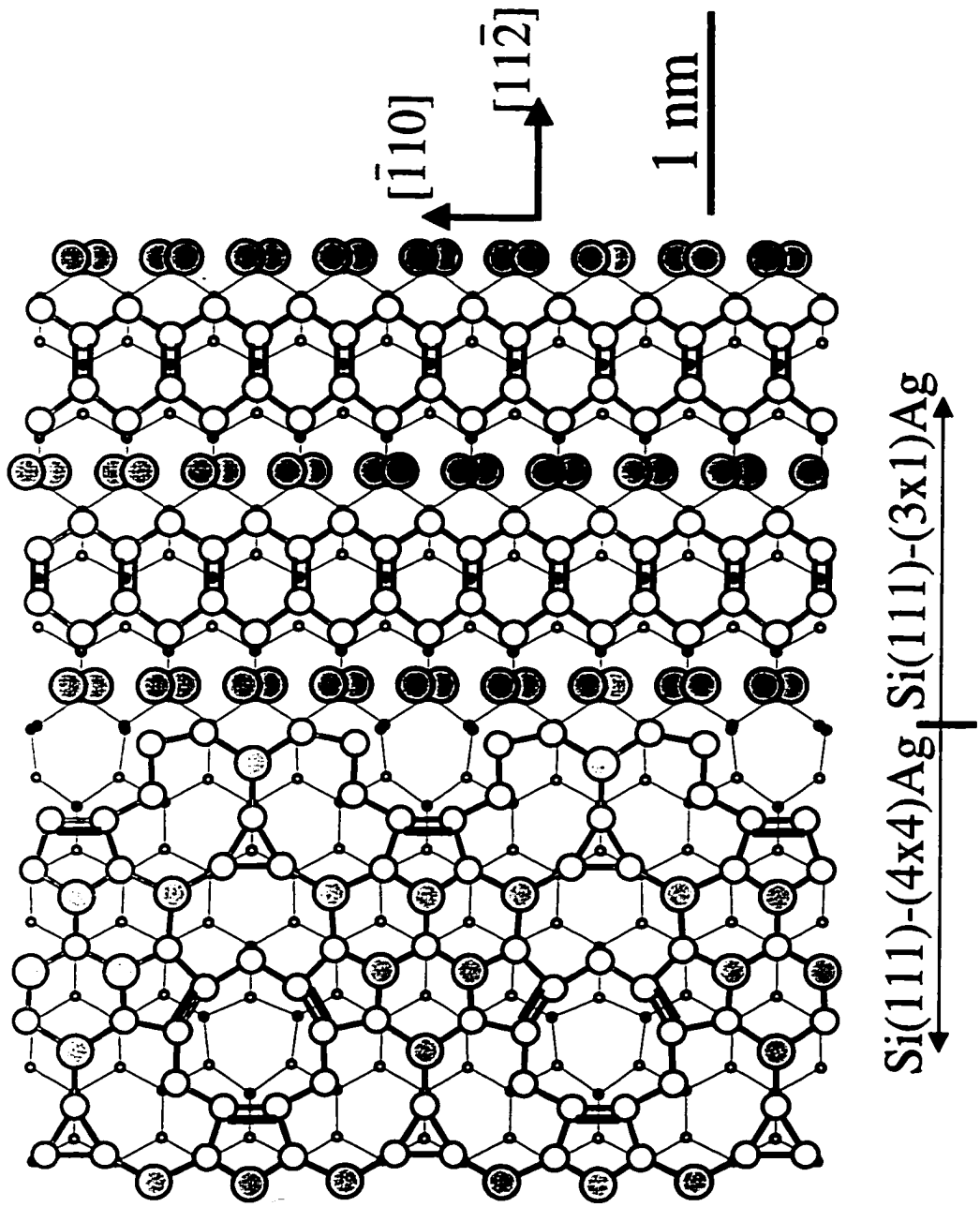

Figure 5.9. Domain boundary model for the boundary between (4x4) and (3x1) structures.

and shows six protrusions in filled-state STM images. The other subunit has a ring-like assembly of nine Ge atoms. The domain boundary model matches STM images well (Hammar et al. 1993; Weitering and Carpinelli 1997; Spence and Tear 1998) and requires only the removal of one Ge atom from the Ge ring and the replacement of two Ge atoms with Ag atoms in the same region. In the other subunit, the remaining Ag atoms correspond to the protrusions adjacent to the (3x1) structure observed in filled-state images. The row from (3x1) which is closest to the (4x4) structure has been proposed by Spence and Tear (1998), using evidence from STM images, as being formed by Ag atoms, in agreement with our proposed model. They also suggested that this row's enhanced contrast , observed in filled-state STM images, is some form of charge transfer to the Ag atoms taking place in the nearby (4x4) region.

The (3x1) structure used to be considered not worth mentioning in the surface phase diagram of the Ag/Ge(111) system, since it was believed to not exist over any extended regions of the surface. This study clarifies the question of its existence and stability, and also provides a better understanding of the (4x4) reconstruction. This latter phase is metastable at room temperature and, after an appropriate thermal treatment, dissociates into (3x1) and ($\sqrt{3}$x$\sqrt{3}$) domains. With the atomic geometry solved for all the phases in the submonolayer regime, as well as the relationships between them, it may be possible to approach this system in a manner similar to the work of Plass and Marks (1997), which proposed a complete surface phase diagram for Au/Si(111) system in the same coverage regime.

It would not be unexpected that this system reserves more surprises, such as the presence of large (3x1) domains. Spence and Tear (1998) reported the existence of a

region of (5x1) periodicity in single domains between rows of (3x1). One might suspect its structure to be a linear reconstruction related to the (3x1) structure.

CHAPTER 6:

SURFACE PHASE DIAGRAMS

The overview of the literature on thin metal deposits on clean semiconductor surfaces, in particular for the Au/Si(111) and Ag/Ge(111) systems, shows a great difference in the number of studies. The Au/Si(111) and Ag/Si(111) interfaces are some of the most extensively investigated. For the Au/Si(111) system, an almost complete characterization of the formation of surface phases, as well as their energetic and electronic properties, has been achieved. Despite this effort, numerous questions remain unanswered. For the Ag/Ge(111) system, the available information is at best fragmentary.

One of the key points in understanding the interaction of metals with semiconductor surfaces during the initial stages of interface formation is the detailed rearrangement of their atoms for every surface phase. Recently, several reports have provided this information for the (5x2) Au (Marks and Plass 1995) and ($\sqrt{3}$x$\sqrt{3}$) Au (or α($\sqrt{3}$x$\sqrt{3}$) Au) (Plass and Marks 1995) surface structures in the submonolayer region of the Au/Si(111) system, and the (6x6) Au and the so-called β($\sqrt{3}$x$\sqrt{3}$) Au structures in the

supermonolayer region (Au coverage up to 1.5 ML) (Grozea at al. 1998; Marks, Grozea et al. 1998). The β(√3x√3) surface phase is the one which displays a (√3x√3) + ring-like diffraction pattern, as mentioned in Chapter 4. In the submonolayer regime of the Ag/Ge(111) system, the atomic arrangements of the (4x4) Ag phase (Collazo-Davila et al. 1998), the (3x1) Ag phase (Grozea, Bengu et al. 1999), and the (√3x√3) structure (Huang et al. 1994; Göthelid et al. 1995; Spence and Tear 1998) have also been established.

Based on the atomic geometry of all phases present and the interphase relationships, this chapter will present a survey of the results of all relevant experimental reports and tentative surface phase diagrams for the Ag/Ge(111) system in the submonolayer regime and the Au/Si(111) system in the supermonolayer regime.

6.1 Background

The solution of the atomic structure for the two main surface phases of the Au/Si(111) system in the submonolayer regime, in conjunction with results from numerous recent studies on this system, cleared the way for a new approach to surface phase understanding. The traditional view was based on familiar phase maps, or 'schematic phase diagrams', showing the temperature versus metal coverage regime for the various surface structures. Instead, Plass and Marks (1997) proposed a true phase diagram obeying the Gibbs phase rule and with phase boundaries based on thermodynamic principles shown in Figure 6.1. Their analysis was limited to the submonolayer region, although the figure encompasses experimental observations from

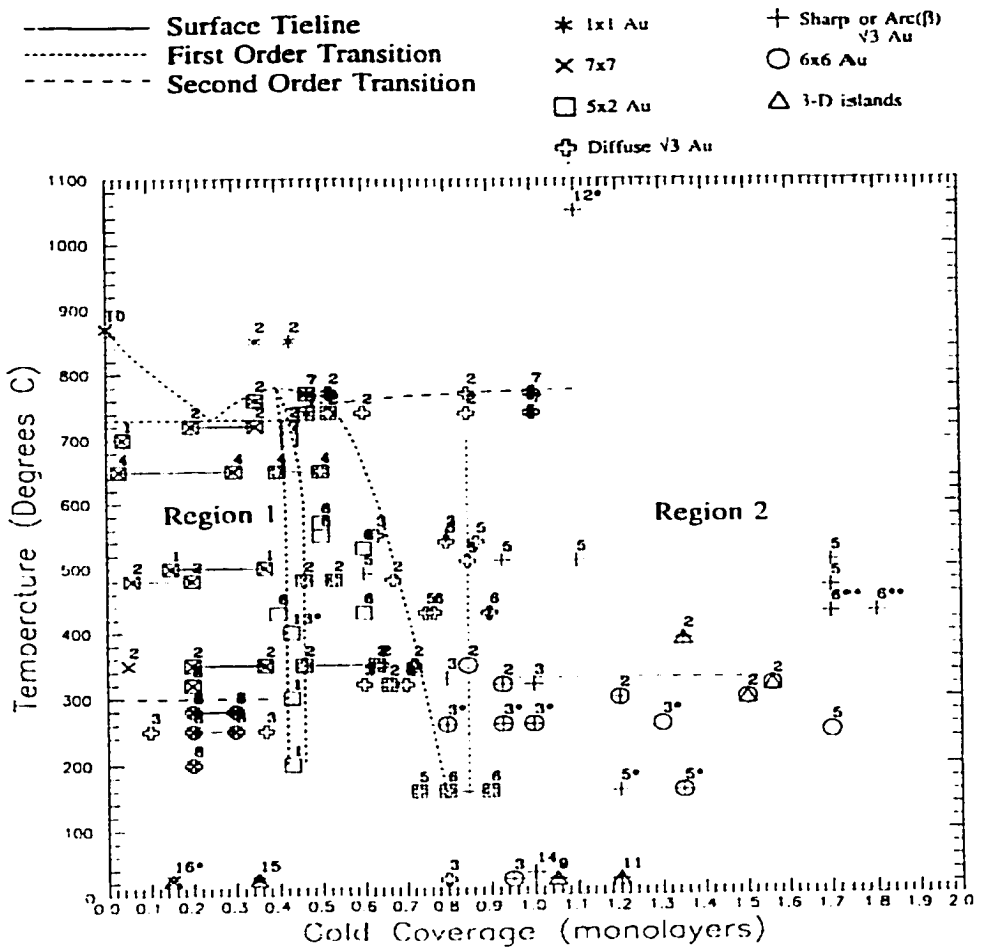

Figure 6.1. Surface phase diagram for the Au/Si(111) system proposed by Plass (1996) (Region 1 – submonolayer coverage) with in situ experimental results. Region 2 (1 ML – 2 ML coverage) displays experimental data points. Data points taken from coverage estimates based on the reference's images have starred (*) reference numbers. The number above a data point corresponds to its reference as follows: 1 = Hasegawa et al. 1991; Hasegawa, Hosaka, and Hosoki 1992; Hasegawa, Hosaka, and Hosoki 1996; 2 = Święch, Bauer, and Mundschau 1991; 3 = Takahashi, Tanishiro, and Takayanagi 1991; 4 = Tanishiro and Takayanagi 1989; 5 = Yuhara, Inoue, and Morita 1992a; 6 = Yuhara, Inoue, and Morita 1992b; 7 = Daimon et al. 1990; 8 = Shibata, Kimura, and Takayanagi 1992; 9 = Fuchigami and Ichimiya 1996; 10 = Miki et al. 1992; 11 = Ichimiya et al. 1995; 12 = Kamino et al. 1996; 13 = Minoda et al. 1992; 14 = Plass, Marks, and Dorset 1996; 15 = Berman, Batterman, and Blakely 1988; 16 = Meinel and Katzer 1992.

the literature up to 2 ML. The data points have errors of at least ± 0.04 ML on the Au coverage and ± 10° C on temperature. The estimation is based on typical limitations of quartz monitors, AES, and RBS for coverage measurements, and of pyrometers for temperature measurements, respectively. They redefined the reconstructions in terms of 'line compounds' or 'surface solutions'. As both (5x2) Au and ($\sqrt{3}$x$\sqrt{3}$) Au phases can sustain varying Au contents, they are considered surface solutions. Plass and Marks (1997) used a set of dashed curves to represent potential phase boundaries, since they have not been derived from any energy parameters. A similar approach has been employed for the present study.

An important point from their analysis is the distinction between studies reporting structural observations at the same temperature at which the structure formed and investigations in which the structure was observed at a lower temperature than the formation temperature. Regardless of this difference, both data sets follow the same general trends provided that the larger coverage and temperature uncertainties in the latter data set are considered. While this separation can be taken into account when analyzing the supermonolayer regime of Au/Si(111), this study will focus mostly on the former type of experimental observations. However, the majority of Ag/Ge(111) observations were performed at a lower temperature than the phase formation temperature. At least for this case, there are no reported differences between structures formed when the metal is deposited on a heated substrate and those induced on the surface by annealing the system after the metal is deposited at room temperature (Spence and Tear 1998; Göthelid et al. 1995).

A phase diagram is a map obeying Gibbs phase rules and showing which phases exist in equilibrium for any combination of temperature and composition. The equilibrium structure is also a function of pressure. However, the existence of a surface reconstruction usually requires UHV conditions and thus, for most purposes, the effects of pressure can be ignored.

The analysis of the surface phase diagram for a certain system is further complicated by the presence of several poorly characterized phases. Some of them are metastable, due mostly to kinetic effects, and are induced by allowing the rapid cooling of the system. Often, achieving the equilibrium phase requires careful control of the cooling conditions. We propose the use of a set of curves commonly referred to in physical metallurgy as T-T-T curves as a way to represent the metastable structures present in surface phase systems (Barrett, Nix, and Tetelman 1973). The T-T-T curves derive their name from time, temperature, and transformation. They provide information on the time that elapses, at any selected temperature, before the transformation begins and until it is finished. Figure 6.2 shows, in addition to an isothermal transformation, how the transformation occurs when an alloy is continuously and slowly cooled (curve S), when most of the transformation occurs at high temperature, versus at a fast continuous cooling rate (curve F), when most of the transformation occurs at low temperatures.

An assumption required for a sound thermodynamic evaluation is that the system under analysis is closed with respect to the amount of its constituents. Surface diffusion can occur simultaneously with competitive processes like desorption and bulk diffusion.

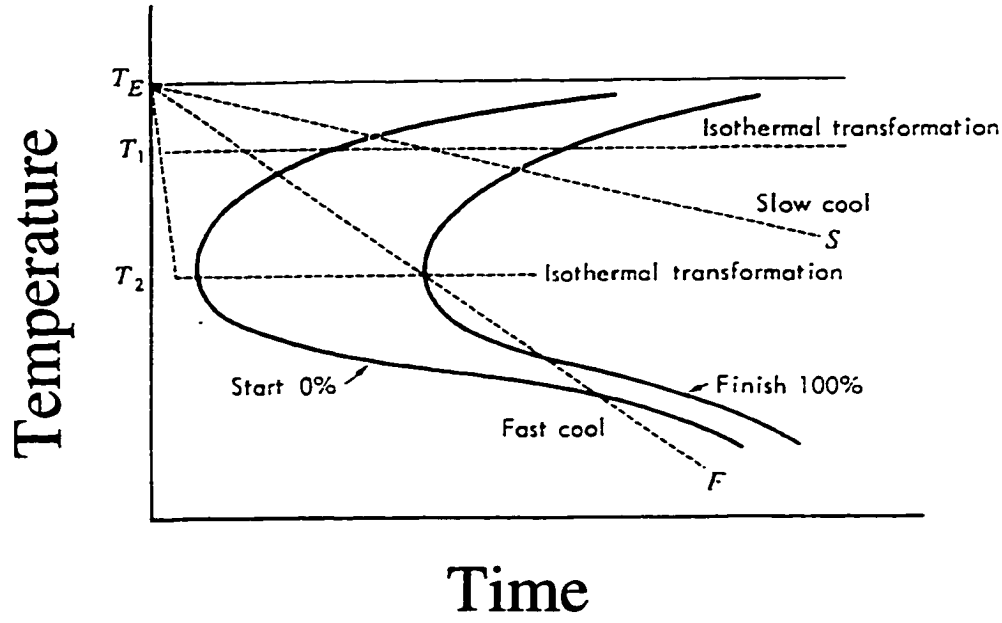

Figure 6.2. T-T-T curve: effects of cooling rate and temperature on the transformation rate (after Barrett, Nix, and Tetelman 1973).

For the case of Au/Si(111) system, under particular temperature and Au coverage conditions, the surface migration process takes place at the same time as the diffusion of Au atoms into the bulk. Yuhara, Inoue, and Morita (1992b) reported an activation energy of 1.3 eV for Au atoms diffusing into bulk Si for Au coverages around 1.7 ML, with an increase to 2.5±0.5 eV for Au diffusion from the $\alpha(\sqrt{3}x\sqrt{3})$ surface at moderate temperatures (between 400° C - 600° C). Desorption starts to play a role at temperatures over 800° C. Le Lay, Manneville, and Kern (1977) determined, based on AES data, that the desorption energies of Au atoms from greater than 1 ML coverage structures and from the $\alpha(\sqrt{3}x\sqrt{3})$ surface are 3.3 eV and 3.6 eV, respectively.

Suliga and Henzler (1983) claimed, in contrast to the Au/Si(111) system, no significant Ag diffusion into bulk Ge for the Ag/Ge(111) system under 1 ML coverage. Silver atoms on Ge(111) surface start to desorb at around 550° C-600° C. Therefore, both systems under investigation, Au/Si(111) and Ag/Ge(111), can be considered closed, a reasonable approximation within a certain temperature range, metal coverage, and length of time.

6.2 The Ag/Ge(111) system

The conventional schematic phase diagram for the Ag/Ge(111) system proposed by Le Lay (1983) is shown in Figure 6.3. When Ag is deposited on the Ge(111) native

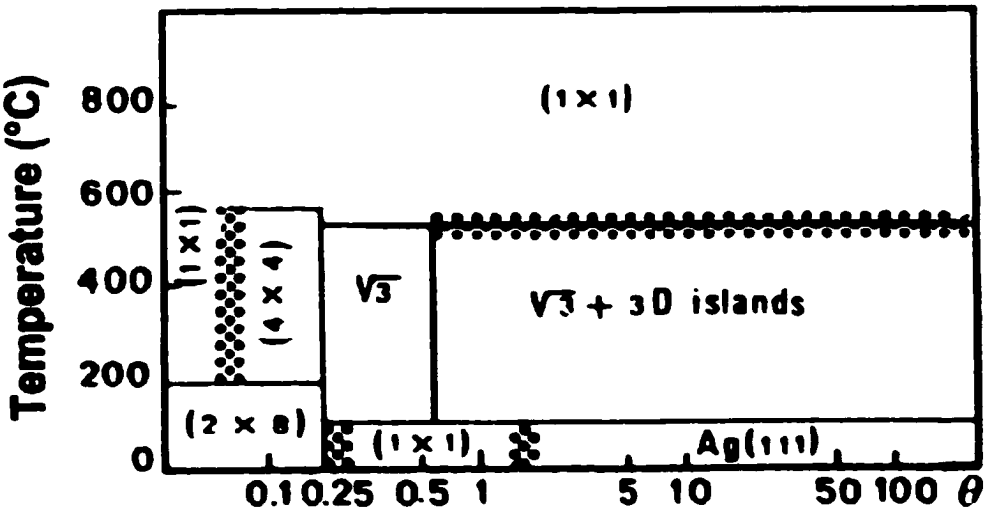

Figure 6.3. Schematic phase diagram of the Ag/Ge(111) system proposed by Le Lay (1983).

reconstruction (the Ge(111)-c(2x8) surface), the interface may undergo a (3x1) Ag, a (4x4) Ag, and eventually a ($\sqrt{3}$x$\sqrt{3}$)R30° Ag reconstruction at a substrate temperature

between 200° C and 450° C in the submonolayer regime. For Ag coverages above 0.1 ML, a (4x4) phase is observed, initially coexisting with the c(2x8) surface. This phase was first reported to be complete at 0.27 ML (Bertucci et al. 1979) and later at 0.375 ML (Collazo-Davila et al. 1998; Spence and Tear 1998). Hammar et al. (1993) identified for the first time a (3x1) structure existing only as small insets at the boundaries of the (4x4) and c(2x8) phase domains. Grozea, Bengu et al. (1999) reported the existence and stability of the (3x1) phase over large areas and with a nominal coverage of 0.33 ML. Upon further deposition of Ag, the (4x4) structure gradually disappears and is replaced by a ($\sqrt{3}$x$\sqrt{3}$) phase which appears to cover completely the surface at 1 ML.

The ($\sqrt{3}$x$\sqrt{3}$) phase has a honeycomb-chained trimer structure (Huang et al. 1994; Göthelid et al. 1995; Spence and Tear 1998) similar to that of the ($\sqrt{3}$x$\sqrt{3}$) surface in the Ag/Si(111) system (Takahashi and Nakatani 1993). The reconstruction can be described as a missing top layer, in which Ag atoms substitute the first layer Ge atoms in positions slightly displaced from bulk sites while the remaining Ge atoms in the topmost double layer form trimers. The correspondence between atomic models for (3x1) and ($\sqrt{3}$x$\sqrt{3}$) structures of Ag on both Si(111) and Ge(111) can account for a similar link between the two structures on Ge(111) as on Si(111) (Collazo-Davila, Grozea, and Marks 1998). This points to a similar local bonding geometry, in which each Ag atom bonds most strongly to a single semiconductor atom from the semiconductor chain and has two other atoms surrounding it in the (3x1) phase and, in the ($\sqrt{3}$x$\sqrt{3}$) phase, the Ag atom bonds most strongly to a single semiconductor atom from the trimer and has two others as neighbors.

The (3x1) structure, as well as its relationship to the (4x4) phase and the common double bond formation, has been discussed extensively in Chapter 5. The (3x1) surface can be described as a partial Ge double layer containing a Ge chain and one missing row, leaving a trench in which the Ag atoms lie (Grozea, Bengu et al. 1999).

The (4x4) surface consists of a missing top layer reconstruction with the Ag atoms placed on Ge substitutional sites in one triangular subunit. The other triangular subunit contains a ring-like assembly of Ge atoms with double bonds eliminating all the dangling bonds and contributing to the ring's stability. The formation of this unusual Ge-Ge double bond is a feature shared with the (3x1) phase. The (4x4) structure also has trimers of Ge atoms, similar to the trimers found on the ($\sqrt{3}$x$\sqrt{3}$) surface, at the corners of the unit cell (Collazo-Davila et al. 1998). The Ge trimer with the three nearest Ag atom neighbors matches the basic structural unit of the ($\sqrt{3}$x$\sqrt{3}$) phase. The partially occupied Ag sites included by Collazo-Davila et al. (1998) in their final model suggest that the (4x4) phase is a surface solution with a lower coverage boundary at 0.375 ML and an upper coverage boundary of 0.5625 ML. They also reported, for the first time, the presence of a disordered (4x4) phase, a quenched structure with a diffraction pattern displaying ring-like motifs around the ($\sqrt{3}$x$\sqrt{3}$) spots and remarkably similar to the unique diffraction patterns of β($\sqrt{3}$x$\sqrt{3}$) in the Au/Si(111) system, Figure 6.4.

Bertucci et al. (1979) proposed a kinetic model of desorption for the (4x4) and ($\sqrt{3}$x$\sqrt{3}$) structures, in which desorption is assumed to occur indirectly through surface diffusion from the domain edge. Their model resulted in sublimation energies of 2.93 eV and 3.3 eV for ($\sqrt{3}$x$\sqrt{3}$) and (4x4), respectively.

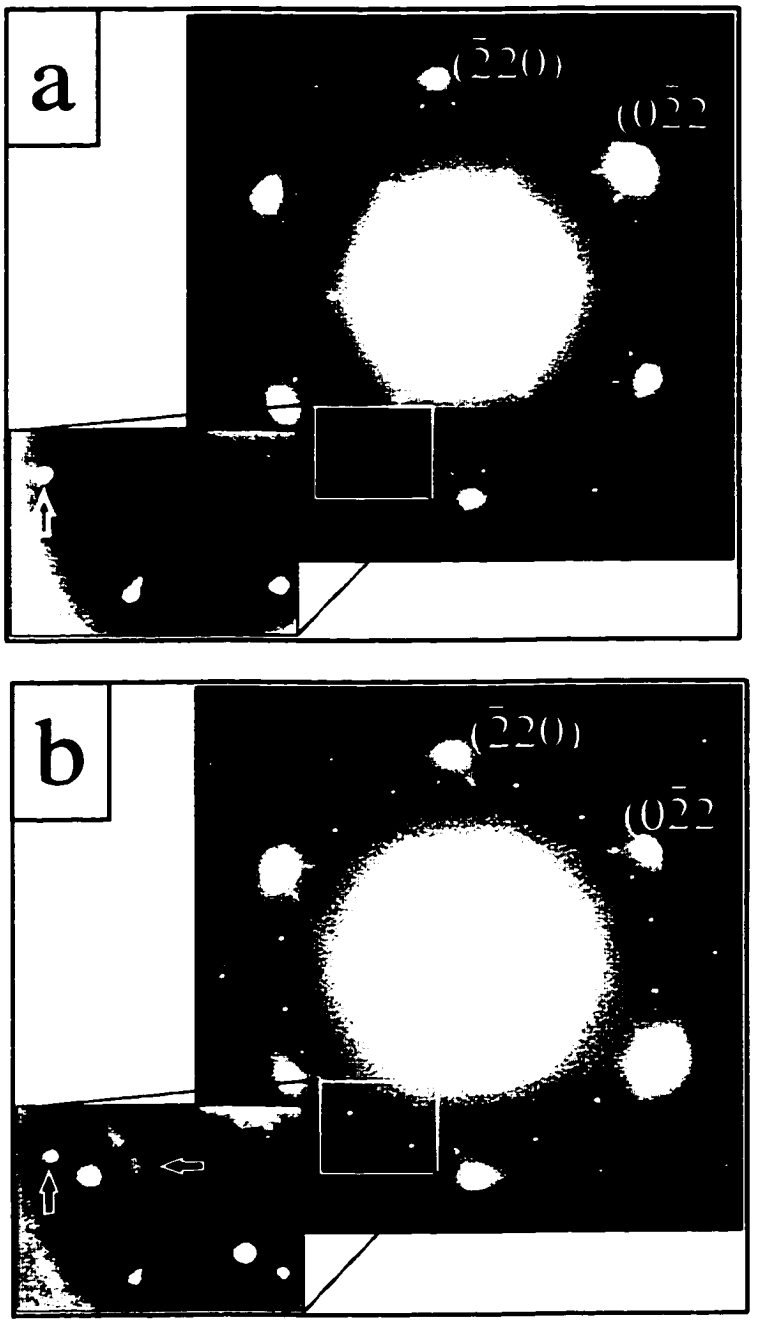

Figure 6.4. TED patterns taken close to a Ge(111) zone-axis. a) From a region covered by the (4x4) structure, and b) From a region with both (4x4) and ($\sqrt{3}$x$\sqrt{3}$) domains. The magnified region in (b) shows diffuse rings (horizontal arrow) surrounding the most intense ($\sqrt{3}$x$\sqrt{3}$) spots. The diffuse rings are not present in (a). The vertical arrows point to the same (4x4) surface reflection in both (a) and (b).

The similarity between the Ag/Ge(111) and Ag/Si(111) surfaces extends to the energies for adsorption (E_a), binding (E_b), and diffusion (E_d) processes on top of the ($\sqrt{3}x\sqrt{3}$) layers for both systems, with (E_d+3E_b) in the range of 0.55 eV - 0.60 eV (Venables, Metcalfe, and Sugawara 1997). (The theoretical nucleation density on a perfect surface is proportional to exp(E/kT), where E for Ag on Ge(111) and Si(111) is $E=E_d+3E_b$).

Both Suliga and Henzler (1983) and Metcalfe and Venables (1996) note an instability of the ($\sqrt{3}x\sqrt{3}$) layer upon annealing at 350° C. Metcalfe and Venables (1996) observe patches of ($\sqrt{3}x\sqrt{3}$) areas which, during annealing (even if the overall patch width increases), split into two regions: an inner region corresponding to the ($\sqrt{3}x\sqrt{3}$) structure, and an outer region of a lower coverage, corresponding to the (4x4) structure. This effect is coupled with a rapid diffusion of Ag atoms over the (4x4) structure. The activation energies for the spreading of the ($\sqrt{3}x\sqrt{3}$) and the (4x4) phases were estimated as 0.78 eV and 0.87 eV, respectively.

The proposed phase diagram for the Ag/Ge(111) system in the submonolayer regime is shown in Figure 6.5. As previously mentioned, the dashed curves represent potential phase boundaries which have not been derived from energy parameters. They are drawn to accommodate the experimental reports. The curves show first-order, reversible transitions between the surface phases. Single symbols represent a reported surface completely covered by one surface structure. Overlapping symbols show the presence on the surface of several structures at the same time.

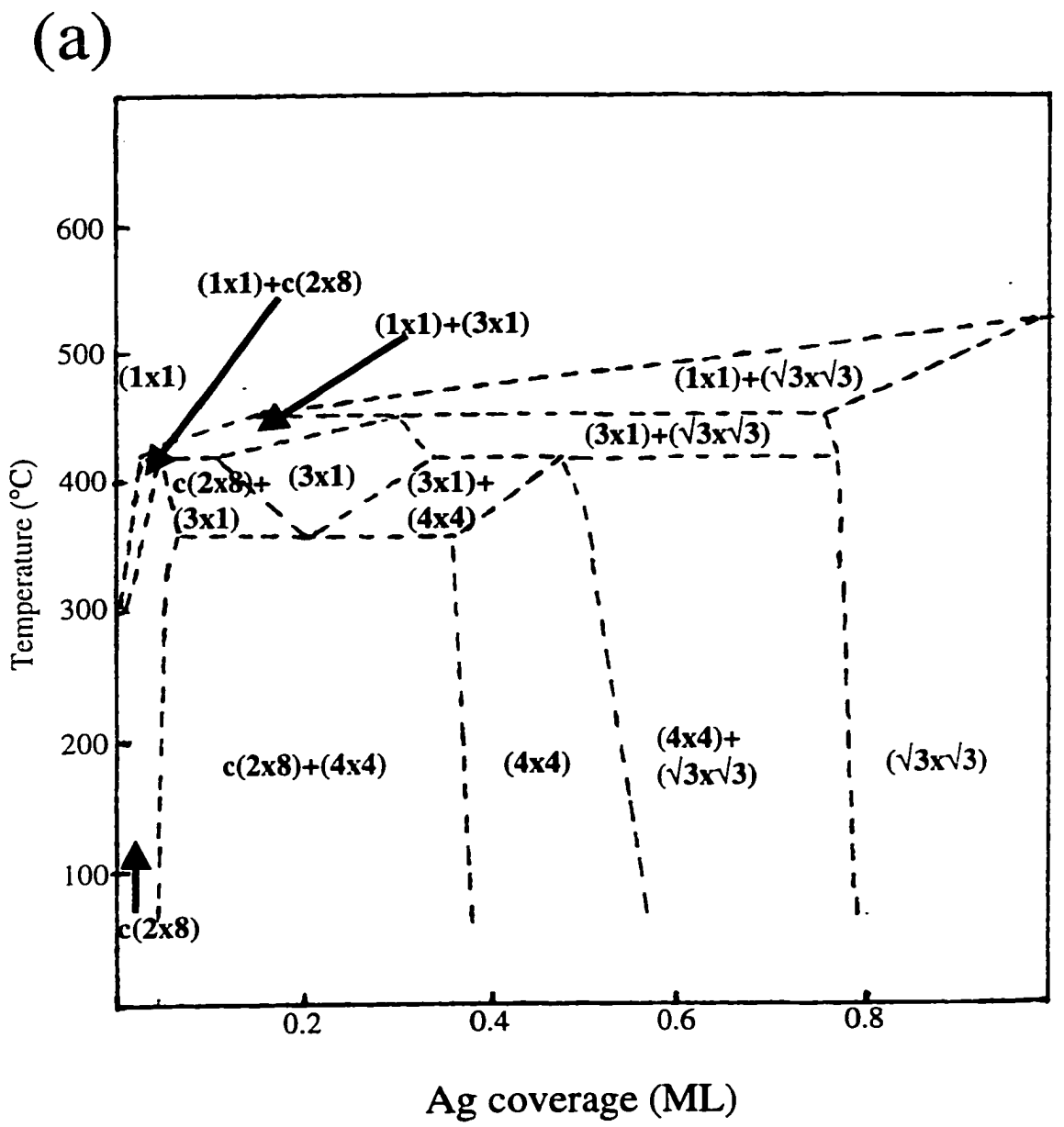

Figure 6.5. a) Proposed surface phase diagram for the Ag/Ge(111) system in the submonolayer regime, and b) The phase diagram with experimental data points. The number above a data point corresponds to its reference as follows: 1 = Spence and Tear 1998; 2 = Grozea, Bengu et al. 1999; 3 = Collazo-Davila et al. 1998; 4 = Weitering and Carpinelli 1997; 5 = Göthelid et al. 1995; 6 = Hammar et al. 1993; 7 = Metcalfe and Venables 1996; 8 = Huang et al. 1994; 9 = Dornisch et al. 1992; 10 = Busch and Henzler 1990; 11 = Fan and Ignatiev 1989; 12 = Knapp et al. 1989; 13 = Suliga and Henzler 1983; 14 = Bertucci et al. 1979; 15 = Phaneuf and Webb 1985.

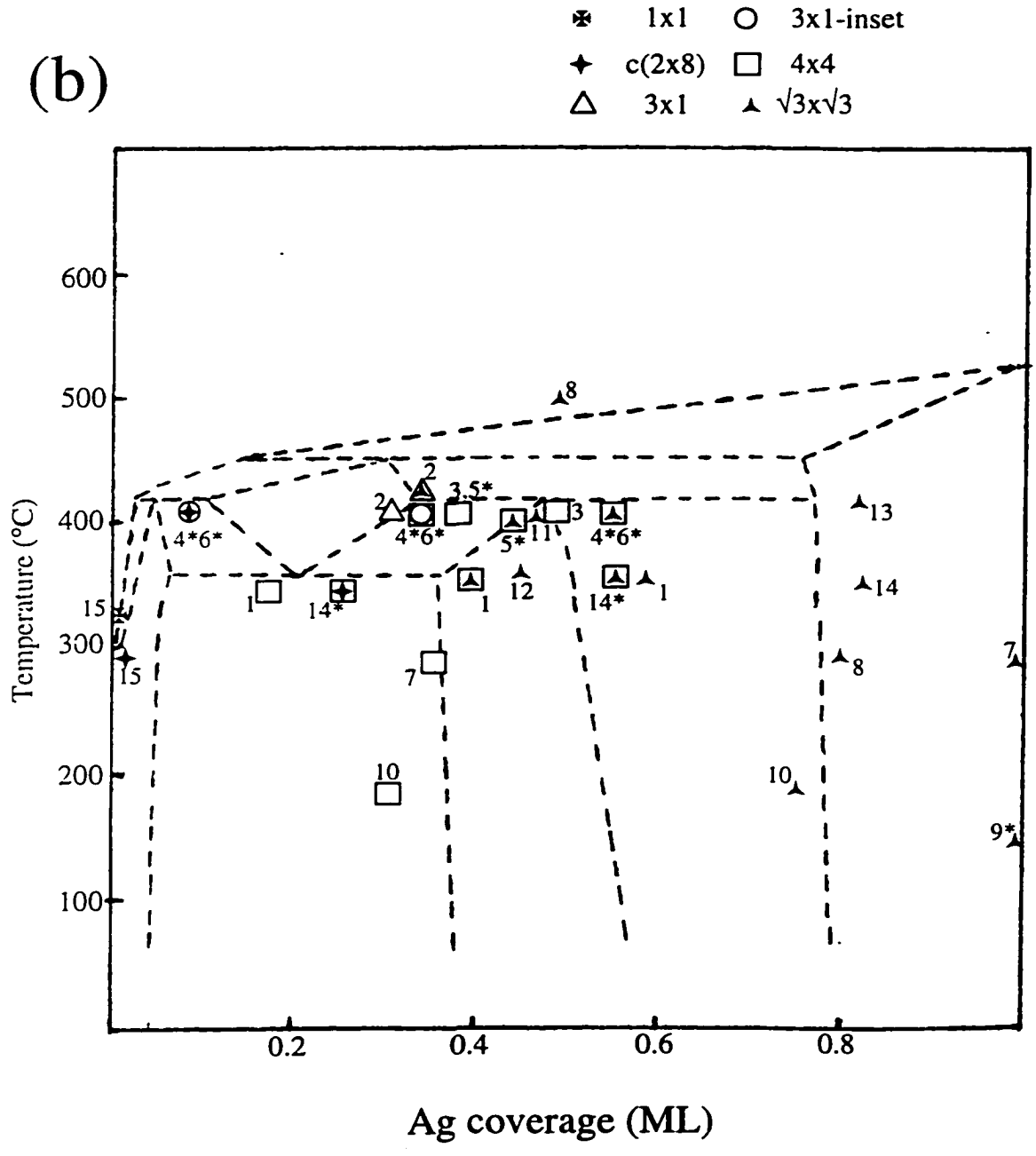

Figure 6.5. Continued.

The existence of the peritectoid region at very low Ag coverages can be inferred from the reversible transition from the c(2x8) phase to a (1x1) phase at 300° C (Phaneuf and Webb 1985), coupled with observations of the c(2x8) and the (4x4) phase occurring simultaneously on the surface at 350° C (Bertucci et al. 1979 - one of the only studies which made observations at the phase formation temperature, 350° C) or with small insets of the (3x1) phase separating c(2x8) domains and the (4x4) domains at 350° C (Spence and Tear 1998) and 400° C (Hammar et al. 1993; Weitering and Carpinelli 1997). No traces of Ag were observed on the c(2x8) terraces, and at no point was the c(2x8) phase observed to coexist with the ($\sqrt{3}$x$\sqrt{3}$) structure (Hammar et al. 1993; Weitering and Carpinelli 1997).

The (3x1) phase observations can be separated in two categories. Only one study (Grozea, Bengu et al. 1999) reported its presence over large area of the surface, and, in another experiment, coexisting with the ($\sqrt{3}$x$\sqrt{3}$) phase. The second type of observation includes the small insets of the (3x1) surface, and it is shown using a different symbol. In addition to being observed bordering c(2x8) and (4x4) domains, the (3x1) was also reported as separating large (4x4) domains (Hammar et al. 1993). The narrow temperature range over which the (3x1) structure covers large areas of the surface reflects the fact that only one study was able to match the necessary observation conditions. The experimental data suggest that the c(2x8), (3x1), and (4x4) phases may be related by an eutectoid region; the position of the eutectoid point was arbitrary selected.

Figure 6.6 shows a T-T-T curve representation of the disordered (4x4) phase, a structure quenched from the (4x4) surface, at an estimated coverage of 0.6 ML. Because

it has never been reported before, it can be assumed that the time span required to generate it is short. After repeating the thermal treatment, the surface reverted to a regular (4x4) structure.

As the next step, more experiments are needed to confirm some of the phase boundaries assumed in this preliminary phase diagram, as well as the presence and position of the eutectoid/peritectoid points.

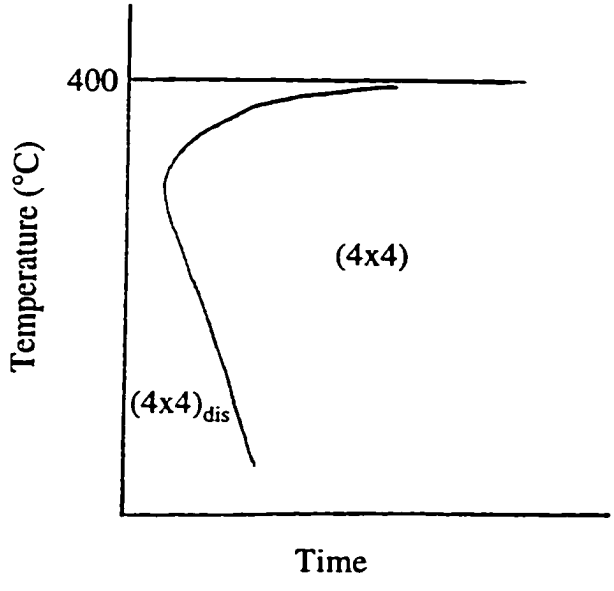

Figure 6.6. Proposed T-T-T curve representation of the transformation from a (4x4) disordered structure to the (4x4) ordered phase, at an estimated coverage of around 0.6 ML.

6.3 The Au/Si(111) system

The groundwork for extending the phase diagram of the Au/Si(111) system to the supermonolayer regime (up to 1.5 ML) has been laid out by the work of Plass (1996). Figure 6.1 shows all the results pertaining to this problem. The experimental observations mapped in the figure will be used as the basis of this study. Plass did not attempt to extend his phase diagram representation to the supermonolayer regime since crucial pieces of information, particularly the atomic geometry of the $\beta(\sqrt{3}x\sqrt{3})$ and (6x6) phases and the relationships between them, were not available.

The Au/Si(111) supermonolayer interfaces are reported to be reconstructed into $\alpha(\sqrt{3}x\sqrt{3})$, $\beta(\sqrt{3}x\sqrt{3})$, and (6x6) structures, depending on the annealing conditions and the amount of Au deposited. In addition, the picture is complicated by the presence of small Au particles that nucleate and grow at various temperatures. They were reported (Święch, Bauer, and Mundschau 1991) to occur even before the (6x6) structure formation and continue to appear in parallel with that reconstruction. The small particles were also observed at higher temperatures on the same surface with the $\beta(\sqrt{3}x\sqrt{3})$ structure (our own experiments and Święch, Bauer, and Mundschau 1991).

The atomic structure of the $\alpha(\sqrt{3}x\sqrt{3})$ phase, which occurs up to 0.95-1.0 ML, consists of sets of Au and Si trimers in the top two layers, forming a missing top layer twisted trimer structure (Plass and Marks 1995). Okuda, Daimon et al. (1997) reported SCLS data showing a spectral dissimilarity between the $\alpha(\sqrt{3}x\sqrt{3})$ and the $\beta(\sqrt{3}x\sqrt{3})$ structures and a strong resemblance between $\beta(\sqrt{3}x\sqrt{3})$ and (6x6) phases. Based on these results it can be said that the chemical environments of topmost Si atoms of the $\alpha(\sqrt{3}x\sqrt{3})$

and $\beta(\sqrt{3}x\sqrt{3})$ differ from each other and that a distinction between these two surfaces is necessary. In agreement with STM observations (Nogami, Baski, and Quate 1990), Okuda's ARPES measurements are consistent with a smaller density of the domain walls on the $\alpha(\sqrt{3}x\sqrt{3})$ surface than on the $\beta(\sqrt{3}x\sqrt{3})$ and (6x6) surfaces, which again look similar.

The structure modeling of the (6x6) phase and its disordered form, $\beta(\sqrt{3}x\sqrt{3})$, were the subject of Chapter 4 (Grozea et al. 1998; Marks, Grozea et al. 1998). Briefly, the atomic arrangement on the (6x6) surface can be described as microdomains of the parent $(\sqrt{3}x\sqrt{3})$ Au structure. A better description is in terms of a tiling of incomplete pentagonal and trimer units, essentially a pseudo-pentagonal glass. The possibility of varying its content from 1.2 ML to 1.5 ML (by completing the pentagons and by filling the centers of the B-type rings – as described in detail in Section 4.5) denotes it as a surface solution.

The $\beta(\sqrt{3}x\sqrt{3})$ and the (6x6) phases are formed at the same Au coverage. The $\beta(\sqrt{3}x\sqrt{3})$ structure corresponds to a glass-like tiling using A and B ring structures sitting at $(\sqrt{3}x\sqrt{3})$ lattice sites and giving a diffraction pattern with sharp spots surrounded by ring-like features (Figure 4.7). Because the movement of the A and B units is expected to be very slow compared to that of single atoms, it is understandable that the transition between $\beta(\sqrt{3}x\sqrt{3})$ and (6x6) surfaces behaves like a glass transition in requiring low temperature annealing and large mass transport for the formation of the 'crystalline' phase.

The proposed phase diagram extension from 1.0 ML to 1.5 ML for the Au/Si(111) system is shown in Figure 6.7, with the same considerations mentioned for Figure 6.1, and Figure 6.5. An eutectoid point, arbitrarily chosen, seems to exist between the $\beta(\sqrt{3}x\sqrt{3})$ phase, the 3D particles region, and the high-temperature phase. More experiments are necessary to configure the high-temperature 'uncharted territory' and define the phase boundaries for regions such as $\alpha(\sqrt{3}x\sqrt{3})+(1x1)$ and $\beta(\sqrt{3}x\sqrt{3})+(1x1)$.

There are a number of alloy systems, such as Cu-Au, which display a similar behavior as the order-disorder transformation observed between the (6x6) and $\beta(\sqrt{3}x\sqrt{3})$ phases. A disordered phase is present above a certain temperature and is transformed to an ordered phase when it reaches equilibrium at lower temperatures. Since the change takes place by diffusion, the rapid cooling of the system can suppress the transformation. However, the reverse change, from the ordered phase to the disordered one, cannot be avoided. By analogy with the Cu-Au system where an ordered phase forms from the disordered phase through a congruent transformation at the stoichiometric composition and with an eutectoid transformation at the Au-rich side, a similar transition is proposed from the $\beta(\sqrt{3}x\sqrt{3})$ phase to the (6x6) phase. The rate of the ordering reaction follows a T-T-T curve, shown in Figure 6.8. The exact start and finish positions are yet to be determined, but the figure qualitatively explains the experimental data and the transformation analysis very well.

During the investigation of the surface phases it resulted that they seem to obey the same general principles of physical metallurgy as their bulk counterparts. Thus, the use of T-T-T curves to explain kinetically constrained phases adds to this beneficial

analogy. It could now be possible to predict the effects of changing certain parameters, such as temperature or metal coverage, on the atomic arrangement at the surface.

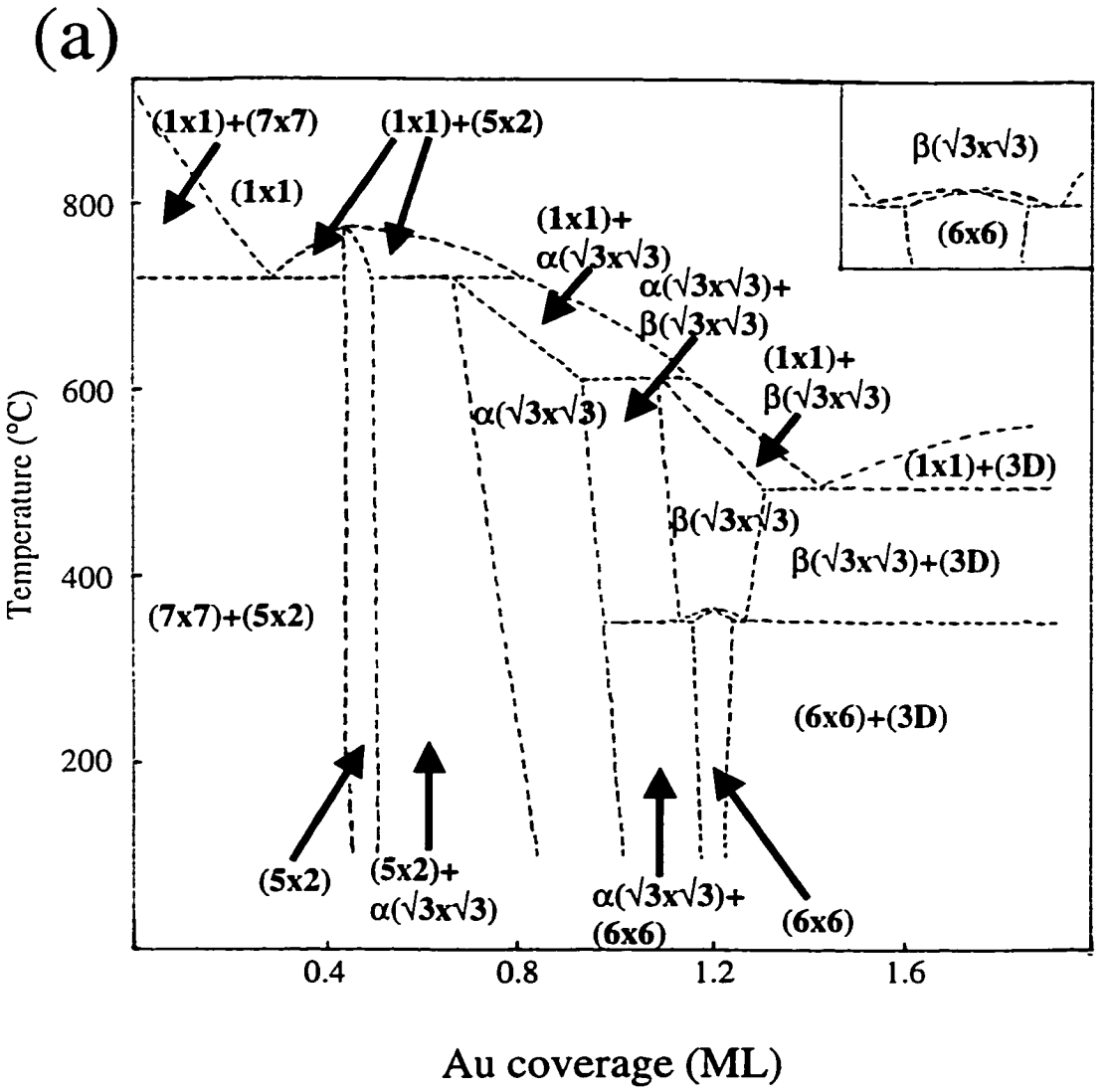

Figure 6.7. a) Proposed phase diagram extension to the supermonolayer regime for the Au/Si(111) system, and b) The phase diagram with experimental data points, limited from 0.5 to 1.5 ML, from Figure 6.1. Inset: a magnified view of the region where the order-disorder transformation occurs.

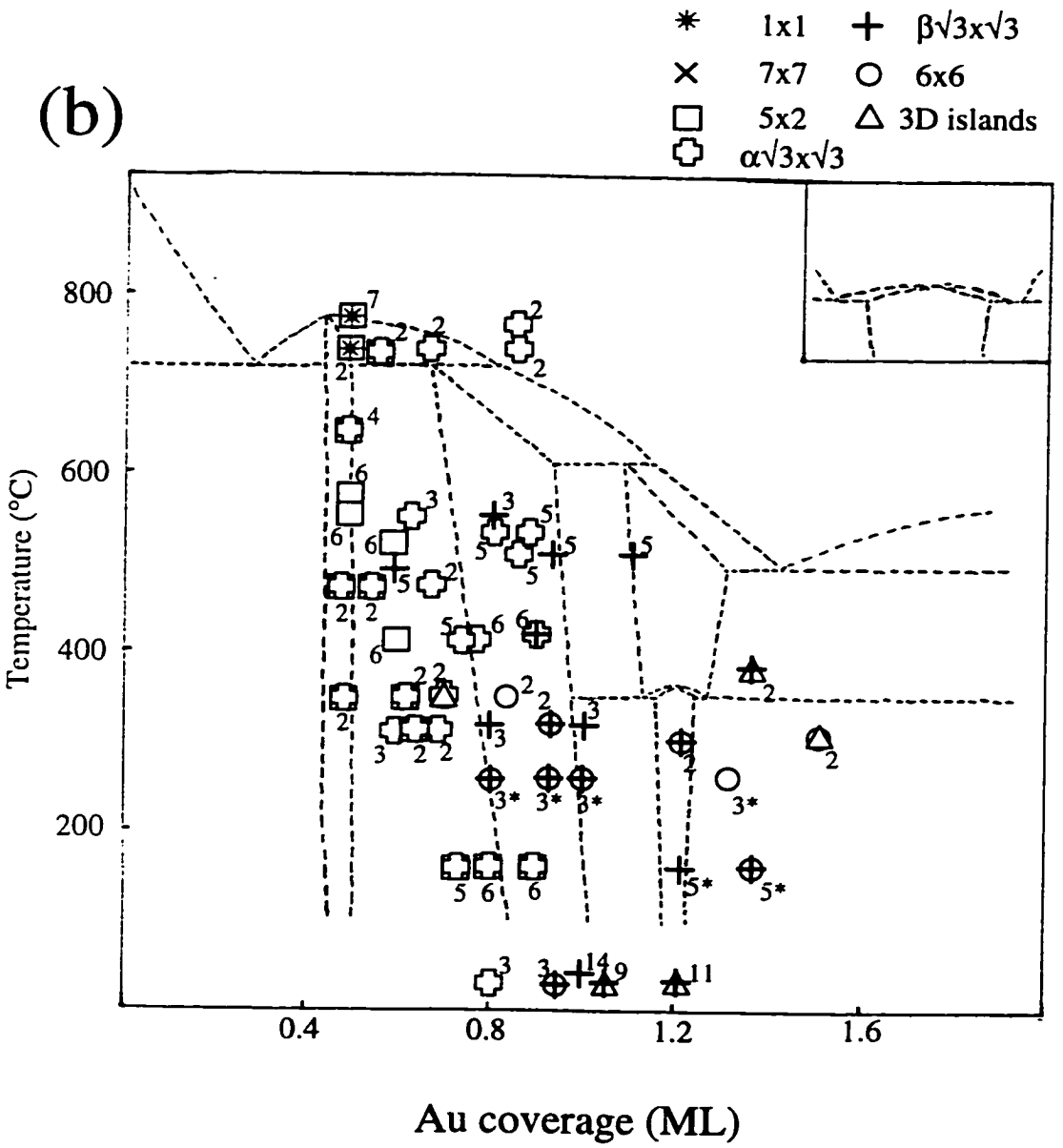

Figure 6.7. Continued.

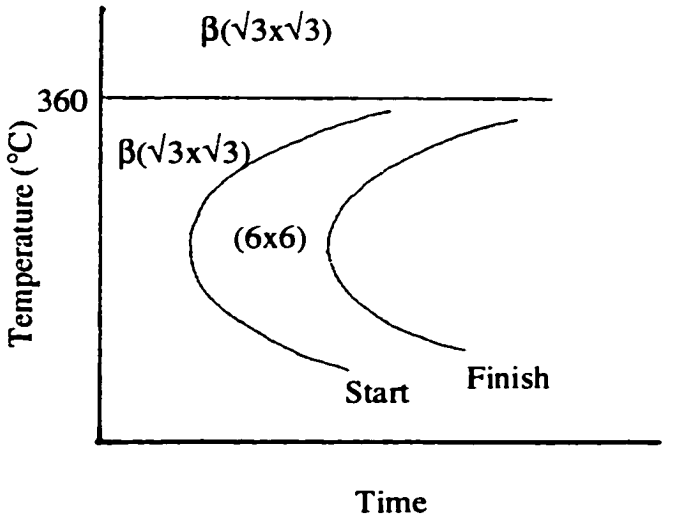

Figure 6.8. Proposed T-T-T curve representation of the transformation from β(√3x√3) phase to the (6x6) phase.

CHAPTER 7:

FUTURE WORK

The investigation of the electronic properties and atomic geometry of reconstructed surfaces is one of the major subjects of the surface science. Among various reconstructed surfaces, the noble metal/semiconductor interfaces have been studied intensively from an industrial and scientific point of view.

To precisely control epitaxy and size, leading to fabrication of novel nanometric devices, it has become necessary to investigate the correlation between atomic scale structures and their macroscopic properties. Interesting applications of the reconstructions, such as atomic scale fast switches or atomic size memories, have been suggested. Kempa, Broido, and Weitering (1997) envisioned an application of the Si(111)-(3x1)Ag surface for ultrafast computing, based on STM images displaying flipping of the semiconductor chains in the (3x1) domains due to STM tip-surface interaction.

The present thesis contributes to the general knowledge about these extremely interesting surface structures. They were investigated from the standpoint of their atomic

arrangements and links to the other related structures. At the same time, the study continued the exploration of a fresh direction by incorporating the wealth of information about surface phases into the concept of surface phase diagrams.

During this work, new atomic scale characterization tools were employed. The experimental measurements were performed using a unique system equipped with a battery of surface science techniques. Direct Methods for surfaces approach, a powerful analytical technique, allowed for pushing well beyond the current limits of surface structure modeling.

As is often the case, this thesis is a work in progress. It would be interesting to chart the supermonolayer region of the Ag/Ge(111) system and extend the phase diagram to that regime. The ($\sqrt{3}$x$\sqrt{3}$) reconstruction transforms to an almost unknown (6x6) phase when more Ag is deposited on that surface in a wide coverage range at room temperature. A reverse transformation from the (6x6) to ($\sqrt{3}$x$\sqrt{3}$) phase occurs upon annealing. Elucidating the atomic geometry and gathering more data about this reconstruction will permit a better understanding of the evolution the Ag/Ge(111) system from the submonolayer regime to higher Ag coverages. It will also allow for comparison with a similar surface solution, the Si(111)-(6x6)Au.

The use of a heating stage inside the transmission electron microscope opens another direction in the mapping of surface phase diagrams. This device would allow for real-time in situ investigation of previously unexplored portions of the phase diagrams. The first heating stage model currently in use provided an insight into design limitations of such as device; in order to perform better dynamic observations of metal-

semiconductor interfaces, the new version must offer a precise control of the annealing temperature and limit its outgassing.

The use of the new gas reaction cell which will be added to SPEAR would greatly aid in extending the investigation of reconstructions under reactive environments as well as the role of chemisorption.

The development of nanoscale devices has not yet reached a large scale and many fundamental issues remain to be solved before practical applications are made possible. Altogether, the results described in this study may play a role in the fast-growing world of nanoelectronics.

REFERENCES

An, K. S., R. J. Park, J.S. Kim, C. Y. Park, C. Y. Kim, J. W. Chung, T. Abukawa, S. Kono, T. Kinoshita, A. Kakizaki, and T. Ishii. 1995. Mg-induced Si(111)3x1 structure studied by photoelectron spectroscopy. *Surf. Sci.* 337:L789-L794.

Barrett, C. R., W. D. Nix, and A. S. Tetelman. 1973. *The principles of engineering materials*. Prentice-Hall, Inc., Englewood Cliffs, New Jersey.

Baumann, F. H. and W. Schröter. 1991. Precipitation of gold into metastable gold silicide in silicon. *Phys. Rev. B* 43:6510-6519.

Becker, G. E. and J. C. Bean. 1977. Acceptor dopants in silicon molecular-beam epitaxy. *J. Appl. Phys.* 48:3395-3399.

Bengu, E., C. Collazo-Davila, D. Grozea, E. Landree, I. Widlow, M. Guruz, and L. D. Marks. 1998. In situ growth and characterization of ultrahard thin films. *Micros. Res. Tech.* 42:295-301.

Bengu, E., R. Plass, L. D. Marks, T. Ichihashi, P. M. Ajayan, and S. Iijima. 1996. Imaging the dimers in Si(111)-(7x7). *Phys. Rev. Lett.* 77:4226-4228.

Berman, L. E., B. W. Batterman, and J. M. Blakely. 1988. Structure of submonolayer gold on silicon (111) from x-ray standing-wave triangulation. *Phys. Rev. B* 38:5397-5405.

Bertucci, M., G. Le Lay, M. Manneville, and R. Kern. 1979. Desorption kinetics of condensed phases. *Surf. Sci.* 85:471-492.

Bevington, P. R. 1969. *Data reduction and error analysis for the physical sciences.* McGraw-Hill, New York.

Binning, G. and H. Rohrer. 1987. Scanning Tunneling Microscopy – from birth to adolescence. *Rev. Mod. Phys.* 59:615-627.

Boishin, G., M. Tikhov, and L. Surnev. 1991. Na-promoted oxidation of Si(111). *Surf. Sci.* 257:190-198.

Boland, J. J. 1990. Structure of the H-saturated Si(100) surface. *Phys. Rev. Lett.* 65:3325-3328.

Bonevich, J. E. and L. D. Marks. 1992. Ultahigh vacuum electron microscopy of crystalline surfaces. *Microscopy: the Key Research Tool* 22:95-102.

Braicovich, L., C. M. Garner, P. R. Skeath, C. Y. Su, P. W. Chye, I. Lindau, and W. E. Spicer. 1979. Photoemission studies of the silicon-gold interface. *Phys. Rev. B* 20:5131-5141.

Busch, H. and M. Henzler. 1990. Domain-growth kinetics of Ag on Ge(111). *Phys. Rev. B* 41:4891-4896.

Carrière, B., J. P. Deville, and A. El Maachi. 1986. Ion-beam-induced amorphization of silicon surfaces: role on the formation of Au/Si(100) interfaces. *Surf. Sci.* 168:149-157.

Carpinelli, J. M. and H. H. Weitering. 1995. Scanning tunneling microscopy study of the metal-induced Si(111)3x1 reconstruction: evidence for dimerized chain formation. *Surf. Sci.* 331-333:1015-1021.

Carpinelli, J. M. and H. H. Weitering. 1996. Low-temperature reconstruction pathway to the Si(111)($\sqrt{3}$x$\sqrt{3}$)R30°-Ag interface. *Phys. Rev. B* 53:12651-12654.

Collazo-Davila, C., D. Grozea, E. Landree, and L. D. Marks. 1997. Transmission electron diffraction determination of the Ge(001)-(2x1) surface structure. *Surf. Sci.* 375:293-301.

Collazo-Davila, C., D. Grozea, and L. D. Marks. 1998. Determination and refinement of the Ag/Si(111)-(3x1) surface structure. *Phys. Rev. Lett.* 80:1678-1681.

Collazo-Davila, C., D. Grozea, L. D. Marks, R. Feidenhans'l, M. Nielsen, L. Seehofer, L. Lottermoser, G. Falkenberg, R. L. Johnson, M. Gothelid, and U. Karlsson. 1998. Direct Methods solution of the Ge(111)-(4x4)Ag surface. *Surf. Sci.* 418:395-406.

Collazo-Davila, C., L. D. Marks, K. Nishii, and Y. Tanishiro. 1997. Atomic structure of the In on Si(111)(4x1) surface. *Surf. Rev. Lett.* 4:65-70.

Crescenzi, M. De and M. N. Piancastelli. 1996. *Electron scattering and related spectroscopies*. World Scientific, New Jersey.

Cros, A. and P. Muret. 1992. Properties of noble-metal silicon junctions. *Mater. Sci. Rep.* 8:271-367.

Daimon, H., C. Chung, S. Ino, and Y. Watanabe. 1990. A study of Si(111)5x2-Au structures by Li adsorption and their coadsorbed superstructures. *Surf. Sci.* 235:142-155.

Daimon, H., and S. Ino. 1985. Study of the Si(111)7x7 surface structure by alkali-metal adsorption. *Surf. Sci.* 164:320-326.

Dallaporta, H. and A. Cros. 1986. Atomic bonding at the Si-Au and Si-Cu interfaces. *Surf. Sci.* 178:64-69.

Doraiswami, N., G. Jayaram, and L. D. Marks. 1995. Unusual island structures in Ag growth on Si(100)-(2x1). *Phys. Rev. B* 51:10167-10170.

Dornisch, D., W. Moritz, H. Schulz, R. Feidenhans'l, M. Nielsen, F. Grey, and R. L. Johnson. 1991. Au/Si(111): Analysis of the ($\sqrt{3}$x$\sqrt{3}$)R30° and 6x6 structures by in-plane x-ray diffraction. *Phys. Rev. B* 44:11221-11230.

Dornisch, D., W. Moritz, H. Schulz, R. Feidenhans'l, M. Nielsen, F. Grey, R. L. Johnson, and G. Le Lay. 1992. Ag on Ge(111): 2D X-ray structure analysis of the $\sqrt{3}$x$\sqrt{3}$ superstructure. *Surf. Sci.* 274:215-221.

Dorset, D. L. 1995. *Structural electron crystallography*. Plenum Press, New York.

Edwards, K. A., P. B. Howes, J. E. Macdonald, T. Hibma, T. Bootsma, M. A. James. 1996. The growth and atomic structure of the Si(111)7x7-Pb buried interface. *Physica B* 221:201-204.

Erwin, S. C. 1995. New structural model for the alkali-induced Si(111)-(3x1) reconstruction from first principles. *Phys. Rev. Lett.* 75:1973-1976.

Erwin, S. C. and H. H. Weitering. 1998. Theory of the "Honeycomb Chain-Channel" reconstruction of M/ Si(111)-(3x1). *Phys. Rev. Lett.* 81:2296-2299.

Falta, J., A. Hille, D. Novikov, G. Materlik, L. Seehofer, G. Falkenberg, and R. L. Johnson. 1995. Domain wall structure of Si(111)($\sqrt{3}$x$\sqrt{3}$)R30°-Au. *Surf. Sci.* 330:L673-L677.

Fan, W. C. and A. Ignatiev. 1989. Reconstruction of the clean and metal-adsorbed Ge(111) surface. *Phys. Rev. B* 40:5479-5483.

Fan, W. C. and A. Ignatiev. 1990. Metal-adsorbate-induced Si(111)-(1x3) reconstruction. *Phys. Rev. B* 41:3592-3595.

Frankl, D. R. and J. A. Venables. 1970. Nucleation on substrates from the vapour phase. *Advan. Phys.* 19:409-456.

Fuchigami, K. and A. Ichimiya. 1996. Gold deposition on a Si(111)$\sqrt{3}$x$\sqrt{3}$-Au surface. *Surf. Sci.* 357-358:937-942.

Fujita, D., M. Schleberger, and S. Tougaard. 1996. Extraction of depth distributions of electron-excited Auger electrons in Fe, Ni, and Si using inelastic peak shape analysis. *Surf. Sci.* 357-358:180-185.

Fukuda, T. 1994. Determination of silver coverage on Si(111)3x1(6x1)-Ag surfaces. *Phys. Rev. B* 50:1969-1972.

Gao, Q. Z., T. Hariu, and S. Ono. 1987. Low-temperature surface cleaning of Si and succesive plasma-assisted epitaxial growth of GaAs. *Jpn. J. Appl. Phys.* 26:L1576-L1578.

Giacovazzo, C. 1980. *Direct Methods in crystallography*. Plenum Press, New York.

Gilmore, C. J., L. D. Marks, D. Grozea, C. Collazo-Davila, E. Landree, and R. D. Twesten. 1997. Direct solutions of the Si(111) 7x7 structure. *Surf. Sci.* 381:77-91.

Goldberg, D. E. 1989. *Genetic algorithms in search, optimization, and machine language*. Addison-Wesley Publishing Company, Inc., New York.

Göthelid, M., M. Hammar, U. O. Karlsson, C. Wigren, and G. Le Lay. 1995. Structural and electronic evolution on the Ge(111)-Ag surface. *Phys. Rev. B* 52:14104-14110.

Green, A. K. and E. Bauer. 1976. Formation, structure, and orientation of gold silicide on gold surfaces. *J. Appl. Phys.* 47:1284-1291.

Grozea, D., E. Bengu, C. Collazo-Davila, and L. D. Marks. 1999. Structure determination of the Ge(111)-(3x1)Ag surface reconstruction. *Surf. Rev. Lett.* in press.

Grozea, D., E. Landree, C. Collazo-Davila, E. Bengu, R. Plass, and L. D. Marks. 1999. Structural investigations of metal-semiconductor surfaces. *Micron* 30:41-49.

Grozea, D., E. Landree, and L. D. Marks. 1997. Surface roughening by electron beam heating. *Appl. Phys. Lett.* 71:2301-2303.

Grozea, D., E. Landree, L. D. Marks, R. Feidenhans'l, M. Nielsen, and R. L. Johnson. 1998. Direct Methods determination of the Si(111)-(6x6)Au surface structure. *Surf. Sci.* 418:32-45.

Hammar, M., M. Göthelid, U. O. Karlsson, and S. A. Flodström. 1993. Initial growth of silver on Ge(111) studied by scanning tunneling microscopy. *Phys. Rev. B* 47:15669-15674.

Hanbücken, M. and G. Le Lay. 1986. Formation of noble-metal-Si(100) interfaces. *Surf. Sci.* 168:122-132.

Hasegawa, S., M. Maruyama, Y. Hirata, D. Abe, and H. Nakashima. 1998. New model for Si(111)-(3x1)Li through determination of its surface Si atom density with the use of scanning tunneling microscopy. *Surf. Sci.* 405:L503-L508.

Hasegawa, T., S. Hosaka, and S. Hosoki. 1992. In-situ observation of gold adsorption onto Si(111) 7x7 surface by scanning tunneling microscopy. *Jpn. J. Appl. Phys.* 31:L1492-L1494.

Hasegawa, T., S. Hosaka, and S. Hosoki. 1996. Domain growth of Si(111)-5x2 Au by high temperature STM. *Surf. Sci.* 358:858-862.

Hasegawa, T., K. Takata, S. Hosaka, and S. Hosoki. 1991. Initial stage of Au adsorption onto a Si(111) surface studied by scanning tunneling microscopy. *J. Vac. Sci. Technol. B* 9:758-761.

Hashizume, T., M. Katayama, D.-R. Jeon, M. Aono, and T. Sakurai. 1993. The absolute coverage of K on the Si(111)-3x1-K surface. *Jpn. J. Appl. Phys.* 32:L1263-L1265.

Heinemann, K. and H. Poppa. 1986. An ultrahigh vacuum multipurpose specimen chamber with sample introduction system for *in situ* transmission electron microscopy investigations. *J. Vac. Sci. Technol. A* 4;127-137.

Henzler, M. 1996. Growth of epitaxial monolayers. *Surf. Sci.* 357-358:809-819.

Higashiyama, K., S. Kono, and T. Sagawa. 1986. Structural disorder of Si(111)$\sqrt{3}$x$\sqrt{3}$-Au surface studied by LEED. *Jpn. J. Appl. Phys.* 25:L117-L120.

Himpsel, F. J., B. S. Meyerson, F. R. McFreely, J. F. Morar, A. Taleb-Ibrahimi, and J. A. Yarmoff. 1989. *Photoemission and Absorption Spectroscopy of Solids and Interfaces.* Proceedings of the International School of Physics Enrico Fermi Course(CVII), edited by M. Campagna and L. Rosei. North-Holland, Amsterdam, p. 203.

Hiraki, A. and M. Iwami. 1974. Electronic structure of thin gold film deposited on silicon substrate studied by Auger electron and x-ray photoelectron spectroscopies. *Jpn. J. Appl. Phys. Suppl.* 2:749-752.

Holland, J. H. 1975. *Adaptation in natural and artificial systems.* University of Michigan Press, Ann Arbor.

Hricovini, K., J. E. Bonnet, B. Carrière, J. P. Deville, M. Hanbücken, and G. Le Lay. 1989. Photoelectron spectroscopy studies of the formation of the Au-Si(100) interface using synchrotron radiation. *Surf. Sci.* 211/212:630-636.

Hu, C. 1999. Silicon nanoelectronics for the 21th century. *Nanotechnology* 10:113-116.

Huang, H., H. Over, S. Y. Tong, J. Quinn, and F. Jona. 1994. Atomic geometry of Ge(111)$\sqrt{3}$x$\sqrt{3}$R30°-Ag determined by low-energy electron diffraction. *Phys. Rev. B* 49:13483-13487.

Huang, J. H. and R. S. Williams. 1988. Surface-strucutre analysis of Au overlayers on Si by impact-collision ion-scattering spectroscopy: $\sqrt{3}$x$\sqrt{3}$ and 6x6 Si(111)/Au. *Phys. Rev. B* 38:4022-4032.

Ichikawa, M. and T. Doi. 1990. Observation of electromigration effect upon Si-MBE growth on Si(001) surface. *Vacuum* 41:933-937.

Ichimiya, A., H. Nomura, Y. Ito, and H. Iwashige. 1995. Gold growth on Si(111)$\sqrt{3}$x$\sqrt{3}$Ag and $\sqrt{3}$x$\sqrt{3}$Au surfaces. *J. Cryst. Growth* 150:1169-1174.

Ishii, M. and Y. Taga. 1994. Time-of-Flight scattering and recoiling spectrometry study of plasma-cleaned silicon surface. *Jpn. J. Appl. Phys.* 33:4186-4190.

Ishikawa, T., N. Tanaka, M. Lopez, and I. Matsuyama. 1996. Effects of GaAs-surface roughness on the electron-beam patterning characteristics of a surface-oxide layer. *Jpn. J. Appl. Phys.* 35:L619-L622.

Ishizaka, A. and Y. Shiraki. 1986. Low temperature surface cleaning of silicon and its application to silicon MBE. *J. Electrochem. Soc.* 133:666-671.

Iwami, M., T. Terada, H. Tokihara, M. Kubota, and Y. Murata. 1988. Alloyed interface formation in the Au-Si(111)2x1 studied by photoemission spectroscopy. *Surf. Sci.* 194:115-126.

Jayaram, G., P. Xu, and L. D. Marks. 1993. Structure of Si(100)-(2x1) surface using UHV transmission electron diffraction. *Phys. Rev. Lett.* 71:3489-3492.

Jeon, D., T. Hashizume, and T. Sakurai. 1996. Scanning tunneling microscopy of the Na/ Ge(111)3x1. *J. Phys.* IV:C5-189-194.

Jeon, D., T. Hashizume, T. Sakurai, and R. F. Willis. 1992. Structural and electronic properties of ordered single and multiple layers of Na on the Si(111) surface. *Phys. Rev. Lett.* 69:1419-1422.

Jeon, D.-R., T. Hashizume, X. Wang, C. Bai, K. Motai, and T. Sakurai. 1992. Scanning tunneling microscope study of the structural transformation of the Si(111)7x7 surface to the Na-induced 3x1 surface. *Jpn. J. Appl. Phys.* 31:L501-L504.

Jeong, S. and M.-H. Kang. 1996. Buckled reconstrcution of the alkali-metal (Na,K)-adsorbed Si(111)-(3x1) surfaces. *Phys. Rev. B* 54:8196-8201.

Jong, T. de, W. A. S. Dowma, L. Smit, V. V. Korablev, and F. W. Saris. 1983. The use of pulsed laser irradiation in silicon molecular beam epitaxy: A comparative low energy electron diffraction study. *J. Vac. Sci. Technol. B* 1:888-898.

Kahata, H. and K. Yagi. 1989. REM observation on conversion between single-domain surfaces of Si(001) 2x1 and 1x2 induced by specimen heating current. *Jpn. J. Appl. Phys.* 28:L858-L861.

Kamino, T., T. Yaguchi, M. Tomita, and H. Saka. 1996. In-situ HREM study on a surface reconstruction of Au deposited Si at very high temperature. *Phil. Mag. A* 75:105-114.

Kang, M.-H., J.-H. Kang, and S. Jeong. 1998. Spectrocopic examination of the Na/ Si(111)-(3x1) surface structure. *Phys. Rev. B* 58:R13359-R13362.

Kempa, K., D. A. Broido, and H.H. Weitering. 1997. Correlational switching between 3x1 and 6x1 surface reconstructions on Si(111) with submonolayer Ag adsorption. *Physica B* 230-232:800-802.

Khramtsova, E. A. and A. Ichimiya. 1997. Structural study of the Si(111)($\sqrt{3}$x$\sqrt{3}$)R30°-Au surface using one-beam reflection high energy electron diffraction intensity rocking curve analysis. *Jpn. J. Appl. Phys.* 36:L926-L928.

Kimura, Y. and K. Takayanagy. 1992. Freezing of the 2x1 structure of commensurate Ag(100)-Si(100) interface. *Surf. Sci.* 276:166-173.

Kleine, H., H. Bludau, H. Over, and D. Fick. 1998. The 3x1-Li to 7x7 structural transformation of Si(111) due to Li desorption. *Surf. Sci.* 410:15-20.

Klement, W. K., R. H. Willens, and P. Duwez. 1960. Non-crystalline structure in solidified gold-silicon alloys. *Nature* 187:869-870.

Knapp, B. J., J. C. Hansen, M. K. Wagner, W. D. Clendening, and J. G. Tobin. 1989. Occupied electronic structure of Au and Ag on Ge(111). *Phys. Rev. B* 40:2814-2824.

Kondo, Y., K. Ohi, Y. Ishibashi, H. Hirano, Y. Harada, K. Takayanagi, Y. Tanishiro, K. Kobayashi, and K. Yagi. 1991. Design and development of an ultrahigh vacuum high-resolution transmission electron microscope. *Ultramicroscopy* 35:111-118.

Krakow, W. 1982. The direct observation of atomic surface structure and inclined planar defects in Au (111) films. *Thin Solid Films* 93:235-253.

LaFemina, J. P. 1992. Total-energy calculations of semiconductor surface reconstrcutions. *Surf. Sci. Rep.* 16:138-248.

Lander, J. J. 1964. Chemisorption and ordered surface structures. *Surf. Sci.* 1:125-164.

Landree, E., C. Collazo-Davila, and L. D. Marks. 1997. A multi-solution genetic algorithm approach to surface structure determination using Direct Methods. *Acta Cryst. B* 53:916-922.

Landree, E., D. Grozea, C. Collazo-Davila, and L. D. Marks. 1997. UHV high-resolution electron microscopy and chemical analysis of room-temperature Au deposition on Si(001)-2x1. *Phys. Rev. B* 55:7910-7916.

Landree, E., L. D. Marks, P. Zschack, and C. J. Gilmore. 1998. Structure of the TiO_{2-x}(100)-1x3 surface by Direct Methods. *Surf. Sci.* 408:300-309.

Le Lay, G. 1981. The Au/Si(111) interface: growth mode, energetics, structural and electronic properties. *J. Cryst. Growth* 54:551-557.

Le Lay, G. 1983. Physics and electronics of the noble-metal/elemental-semiconductor interface formation: a status report. *Surf. Sci.* 132:169-204.

Le Lay, G., M. Manneville, and R. Kern. 1977. Isothermal desorption spectroscopy for the study of two-dimensional condensed phases. Investigation of the Au(deposit)/Si(111) (substrate) system; application to the Xe/(0001) graphite system. *Surf. Sci.* 65:261-276.

Le Lay, G., G. Quentel, J. P. Faurie, and A. Masson. 1976. Epitaxy of noble metals and (111) surface superstructures of silicon and germanium. Part I: study at room temperature. *Thin Solid Films* 35:273-287.

Lottermoser, L., E. Landermark, D.-M. Smilgies, M. Nielsen, R. Feidenhans'l, G. Falkenberg, R. L. Johnson, M. Gierer, A. P. Seitsonen, H. Kleine, H. Bludau, H. Over, S. K. Kim, and F. Jona. 1998. New bonding configuration on Si(111) and Ge(111) surfaces induced by the adsorption of alkali metals. *Phys. Rev. Lett.* 80:3980-3983.

Love A. E. H. 1944. *A Treatise on the Mathematical Theory of Elasticity*. Dover Publications Inc., New York, p. 172.

Lu, P. and D. J. Smith. 1991. Direct imaging of CdTe(001) surface reconstructions by high-resolution electron microscopy. *Surf. Sci.* 254:119-124.

Malis, T., S. C. Cheng, and R. F. Egerton. 1988. EELS log-ratio technique for specimen-thickness measurement in TEM. *J. Electron Micros. Tech.* 8:193-200.

Marks, L. D. 1983. Direct imaging of carbon-coated and clean gold (110) surfaces. *Phys. Rev. Lett.* 51:1000-1002.

Marks, L. D. 1996. Wiener-filter enhancement of noisy HREM images. Ultramicros. 62:43-52.

Marks, L. D. 1999. General solution for three-dimensional surface structures using direct methods. *Phys. Rev. B* 60:2771-780.

Marks, L. D., E. Bengu, C. Collazo-Davila, D. Grozea, E. Landree, C. Leslie, and W. Sinkler. 1998. Direct Methods for surfaces. *Surf. Rev. Lett.* 5:1087-1106.

Marks, L. D., D. Grozea, R. Feidenhans'l, M. Nielsen, and R. L. Johnson. 1998. Au 6x6 on Si(111): evidence for a 2D pseudoglass. *Surf. Rev. Lett.* 5:459-464.

Marks, L. D. and E. Landree. 1998. A Minimum Entropy algorithm for surface phasing problems. *Acta Cryst. A* 54:296-305.

Marks, L. D. and R. Plass. 1995. Atomic structure of Si(111)-(5x2)-Au from high resolution electron microscopy and heavy-atom holography. *Phys. Rev. Lett.* 75:2172-2175.

Marks, L. D., R. Plass, and D. Dorset. 1997. Imaging surface structures by direct phasing. *Surf. Rev. Lett.* 4:1-8.

Marks, L. D., W. Sinkler, and E. Landree. 1999. A feasible set approach to the crystallographic phase problem. *Acta Cryst. A* 55:601-612.

Marks, L. D. and D. J. Smith. 1983. Direct surface imaging in small metal particles. *Nature* 303:316-317.

Marks, L. D., P. Xu, and D. N. Dunn. 1993. UHV transmission electron microscopy of Ir(001). II Atomic positions of the (5x1) reconstructed surface from HREM and R-factor refinements. *Surf. Sci.* 294:322-332.

Mathieu, G., R. Contini, J. M. Layet, P. Mathiez, and S. Giorgio. 1988. The Au/Si(111)7x7 interface: correlation between electronic and morphological properties by high-resolution electron energy-loss spectroscopy, ultraviolet photoemission spectroscopy, and transmission electron microscopy. *J. Vac. Sci. Technol.* A 6:2904-2909.

McCartney, M. R. and D. J. Smith. 1991. Studies of electron irradiation and annealing effects on TiO_2 surfaces in ultrahigh vacuum high-resolution electron microscopy. *Surf. Sci.* 250:169-178.

Meinel, K. and D. Katzer. 1992. Modes of growth of Au films on Si(111) and the mechanism of the silicide formation. *Appl. Surf. Sci.* 56-58:514-519.

Metcalfe, F. L. and J. A. Venables. 1996. Comparisons of Ag deposits on Ge and Si(111). *Surf. Sci.* 369:99-107.

Métois, J. J., S. Nitsche, and J. C. Heyraud. 1989. An ultrahigh-vacuum transmisson and scanning electron microscope for crystal growth experiments. *Ultramicroscopy* 27:349-358.

Miki, K., Y. Morita, H. Tokumoto, T. Sato, M. Iwatsuki, M. Suzuki, and T. Fukuda. 1992. Real-time observation of the Si(111):(7x7)-(1x1) phase transition by scanning tunneling microscopy. *Ultramicroscopy* 42:851-857.

Milnes, A. G. 1973. *Deep impurities in semiconductors*. New York, Wiley.

Minoda, H., Y. Tanishiro, N. Yamamoto, and K. Yagi. 1992. Growth of Si on Au deposited Si(111) surfaces studied by UHV-REM. *Appl. Surf. Sci.* 60:107-111.

Miura, H., K. Ohtaka, and D. Shindo. 1995. Effect of electron beam irradiation on Si surface cleaning in ultrahigh-vacuum system. *Jpn. J. Appl. Phys.* 34:L573-L576.

Monch, W., P. Koke, and S. Krueger. 1981. On the electronic structure of clean, 2x1 reconstructed silicon (001) surfaces. *J. Vac. Sci. Technol.* 19:313-318.

Morrison, S. R. 1990. *The Chemical Physics of Surfaces*. 2nd ed., Plenum Press, New York, pp. 95 and 102.

Muscat, A. J., A. Rjeb, and D. Roy. 1994. Oxidation of Si(111)7x7 using alkali metal atoms: evidence for local promotion mechanisms. *Surf. Sci.* 302:L256-L262.

Nagao, T., S. Hasegawa, K. Tsuchie, S. Ino, C. Voges, G. Klos, H. Pfnür, and M. Henzler. 1998. Structural phase transitions of Si(111)-($\sqrt{3}$x$\sqrt{3}$)R30°-Au: Phase transitions in domain-wall configurations. *Phys. Rev. B* 57:10100-10109.

Nakashima, K., M. Iwami, and A. Hiraki. 1975. Low temperature diffusion of Au into Si on the Si(substrate)-Au(film) system. *Thin Solid Films* 25:423-430.

Narusawa, T., S. Komiya, and A. Hiraki. 1973. Diffuse interface in Si(substrate)-Au(evaporated film) system. *Appl. Phys. Lett.* 22:389-390.

Narusawa, T., K. Kinoshita, W. M. Gibson, and A. Hiraki. 1981. Structure study of Au-Si interface by MeV ion scattering. *J. Vac. Sci. Technol.* 18:872-875.

Nihoul, G., K. Abdelmoula, and J. J. Métois. 1984. High resolution images of a reconstructed surface structure on (111) gold platelets: interpretation and comparison with theoretical models. *Ultramicroscopy* 12:353-366.

Nogami, J., A. A. Baski, and C. F. Quate. 1990. $\sqrt{3}x\sqrt{3} \rightarrow 6x6$ phase transition on the Au/Si(111) surface. *Phys. Rev. Lett.* 65:1611-1614.

Oberli, L., R. Monot, H. J. Mathieu, D. Landolt, and J. Buttet. 1981. Auger and X-ray photoelectron spectroscopy of small Au particles. *Surf. Sci.* 106:301-307.

Okamoto, H. and T. B. Massalski. 1983. The Au-Si (gold-silicon system). *Bull. Alloy Phase Diagr.* 4:190.

Okuda, T., H. Daimon, S. Suga, Y. Tezuka, and S. Ino. 1997. Surface electronic structure of ordered alkali- and noble metal-overlayers on Si(111). *Appl. Surf. Sci.* 121/122:89-97.

Okuda, T., K. Sakamoto, H. Nishimoto, H. Daimon, S. Suga, T. Kinoshita, and A. Kakizaki. 1997. Angle-resolved photoelectron spectroscopy of the Si(111)3x1-Na surface. *Phys. Rev. B* 55:6762-6765.

Okuda, T., H. Shigeoka, H. Daimon, S. Suga, T. Kinoshita, and A. Kakizaki. 1994. Surface and bulk core level shifts of the Si(111)3x1-Na and Si(111)δ7x7-Na surfaces. *Surf. Sci.* 321:105-110.

Okuno, K., T. Ito, M. Iwami, and A. Hiraki. 1980. Presence of critical Au-film thickness for room temperature interfacial reaction between Au(film) and Si(crystal substrate). *Solid State Commun.* 34:493-497.

Oura, K. and T. Hanawa. 1979. LEED-AES study of the Au-Si(100) system. *Surf. Sci.* 82:202-214.

Oura, K., Y. Makino, and T. Hanawa. 1976. Gold-induced superstructures on Si(100) surfaces as observed by LEED-AES. *Jpn. J. Appl. Phys.* 15:737-738.

Pandey, K. C. 1981. New π-bonded chain model for Si(111)-(2x1) surface. *Phys. Rev. Lett.* 47:1913-1917.

Perfetti, P., S. Nannarone, F. Patella, C. Quaresima, A. Savoia, F. Cerrina, and M. Capozi. 1980. Energy loss spectroscopy (ELS) on the Si-Au system. *Solid State Commun.* 35:151-153.

Phaneuf, R. J. and M. B. Webb. 1985. A LEED study of Ge(111); a high temperature incommensurate structure. *Surf. Sci.* 164:167-195.

Plass, R. 1996. *Gold induced Si(111) surface reconstructions studied by ultrahigh vacuum transmission electron microscopy*. Ph. D. Thesis dissertation, Northwestern University, Illinois.

Plass, R., K. Egan, C. Collazo-Davila, D. Grozea, E. Landree, L. D. Marks, and M. Gajdardziska-Josifovska. 1998. Cyclic ozone identified in Magnesium oxide (111) surface reconstructions. *Phys. Rev. Lett.* 81:4891-4894.

Plass, R. and L. D. Marks. 1995. UHV transmission electron microscopy structure determination of the Si(111)-($\sqrt{3}$x$\sqrt{3}$)R30°Au surface. *Surf. Sci.* 342:233-249.

Plass, R. and L. D. Marks. 1997. Submonolayer Au on Si(111) phase diagram. *Surf. Sci.* 380:497-506.

Plass, R., L. D. Marks, and D. L. Dorset. 1996. Adsorption site of Au on the Si(111)-($\sqrt{3}$x$\sqrt{3}$)R30° Au surface. Unpublished.

Press, W. H., B. F. Flannery, S. A. Teukolsky, and W. T Vetterling. 1986. *Numerical Recipes.* Cambridge University Press, Cambridge, p. 539.

Quinn, J. and F. Jona. 1991. New results on the reaction of Si{111} with Mg. *Surf. Sci.* 249:L307-L311.

Rao, C. N. R., V. Vijayakrishnan, H. N. Aiyer, G. U. Kulkarni, and G. N. Subbanna. 1993. An investigation of well-characterized small gold clusters by photoelectron spectroscopy, tunneling spectroscopy, and cognate techniques. *J. Phys. Chem.* 97:11157-11160.

Robison, W., R. Sharma, and L. Eyring. 1991. Observation of gold silicon alloy formation in thin-films by high-resolution electron-microscopy. *Acta Metall. Mater.* 39:179-186.

Salvan, F., A. Cros, and J. Derrien. 1980. Electron energy loss measurements on the gold-silicon interface. *J. Phys. Lett.* 41:L337-340.

Salvan, F., H. Fuchs, A. Baratoff, and G. Binning. 1985. Au/Si(111) overlayer: characterization by tunneling microscopy and spectroscopy. *Surf. Sci.* 162:634-639.

Sakamoto, K., T. Okuda, H. Nishimoto, H. Daimon, S. Suga, T. Kinoshita, and A. Kakizaki. 1994. Photoemission study of the Si(111)3x1-K surface. *Phys. Rev. B* 50:1725-1732.

Saranin, A. A., A. V. Zotov, V. G. Lifshits, J.-T. Ryu, O. Kubo, H. Tani, T. Harada, M. Katayama, and K. Oura. 1998. Reexamination of the Si(111)3x1-Na reconstruction on the basis of Si atom density and unit cluster determiantion. *Phys. Rev. B* 58:3545-3548.

Seiwatz, R. 1964. Possible structures for clean, annealed surfaces of germanium and silicon. *Surf. Sci.* 2:473-483.

Semiconductor Industry Association. 1997. *The National Technology Roadmap for Semiconductors*. San Jose, California.

Shibata, A., Y. Kimura, and K. Takayanagi. 1992. Si(111)$\sqrt{3}$x$\sqrt{3}$-Au growing on a 7x7 surface. *Surf. Sci. Lett.* 273:L430-L434.

Shiraki, Y., Y. Katayama, K. L. I. Kobayashi, and K. F. Komatsubara. 1978. Molecular beam and solid-phase epitaxies of silicon under ultra-high vaccum. *J. Cryst. Growth* 45:287-291.

Sone, J., J. Fujita, Y. Ochiai, S. Manako, S. Matsui, E. Nomura, T. Baba, H. Kawaura, T. Sakamoto, C. D. Chen, Y. Nakamura, and J. S. Tsai. 1999. Nanofabrication toward sub – 10 nm and its application to novel devices. *Nanotechnology* 10:135-141.

Spence, D. J. and S. P. Tear. 1998. STM studies of submonolayer coverages of Ag on Ge(111). *Surf. Sci.* 398:91-104.

Stöhr, J., R. Jaeger, G. Rossi, T. Kendelewicz, and I. Lindau. 1983. Structure of the Ag on Si(111) 7x7 interface by means of surface EXAFS. *Surf. Sci.* 134:813-.

Sugiura, H. and M. Yamaguchi. 1980. Crystal defects of silicon films formed by molecular beam epitaxy. *Jpn. J. Appl. Phys.* 19:583-589.

Suliga, E. and M. Henzler. 1983. Diffusion of Ag on clean Ge(111) with different step densities. *J. Phys. C* 16:1543-1554.

Święch, W., E. Bauer, and M. Mundschau. 1991. A low-energy electron microscopy study of the sytem Si(111)-Au. *Surf. Sci.* 253:283-296.

Takahashi, S., Y. Tanishiro, and K. Takayanagi. 1991. Short range orders of an adsorbed layer: gold on the Si(111)7x7 surface. *Surf. Sci.* 242:73-80.

Takahashi, T. and S. Nakatani. 1993. Refinement of the Si(111)$\sqrt{3}$x$\sqrt{3}$-Ag structure by surface x-ray-diffraction. *Surf. Sci.* 282:17-32.

Takami, T., D. Fukushi, T. Nakayama, M. Uda, and M. Aono. 1994. Structural correlation among different phases in the initial stage of epitaxial growth of Au on Si(111). *Jpn. J. Appl. Phys.* 33:3688-3685.

Takayanagy, K., Y. Tanashiro, S. Takahashi, and M. Takahashi. 1985. Structure analysis of Si(111)-7x7 reconstructed surface by transmission electron diffraction. *Surf. Sci.* 164:367-392.

Taleb-Ibrahimi, A., C. A. Sebenne, D. Bolmont, and P. Chen. 1984. Electronic properties of cleaved Si(111) upon room-temperature deposition of Au. *Surf. Sci.* 146:229-240.

Tanishiro, Y. and K. Takayanagi. 1989. Validity of the kinematical approximation in transmission electron diffraction for the analysis of surface structures. *Ultramicroscopy* 27:1-8.

Tanuma, S., C. J. Powel, and D. R. Penn. 1991. Calculations of electron inelastic mean free paths. 2. Data for 27 elements over the 50-2000-eV range. *Surf. Interface Anal.* 17:911-926.

Tikhov, M., L. Surnev, and M. Kiskinova. 1991. Na-induced (7x7)-to-(3x1) structural transformation on a Si(111)7x7 surface and the resulting passivation of the surface towards interaction with oxygen. *Phys. Rev. B* 44:3222-3225.

Twesten, R. D., J. M. Gibson, and F. M. Ross. 1994. Visualization of dynamic near-surface processes. *MRS Bull.* 6:38-43.

Venables, J. A., F. L. Metcalfe, and A. Sugawara. 1997. Competing processes and controlling energies at the Ag/Ge(111) interface. *Surf. Sci.* 371:420-430.

Venables, J. A., G. D. T. Spiller, and M. Hanbücken. 1984. Nucleation and growth of thin films. *Rep. Prog. Phys.* 47:399-459.

Vijayakrishnan, V. and C. N. R. Rao. 1991. An investigation of transition metal clusters deposited on graphite and metal oxide substrates by a combined use of XPS, UPS and Auger spectroscopy. *Surf. Sci. Lett.* 255:L516-L522.

Wan, K. J., X. F. Lin, and J. Nogami. 1992. Comparison of the 3x1 reconstructions of the Si(111) surface induced by Li and Ag. *Phys. Rev. B* 46:13635-13638.

Wang, H., R. Liu, and X. Wang. 1987. Structural model of Si(100)-c(4x4). *Phys. Rev. B* 36:7712-7714.

Weitering, H. H. 1996. New barium-induced surface reconstruction on Si(111). *Surf. Sci.* 355:L271-L277.

Weitering, H. H. and J. M. Carpinelli. 1997. Electronic properties of the Ag/ Ge(111) interface. *Surf. Sci.* 384:240-253.

Weitering, H. H., N. J. DiNardo, R. Pérez-Sandoz, J. Chen, and E. J. Mele. 1994. Structural model for the metal-induced Si(111)3x1 reconstruction. *Phys. Rev. B* 49:16837-16840.

Weitering, H. H., X. Shi, and S. C. Erwin. 1996. Band dispersions of the π-bonded-chain reconstruction of Si(111)3x1-Li: a critical evaluation of theory and experiment. *Phys. Rev. B* 54:10585-10592.

Wilk, G. D., R. E. Martinez, J. F. Chervinsky, F. Spaepen, and J. A. Golovchenko. 1994. Low-temperature homoepitaxial growth on Si(111) mediated by thin overlayers of Au. *Appl. Phys. Lett.* 65:866-868.

Wood, E. A. 1964. Vocabulary of surface crystallography. *J. Appl. Phys.* 35:1306-1311.

Woolfson, M. M. 1987. Direct Methods – from birth to maturity. *Acta Cryst. A* 43:593-612.

Woolfson, M. M. and H.-f. Fan. 1995. *Physical and non-physical methods of solving crystal structures*. University Press, Cambridge.

Wright, S. and H. Kroemer. 1980. Reduction of oxides on silicon by heating in a gallium molecular beam at 800°C. *Appl. Phys. Lett.* 36:210-211.

Xu, P., D. N. Dunn, J. P. Zhang, and L. D. Marks. 1993. Atomic imaging of surfaces in plan view. *Surf. Sci.* 285:L479-L485.

Xu, P., G. Jayaram, and L. D. Marks. 1994. Cross-correlation method for intensity measurement of transmission electron diffraction patterns. *Ultramicroscopy* 53:15-18.

Xu, P. and L. D. Marks. 1992. Intensities of surface diffraction spots in plan view. *Ultramicroscopy* 45:155-157.

Yeh, J. –J., J. Hwang, K. Bertness, D. J. Friedman, R. Cao, and I. Lindau. 1993. Growth of the room temperature Au/ Si(111)-(7x7) interface. *Phys. Rev. Lett.* 70:3768-3771.

Yuhara, J., M. Inoue, and K. Morita. 1992a. Phase transition of the Si(111)-Au surface from $\sqrt{3}x\sqrt{3}$ to 5x1 structure studied by means of the low-energy electron diffraction, Auger electron spectroscopy, and Rutherford backscattering spectroscopy techniques. *J. Vac. Sci. Technol. A* 10:334-338.

Yuhara, J., M. Inoue, and K. Morita. 1992b. Commensurate-incommensurate phase transition between 6x6 and $\sqrt{3}x\sqrt{3}$+ satellite structures of the Au/Si(111) surface. *J. Vac. Sci. Technol. A* 10:3486-3491.

Zehner, D. M., C. W. White, and G. W. Ownby. 1980. Preparation of atomically clean silicon surfaces by pulsed laser irradiation. *Appl. Phys. Lett.* 36:56-59.

Zinsmeister, G. 1971. Theory of thin film condensation. Part D: Influence of a variable collision factor. *Thin Solid Films* 7:51-75.

APPENDIX A:

THE SPEAR DANCE

Schmidt's Law:

If you mess with a thing long enough, it will break

The term 'Spear Dance' was coined by Rich Plass, who came back from Japan and discovered how interesting things have become in using Spear and the attached Hitachi microscope. In fact, it used to be a unique UHV microscope with a small and limited surface side chamber attached to it.

Over the last few years I was one of the people who used the system extensively, therefore the following would try to give you a flavor and some informal details of what it takes to obtain one of the metal/semiconductor surface reconstructions. Which sometimes is the goal and sometimes just the beginning of the experiment.

Ex situ:

In most cases we are preparing TEM samples, hence I'll concentrate only on

them. First point: **CLEAN**, you should clean thoroughly everything, glassware, sample (get rid of all the glue residue), the Mo ring, the spring-clip. Use deionized water from the Materials Processing and Crystal Growth Facility. Do not breathe over the sample or the ring. You can use Erman's tools to put the sample into the ring and push down the spring-clip. Did I mention to wear gloves at all times?

Now, before you move to Spear, look at yourself, if you have long arms and a steady hand, you may eventually qualify (in 6 months to 1 year) as a fully trained user. If you are small, but nimble, willing to climb all over the place, and not afraid, you may also have a shot (still there will be things that only 'long hands' can do).

Before you can operate Spear, watch and learn, even open the manual. You should watch the video tapes about baking Spear and the microscope to see what kind of work it is expected from you. Try to understand what is being done, how, and why. Ask a lot of questions, you may even get some answers. Even small details are important, and neglecting them can lead to major accidents. If something gets jammed, do not force it. If force is the last option, try to secure the other parts and predict what may happen if something breaks.

In situ:

You put a sample into Spear. You have courage. But we saw people who were too afraid to go on and tried to stop after this feat. Another important rule: keep track of your sample, and do not mess with other people's samples. Treat their samples as being more important than yours.

The first thing to do (after the usual overnight bake of the load lock) is to check the sample if it is indeed a TEM sample.

Spear dance – Part one:

Check the pressure on the CC (cold-cathode), and inside the transfer chamber. Open the gate-valve to the transfer chamber, extend the transfer arm and pick up the introduction module (do not forget to apply some pressure and use your long hands), retract the arm and close the gate-valve (Did you check the pressure all the time?). Rotate the arm towards the parking module and extend the arm, but not all the way. Bring down the elevator rod, and then position the sample under it. Pick the sample up and now it becomes exciting. Put it inside one of the microscope cartridges. It is the one of the most potentially damaging operations so you have to learn it very well. Open the gate-valve to the microscope and transfer your sample inside. Do not forget to check: Objective Aperture – out, translators and tilts – zeroed, and the pressure.

If your sample is a good TEM specimen, it has to go to the analytical chamber to get cleaned.

Spear Dance – Part Two:

Open the gate-valve to the microscope and take the cartridge out (after checking: Objective Aperture – out, translators and tilts – zeroed, and the pressure). Pick up the sample with the elevator rod and put it down on the transfer arm (GaAs samples do not survive the transfer, thus there may be materials that can not be investigated using Spear). Retract the arm and rotate it, always only in the clockwise (there is an arrow) direction, towards the analytical chamber. The idea with opening all the time the gate-valves is that

it helps with getting through them. If you extend/move things slowly and gently, a nice sound will tell you that you should have opened the gate-valve; otherwise, check how many samples are still there and write on the board. Once inside the analytical chamber, pick up your sample with the grippers, and remember that gravity is working against you. Do not push the vertical manipulator higher than 7; if it breaks, lift the stage with your hand and do not let it to push against the transfer rod. An advanced user can try to get the sample with the grippers on reverse, with the result of the sample sitting higher and less shadow effects affecting your processing.

Cleaning the sample: if the sample sits high in the grippers, you will be able to use lower angles for ion milling and increase the yield. We clean both sides, each from two directions, 45°-50° and 130°. Ar ions are very effective at lower energies. The time depends on the particular sample and you can check the results using the XPS. Once there are no more contaminants on the sample surface but Ar, and a detailed scan around C, O peaks confirmed it, you can anneal the sample. The ring is annealed better resistively, while for the sample use the electron gun.

For XPS, the controls are: vertical 5.85; rotation 95° or 275°; I/O start around 4.0 – 4.2; and horizontal start around 3.7. The last two have to be centered: move the sample until you see the Mo peak (one side of the sample), then the other way again until the Mo peaks shows up again (the other side of the sample). The middle value corresponds to the center of the sample.

For resistive heating, 0.9 V/ 6A for 3 min gives you a clean ring. For the electron gun: a) Si(001)-(2x1) 740° C for 5 min, followed by 550° C for 30-45 min; b) Si(111)-

(7x7) 740° C for 5 min. For other kind of samples you have to experiment by yourself, if the temperature is too high, you can start rethinning or making a new sample, if it is too low, you do not achieve the desorption of the contaminants. Anneal usually from the spring-clip side and do your depositions on the other side of the sample. After that, the samples go back to the microscope to be checked if they are thin and their surface reconstructed.

Now is a good moment to outgass the metal deposition boat, for 2 – 3 s at a voltage higher than the one that will be used. For the determination of the deposition conditions, a different sample may be used. Put your sample on the transfer module, and please do not have any other module attached. Remember that you want to deposit only on your sample. When you extend/retract the arm towards the metal deposition stage, pay a lot of attention to the wires from the deposition boats. For deposition conditions, for example: a) Si(111)-($\sqrt{3}$x$\sqrt{3}$)-Au, deposit Au at V=2.2 V for 30 s, followed by an anneal at 610° C for 1 min (as a bonus you may even get small particles too. To clean the sample of the Au layer, ion milling with Ar ions at 1.2 kV for 1 h, followed by a resistive anneal, more ion milling, and eventually an electron beam anneal will restore the Si(111)-(7x7) surface); b) Si(111)-($\sqrt{3}$x$\sqrt{3}$)-Ag, deposit Ag at V=2.4 V for 45 s, followed by an anneal at 560° C for 4 s (annealing at 600° C for 30 s will desorb all the Ag atoms). All these values should be taken as starting points.

How do you estimate how much material was deposited? There used to be a working quartz crystal monitor. If you observe the ($\sqrt{3}$x$\sqrt{3}$) reconstruction for Au or Ag, that is corresponding to a coverage of around 1 ML, and it can be correlated with the XPS

spectra. XPS can provide useful information. Using the XPS spectra, recorded before and after the deposition, the code will give you the area under the peaks. With that data, corrected with the sensitivity factors and assuming a growth model (such as layer-by-layer), you can calculate the thickness of the deposit (see, for instance, the C80 course notes). You can also use AES, it worked a couple of times (a bold and persistent guy is needed).

Equipment maintenance

If the equipment is not working, the net result is no experiments, and no data for your thesis. Before you run to Laurie, try to give it your best shot. Call the company a lot and try to talk with a technician, not a salesman. Sending back the device takes time and money, but the worse is to have them to visit. **When you enter the laboratory, always check the pressure, and then listen to the sounds of Spear.** It is like a song, and anything different is a signal that something is or will be wrong.

Finally, to achieve that nice UHV that we are so proud of, "METAL-TO METAL", as Erman will say, when you tighten down flanges.